NUREG/CR-6778

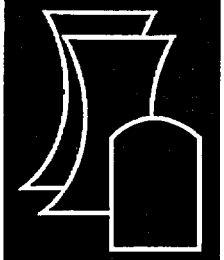

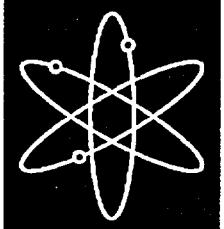

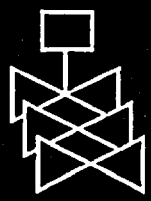

The Effects of Composition and Heat Treatment on Hardening and Embrittlement of Reactor Pressure Vessel Steels

University of California at Santa Barbara

U.S. Nuclear Regulatory Commission
Office of Nuclear Regulatory Research
Washington, DC 20555-0001

AVAILABILITY OF REFERENCE MATERIALS IN NRC PUBLICATIONS

NRC Reference Material

As of November 1999, you may electronically access NUREG-series publications and other NRC records at NRC's Public Electronic Reading Room at http://www.nrc.gov/reading-rm.html. Publicly released records include, to name a few, NUREG-series publications; *Federal Register* notices; applicant, licensee, and vendor documents and correspondence; NRC correspondence and internal memoranda; bulletins and information notices; inspection and investigative reports; licensee event reports; and Commission papers and their attachments.

NRC publications in the NUREG series, NRC regulations, and *Title 10, Energy*, in the Code of *Federal Regulations* may also be purchased from one of these two sources.

1. The Superintendent of Documents
   U.S. Government Printing Office
   Mail Stop SSOP
   Washington, DC 20402–0001
   Internet: bookstore.gpo.gov
   Telephone: 202-512-1800
   Fax: 202-512-2250
2. The National Technical Information Service
   Springfield, VA 22161–0002
   www.ntis.gov
   1–800–553–6847 or, locally, 703–605–6000

A single copy of each NRC draft report for comment is available free, to the extent of supply, upon written request as follows:

Address: Office of the Chief Information Officer,
Reproduction and Distribution
Services Section
U.S. Nuclear Regulatory Commission
Washington, DC 20555-0001
E-mail: DISTRIBUTION@nrc.gov
Facsimile: 301–415–2289

Some publications in the NUREG series that are posted at NRC's Web site address http://www.nrc.gov/reading-rm/doc-collections/nuregs are updated periodically and may differ from the last printed version. Although references to material found on a Web site bear the date the material was accessed, the material available on the date cited may subsequently be removed from the site.

Non-NRC Reference Material

Documents available from public and special technical libraries include all open literature items, such as books, journal articles, and transactions, *Federal Register* notices, Federal and State legislation, and congressional reports. Such documents as theses, dissertations, foreign reports and translations, and non-NRC conference proceedings may be purchased from their sponsoring organization.

Copies of industry codes and standards used in a substantive manner in the NRC regulatory process are maintained at—

The NRC Technical Library
Two White Flint North
11545 Rockville Pike
Rockville, MD 20852–2738

These standards are available in the library for reference use by the public. Codes and standards are usually copyrighted and may be purchased from the originating organization or, if they are American National Standards, from—

American National Standards Institute
11 West 42nd Street
New York, NY 10036–8002
www.ansi.org
212–642–4900

Legally binding regulatory requirements are stated only in laws; NRC regulations; licenses, including technical specifications; or orders, not in NUREG-series publications. The views expressed in contractor-prepared publications in this series are not necessarily those of the NRC.

The NUREG series comprises (1) technical and administrative reports and books prepared by the staff (NUREG–XXXX) or agency contractors (NUREG/CR–XXXX), (2) proceedings of conferences (NUREG/CP–XXXX), (3) reports resulting from international agreements (NUREG/IA–XXXX), (4) brochures (NUREG/BR–XXXX), and (5) compilations of legal decisions and orders of the Commission and Atomic and Safety Licensing Boards and of Directors' decisions under Section 2.206 of NRC's regulations (NUREG–0750).

NUREG/CR-6778

The Effects of Composition and Heat Treatment on Hardening and Embrittlement of Reactor Pressure Vessel Steels

Manuscript Completed: April 2002
Date Published: May 2003

Prepared by
G. R. Odette, G. E. Lucas, D. Klingensmith,
B. D. Wirth, D. Gragg

Department of Mechanical and Environmental Engineering
University of California at Santa Barbara
Santa Barbara, CA 93106

C. Santos, NRC Project Manager

Prepared for
Division of Engineering Technology
Office of Nuclear Regulatory Research
U.S. Nuclear Regulatory Commission
Washington, DC 20555-0001
NRC Job Code Y6396

NUREG/CR-6778, has been reproduced from the best available copy.

ABSTRACT

This report addresses several important issues regarding possible revisions of RG 1.99 Rev. 2 to predict irradiation induced hardening ($\Delta\sigma_y$) and hence embrittlement manifested as shifts (ΔT) in the 41 J Charpy test transition temperature. We are developing a $\Delta\sigma_y$ database from controlled, single-variable experiments to map the individual and interactive effects of metallurgical and environmental variables. The data are generated from a large matrix of composition-controlled alloys irradiated in the Irradiation Variables Facility (IVAR) at the University of Michigan Ford Research Reactor. The results provide quantitative and independent validation of the two component form of the NUREG/CR-6551 model, comprised of matrix feature (MF) and copper rich precipitate (CRP) terms. The IVAR database also quantitatively supports: 1) the model treatments of a strong copper-nickel interaction in the CRP term; 2) the treatment of phosphorous in the MF term; 3) an independent validation of a maximum effective matrix copper level (Cu_{max}) of around 0.3% following heat treatment; and 4) a sensitivity of Cu_{max} to nickel content. The IVAR database also shows: 1) manganese interaction with copper and nickel in the CRP contribution; 2) manganese and nickel increase the MF term; 3) a somewhat unanticipated effect of flux and flux-composition interactions on the fluence dependence of $\Delta\sigma_y$ and ΔT; and 4) a possible reduction in the effect of phosphorus at higher copper.

TABLE OF CONTENTS

ABSTRACT iii

LIST OF FIGURES vii

LIST OF TABLES ix

EXECUTIVE SUMMARY x

ACKNOWLEDGMENTS xii

NOMENCLATURE AND SYMBOLS xiii

1 BACKGROUND AND INTRODUCTION 1

2 OBJECTIVES, STRATEGY, FOCUS AND ORGANIZATION OF THE REPORT 4

3 MATERIALS, EXPERIMENTAL METHODS AND DATA ANALYSIS AND EVALUATION PROCEDURE 6

3.1 Alloys And Specimens 6
3.2 Irradiations 7
3.3 Tensile Testing 18
3.4 Small Angle Neutron Scattering 19
3.5 Field Emission Gun Scanning Transmission Electron Microscopy 21
3.6 Electrical Resistivity Measurements 22
3.7 Seebeck Coefficient Measurements 23

4 EFFECTS OF COMPOSITION ON IRRADIATION HARDENING AND EMBRITTLEMENT 24

4.1 Summary of the Data Trends 24
4.1.1 Copper Bearing Alloys 24
4.1.2 Low Copper Alloys 28

5 ANALYSIS OF THE COMPOSITIONAL TRENDS 33

5.1 Comparison of the IVAR Results With Predictions of the NUREG/CR-6551 Model 33
5.2 The Microstructural Basis, Mechanisms and Models for the Composition Dependence of Hardening and Embrittlement 36
5.2.1 Copper Rich Precipitates 36
5.2.2 Matrix Features 39
5.3 Discussion of Improvements in the NUREG Embrittlement Correlation Model Treatment of Composition Effects 40

6 EVALUATION OF THE MATRIX COPPER CONTENT 44

6.1 General Effects of Heat Treatment on σ_y and $\Delta\sigma_y$ 45
6.2 Estimates of Matrix Copper Levels 49
6.2.1 Estimates of Cu_m Based on Ds_y Deviations From the Low Copper c Trend Line 49
6.2.2 Estimates of Cu_m Based on VSR $\Delta\sigma_y$ Trends and the Modified NUREG/CR-6551 $\Delta\sigma_y$ Model 52

6.3 Microanalytical Assessments of Cu_m 58
6.3.1 Field Emission Gun Scanning Transmission Electron Microscopy 58
6.3.2 Electrical Resistivity 58
6.3.3 Seebeck Coefficient 62
6.4 Summary and Discussion of the Ds_y and Microanalytical Based Estimates of Cu_m 65
6.5 Small Angle Neutron Scattering Studies from the PB Experiment 66

7 A PRE-PRECIPITATION MODEL FOR Cu_m 71

8 SUMMARY AND CONCLUSIONS 74

9 REFERENCES 76

APPENDIX A THE NUREG $\Delta\sigma_y$ MODEL 80

APPENDIX B TENSILE DATA FOR T4, T14, VSR AND PB 85

LIST OF FIGURES

Figure		Page
Figure 3-1	Specimen Baskets in the IVAR Facility	13
Figure 3-2	Schematic Design of the IVAR Irradiation Facility	14
Figure 4-1	Variation of $\Delta\sigma_y$ with bulk copper in intermediate nickel alloys for the a) CM and b) LV series	25
Figure 4-2	Variation of $\Delta\sigma_y$ with nickel for a) 0.4 copper and b) 0.2 copper CM alloys; c) comparison of $\Delta\sigma_y$ versus nickel for intermediate and high copper steels for T14; d) Variation of $\Delta\sigma_y$ with nickel for high copper LV series steels (corresponding CM alloys shown for comparison as small filled symbols)	26
Figure 4-3	Variation of $\Delta\sigma_y$ with manganese for intermediate nickel, high copper CM and LV steels	27
Figure 4-4	Variation of $\Delta\sigma_y$ with boron, molybdenum, and chromium for a) PB and b) T14	27
Figure 4-5	Variation of $\Delta\sigma_y$ with phosphorous for a) low copper, low nickel; b) low copper, intermediate nickel; and c) low copper, high nickel steels; d) Variation of phosphorous sensitivity (B) with nickel; e) Comparison of $\Delta\sigma_y$ (P) for alloys with 0.02 and 0.11 copper	30
Figure 4-6	Variation of $\Delta\sigma_y$ with nickel for a) low and b) high phosphorous steels	31
Figure 4-7	Variation of $\Delta\sigma_y$ with manganese for low copper CM alloys	31
Figure 4-8	Variation of $\Delta\sigma_y$ with carbon, nitrogen, boron and tramp elements (TE) for low copper CM steels	32
Figure 5-1	Comparison of the NUREG-$\Delta\sigma_y$ model predictions with the data from the capsule T14	34
Figure 5-2	Comparison of the NUREG-$\Delta\sigma_y$ model predictions with the data from capsule T14 adjusted to 0.8% nickel and 0.005% phosphorous	34
Figure 5-3	Comparison of the NUREG-$\Delta\sigma_y$ model predictions of nickel dependence of embrittlement with the T14 data for a) 0.4% copper and b) 0.2% copper steels	35
Figure 5-4	Comparison of NUREG-$\Delta\sigma_y$ model predictions with $\Delta\sigma_y$ data as a function of fluence for low copper (0.02%) intermediate nickel (0.85%) CM alloys for both low (0.005%, CM3) and high (0.04%, CM5) phosphorous levels	35
Figure 5-5	Volume fraction of CRP's estimated from SANS measurements on CM and LV alloy for the PB capsule as a function of a) nickel for CM alloys, b) nickel for LV alloys, and c) manganese for CM alloys; d) comparison of measured $\Delta\sigma_y$ with values predicted from SANS microstructural parameters	38
Figure 5-6	Variation of $\Delta\sigma_y$ with a matrix chemistry factor given in Equation 5-2 for low copper CM and LV steels for capsules T14 and PB. The unalloyed VM steels are shown as filled triangles	42
Figure 5-7	$\Delta\sigma_y$ for various V-series alloys with no copper irradiated in PB	43

Figure 5-8 a) Comparison of NUREG matrix feature predictions with low copper French power reactor surveillance data; b) plot showing scatter in $\Delta\sigma_y$ in low copper steel irradiations in this study and unexplained differences between CM and LV alloys 43

Figure 6-1 Variation of σ_y with P_T for a) CM5, 11, 18 b) CM3, 11, 19 c) CM12, 13, 20 47

Figure 6-2 Variation of $\Delta\sigma_y$ with σ_y (unirradiated) for a) high (0.42%) copper CM alloys, b) intermediate (0.8%) nickel 0.22% copper alloys 48

Figure 6-3 Variation of $\Delta\sigma_y$ with c for irradiated intermediate nickel alloys 48

Figure 6-4 Variation of $\Delta\sigma_y$ with c for intermediate nickel CM and LV alloys in capsules T14 (a and b), T4 (c and d) and PB (e and f) 51

Figure 6-5 Variation of $\Delta\sigma_y$ with SR condition for a) CM3, b) CM5, c) CM11, d) CM12, e) CM13, f) CM16, g) CM18, h) CM19, i) CM 20 53

Figure 6-6 $\Delta\sigma_y$-based NUREG model prediction of the variation in Cu_m with SR time for the VSR data for a) CM11, b) CM12, c) CM18, d) CM 19, e) CM20; f) Comparison of high copper CM19 to two lower Cu steels 56

Figure 6-7 $\Delta\sigma_y$-based NUREG model prediction of the variation in Cu_m with stress relief time for the PB data for CM12, CM18, CM19, CM20 57

Figure 6-8 Idealized variation of resistivity with content C_x of solute x 60

Figure 6-9 Variation of resistivity with copper content for a range of alloys 61

Figure 6-10 Variation of resistivity with copper content for a) CM, b) LV and c) as-tempered CM alloys 63

Figure 6-11 Variation of Seebeck coefficient with copper content 64

Figure 6-12 Variation of Seebeck coefficient with copper content for a) stress-relieved CM, b) as-tempered CM and c) LV-series alloys 68

Figure 6-13 Cu_m measurements from various techniques for a) CM11, b) CM19, c) LC 69

Figure 6-14 Effects of t_{sr} on CRP features as measured by SANS on CM19 from the PB capsule 70

Figure 7-1 Comparison of Cu_e to Cu_m for high copper CM alloys from VSR 72

Figure 7-2 Comparison of Cu_m from VSR data to predictions of Equations 7-2 through 7-4 73

Figure 7-3 Comparison of Cu_m for CM19 as a function of t_{sr} 73

Figure A-1 Variation of C_c with ΔT. The dashed line shows the average 83

Figure A-2 Comparison measured $\Delta\sigma_y$ with values predicted from NUREG model for T4 83

Figure A-3 Variation of the difference between predicted and measured $\Delta\sigma_y$ with nickel 84

LIST OF TABLES

Table		Page
Table 3-1	CM-Series Alloy Compositions and Heat Treatments	8
Table 3-2	Stress Relief Anneal Matrix	9
Table 3-3	LV-Series Alloy Compositions and Heat Treatments	9
Table 3-4	Commercial Steels	10
Table 3-5	VM-Series Alloy Composition	11
Table 3-6	Specimen Loadings for Capsules T4 and T14	15
Table 3-7	Capsule loading for VSR	16
Table 3-8	Capsule loading for PB	17
Table 3-9	Irradiation Conditions	19
Table 4-1	Summary of Compositional Dependence of Hardening in High Copper Steels	29
Table 4-2	Summary of Compositional Dependence of Hardening in Low Copper Steels	32
Table 6-1	Estimated Cu_m for Intermediate Nickel High Copper CM Alloys in VSR Study	50
Table 6-2	Estimated Cu_m for Intermediate Nickel High Copper CM Alloys in Various Capsules	50
Table 6-3	Estimated Cu_m for High Copper CM Alloys in VSR Study	57
Table 6-4	Estimated Cu_m for High Copper CM Alloys in PB Study	57
Table 6-5	Averaged Cu_m Following Heat Treatment at ~590-610°C	58
Table 6-6	FEGSTEM Estimates of Cu_m for CM12, CM19 and CM20	59
Table 6-7	Least Square Fit Calibration of Equations 6-7 and 6-8	64
Table 6-8	Microanalytical and $\Delta\sigma_y$ Based Estimates of Cu_m for Typical As-tempered and Stress-relieved Conditions	67

EXECUTIVE SUMMARY

Safe operation of reactor pressure vessels requires evaluation of irradiation embrittlement by neutrons leaking from the core. Embrittlement is currently monitored by measuring changes in the energy-temperature curves of Charpy V-notch specimens irradiated in reactor surveillance programs. Embrittlement is characterized in terms of reductions in the Charpy upper shelf energy (ΔUSE) and elevations of the temperature at 41J (ΔT). The latter is the focus of this report. Prescriptions for evaluating ΔT (and ΔUSE) for a particular steel and vessel exposure condition are provided in US NRC Regulatory Guide 1.99 Revision 2 (RG 1.99/2). However, RG 1.99/2 was based on a rather small database, assembled from the literature several years earlier, and reflects the limited understanding of embrittlement mechanisms at that time.

Over the intervening years, both fundamental understanding of embrittlement mechanisms and the surveillance database have grown, along with a recognition that complex interactions between the irradiation and metallurgical variables control ΔT. Thus the synthesis of various sources of information is the key to reliable embrittlement predictions. Recently a new ΔT correlation model was developed based on statistical fits to the power reactor embrittlement database (PREDB), using equations that were both developed and vetted using physical models and independent sources of pertinent data. The NUREG/CR-6551 Model (sometimes known as the Eason-Wright-Odette Model) has been extensively scrutinized by the nuclear industry and researchers around the world. The ASTM Subcommittee E10.02 has led the independent evaluation of this work, and has considered the NUREG model as a candidate for adoption for ΔT predictions in draft standard E900. The NUREG model, and its progeny, are also under consideration for adoption in a preposed revision to RG 1.99/2.

The NUREG model has proven to be rather robust in these evaluations. It represents a significant statistical improvement over RG 1.99/2, and is based on a much better physical model of embrittlement. However specific issues have been raised, and new questions continue to emerge regarding details of the model. The results presented in this report represent part of a larger overall effort to address and resolve these issues. The technical approach involves developing an independent embrittlement database from controlled, single-variable experiments. High-resolution experimental maps of the individual and interactive effects of metallurgical and environmental variables on embrittlement are derived from irradiation and post-irradiation testing of very large experimental matrices. These studies take advantage of the relationship between ΔT and increases in yield stress ($\Delta\sigma_y$), which can be measured using small tensile specimens. These studies achieve precise control and characterization of the embrittlement variables. Irradiations are carried out in the Irradiation Variable Facility (IVAR) at the University of Michigan Ford Research Reactor. The large experimental $\Delta\sigma_y$ database under development, will be complemented by an extensive effort to characterize the micro(nano)structural changes responsible for $\Delta\sigma_y$ and ΔT. The collective results will be analyzed and used to develop quantitative, mechanism-based embrittlement models.

This report focuses on a subset of important questions that must be answered in establishing a technical basis for any future revision to RG 1.99/2. In particular the following issues are addressed, and to a large extent resolved, by the IVAR data and analysis reported here. These advances include:

1. Quantitative independent validation of the general two component form of the NUREG model comprised of copper-independent matrix features and copper-dependent copper rich precipitates (CRPs) terms.

2. Quantitative independent validation of the very strong interaction between copper and nickel in the NUREG model CRP contribution to ΔT. The specific thermodynamic basis for this interaction is described, along with an example from a larger supporting microstructural characterization database.

3. Validation of the inclusion of phosphorous in the NUREG model, and strong support for its approximate treatment in the matrix feature contribution to ΔT.

4. Validation of a maximum effective matrix copper level of around 0.3% following tempering and stress relief heat treatments as found in the NUREG model. Strong support is also presented for even lower maximum effective matrix copper levels of about 0.25% in low-to-intermediate nickel steels, as well as evidence for corresponding levels in excess of 0.3% in high nickel steels. The role of stress relief time and temperature on effective matrix copper levels is also elucidated and represented in terms of a simple pre-precipitation model.

In addition, the database and analysis in this report also provides additional insight into several other issues, which are further from closure. Resolution of these issues could lead to significant further improvements in embrittlement forecasting. They include:

1. Possible sources of product form variability and data scatter in the CRP term. These include embrittlement contributions from elements not explicitly accounted for in the NUREG model, like manganese (interacting with nickel and copper), and effects of microstructural variations on the fluence dependence of $\Delta\sigma_y$ and ΔT.

2. An unanticipated effect of flux and flux-composition interactions on the fluence dependence of the CRP contribution to $\Delta\sigma_y$ and ΔT.

3. Effects of the unirradiated constitutive and Charpy properties on: a) the $\Delta\sigma_y$ produced by a specified embrittlement microstructure; and b) the relationship between $\Delta\sigma_y$ and ΔT. This work has also identified new mechanisms that influence the effects the heat treatment on the unirradiated microstructure and properties, hence, also on $\Delta\sigma_y$ and ΔT.

4. Possible sources of product form variability and data scatter in the matrix feature term, including an increase in $\Delta\sigma_y$ with manganese and nickel.

5. A possible interaction reducing the effect of phosphorus at higher copper.

All of these issues, and several others, are the subject of ongoing research in the UCSB program.

ACKNOWLEDGMENTS

The authors appreciate the advice and encouragement of Al Taboada, and Mike Vassilaros our former project managers at the U. S. Nuclear Regulatory Commission and Carolyn Fairbanks our current project manager. Al Taboada contributed enormously to the conceptual design of our program and Mike Vassilaros was instrumental in turning these concepts into realities. Carolyn Fairbanks has helped us in the completion of this part of the work and has provided sustained support for our research. The advice and support from other U.S. NRC staff are also appreciated. The staff and students in our group at the University of California Santa Barbara, particularly Chris Cowan, have made important contributions to various parts of this research. The support of the collaborators at ORNL, particularly Roger Stoller, Randy Nanstad, Mikhail Sokolov and Dennis Heatherly, as well as the staff at the Ford Nuclear Reactor irradiation facility, particularly Phil Simpson, are greatly appreciated. We would also like thank the staff at AEA Technology, especially Amanada Kenway-Jackson, Colin English and Will Phythian, for their role in procuring alloys and performing FEGSTEM studies. The work was performed under U.S. NRC Contract 04-94-049.

NOMENCLATURE AND SYMBOLS

SYMBOLS

A_i	intercept of $\Delta\sigma_y$ sensitivity to ith specie
B_i	slope of $\Delta\sigma_y$ sensitivity to ith specie
C_c	ratio of ΔT to $\Delta\sigma_y$
CF	chemistry factor
C_i	concentration of ith specie
Cu_{bk}	bulk copper concentration
Cu_e	effective copper concentration
Cu_m	matrix copper concentration
E_{sr}	pre-precipitation effective activation energy
F	neutron scattering factor
f_i	volume fraction of ith specie
f_ϕ	flux factor
k_i	resistivity coefficient of ith specie
k_{sr}	pre-precipitation rate coefficient
N_i	number density of ith feature
P_{Tt}	heat treatment temperature-time factor
q	neutron scattering vector
r_i	radius of ith feature
r_{ip}	radius of ith feature at peak strength
r_m	mean radius of scattering feature
S	Seebeck coefficient
S_i	Seebeck coefficient from ith contribution
t_{ht}	heat treatment time
t_{sr}	stress relief time
T_{ht}	heat treatment temperature
ΔT	41J indexed Charpy transition temperature shift
ΔT_i	shift due to ith contribution
V_i	Volume of ith feature
β	scattering distribution fit parameter
χ	NUREG copper factor
ϕ	flux
ϕt	fluence
ϕ_s	neutron scattering angle relative to magnetic field
γ_{sr}	numerical constant for pre-precipitation rates
κ_i	Seebeck coefficient sensitivity to ith species
Λ_i	strength of ith obstacle
ρ	Resistivity
ρ_i	contribution to resistivity of ith source
$\Delta\rho$	neutron scattering contrast
$d\Sigma/d\Omega$	SANS scattering intensity
σ_i	strength contribution from ith source
σ_u	unirradiated obstacle yield strength contribution
σ_y	yield strength
$\Delta\sigma_y$	change in yield strength
θ	superposition parameter
ASAXS	Anomalous Small Angle X-ray Scattering
CRP	Copper rich precipitate

FEGSTEM	Field Emission Gun Scanning Transmission Electron Microscope
FNR	Ford Nuclear Reactor
HF	High Flux
HT	Heat Treatment
IVAR	Irradiation Variables Facility
IF	Intermediate Flux
LF	Low Flux
PIA	Post-Irradiation Annealing
SAW	Submerged Arc Weld
SR	Stress Relief
SSR	Standard Stress Relief
SANS	Small Angle Neutron Scattering
TEP	Thermoelectric Power

1 BACKGROUND AND INTRODUCTION

Accurate prediction of neutron irradiation embrittlement of reactor pressure vessels is a key component in structural integrity assessments for both normal operation and during accident transients [USNRC, 1986]. Embrittlement is currently empirically characterized in reactor surveillance programs by measuring changes in the Charpy V-notch transition energy-temperature curves of representative vessel steels. Data from surveillance programs are archived in the Power Reactor Engineering Data Base (PREDB) [Stallman et. al, 1994], compiled at Oak Ridge National Laboratory. Charpy data are usually represented as temperature shifts indexed at 41J (ΔT) and reductions in the upper shelf energy (ΔUSE). Regulatory procedures for predicting embrittlement are described in US NRC Regulatory Guide 1.99 Revision 2 (RG 1.99/2) published in 1988 [USNRC, 1988]. However, the ΔUSE and ΔT in RG 1.99/2 were based on a rather small database, assembled from the literature several years earlier and reflect the limited understanding of embrittlement mechanisms at that time.

Over recent years both fundamental understanding of embrittlement mechanisms and the surveillance database have grown, along with a recognition that complex interactions between the irradiation and metallurgical variables control ΔT [Odette and Lucas, 1989, 1996, 1997, 1998; Odette, 1998; Buswell and Jones, 1993; Fisher and Buswell, 1987; Stoller, 1996; Lott and Freyer; 1996, Bolton, et al, 1996; McElroy and Lowe, 1996; English et al, 1997]. The irradiation variables include temperature and exposure time, neutron flux, fluence and spectrum. Metallurgical variables include composition and processing history, which combine to mediate the start-of-life alloy microstructure and microchemistry. Elements that are known, or thought, to influence ΔT include copper, nickel, phosphorous, manganese, and perhaps, silicon and nitrogen. Corresponding processing and microstructural variables are more difficult to parameterize, but clearly include product form and tempering-stress relief heat treatment. A myriad of other factors, that mediate the start-of-life condition of a steel, as represented by grain and subgrain structures, dislocation densities and arrangements, as well as carbide and other second phase distributions, also play a role. These microstructural factors are manifested in terms of both the effect of the start-of-life properties on embrittlement as well as their effect on fine scale changes in the microstructures caused by irradiation that alter these properties.

An example of such complex metallurgical effects, which are the focus of this report, is provided by the interaction between copper, nickel, manganese and stress-relief heat treatment. Irradiation hardening, which is the primary cause of embrittlement, increases with increasing nickel and manganese content. However, the effect of these elements acting in tandem, is synergistic in steels containing a significant amount of copper. Further at high levels, the effective copper content is influenced by the heat treatment because of pre-precipitation of this element. The amount of copper pre-precipitation appears to be influenced by the alloy nickel content. Both the heat treatment and composition in turn influence the start-of-life alloy strength, which also affects the irradiation hardening. Additional combinations of these variables may influence ΔT, but it is sufficient to conclude that such interactions and synergisms can only be reliably understood and accounted for based on insight provided by combinations of careful, single variable experiments and modeling. However, it is also equally clear that such complexity, and limitations in understanding, demand that predictive models be derived from the most realistic database available, currently represented by the PREDB.

Thus the synthesis of various sources of information is the key to reliable embrittlement predictions. Recently a major advance in implementing this paradigm was reported in

NUREG/CR-6551 [Eason et al, 1988]. which featured the following key elements in deriving ΔT predictions.

1. The ΔT predictions were based on non-linear least squares fits of correlation equations to a carefully scrubbed, frozen version of the PREDB.

2. The correlation equations were developed based on understanding of key embrittlement mechanisms.

3. Selection from among a large number of statistically similar calibrated correlation equations was based on both mechanistic considerations and consistency with independent sources of data, largely derived from test reactor studies.

4. Both the limits of the correlation equations, and the likelihood they would continue to be refined, were recognized. Thus unless there was a combination of mechanistic and statistical significance dictating otherwise, the correlation equations were kept as simple and with as few degrees of freedom as possible. The attendant compromises included use of correlation equation forms that were consistent with the demands of nonlinear data fitting methods.

While the NUREG/CR-6551 equations are fairly robust and reliable, more importantly the overall methodology established a framework for continuing improvements in embrittlement predictions and a basis to assess important gaps in understanding. Significant issues that have been identified include:

1. What are the sources of embrittlement variability associated with product form, or even vessel vendor, and the corresponding underlying microstructural basis? Note this is also an important issue related to other sources of material variability, like weld practice, heat affected zones, through thickness variation of properties and, very importantly, treatment of the relation of surveillance materials to those in the vessel itself, or the issue of surrogate materials.

2. What are the sources of large scatter and differences with other database trends in the copper-independent, so-called matrix feature term?

3. What is the effective upper cut-off in copper content; and how is this affected by other variables, such as nickel and heat treatment, and how is it best modeled in the correlation equations?

4. What is the effect of phosphorous and how can it be best modeled?

5. What are the effects of flux and time-at-temperature? How are these factors influenced by other variables and how are they best treated in the correlation equations?

6. What variables, terms and mechanisms could be missing from the existing correlation equations? This includes interactions between existing variables as well as variables that are currently not accounted for.

The latter point deserves a brief elaboration. Statistical methods, even using simple, non-physical algebraic correlation equations, generally can reasonably fit a database within expected scatter and considering other sources of uncertainties. However, various terms in such models may be entirely non-physical, simply acting as surrogates for real physical effects. Put simply, the fitting model will force itself to work as well as it can independent of the reality of how it does it. At least to some extent, this involves replacing something that is missing with something that simply works (or, to say it simply, pushing something in one place pops something out in another place). Correlation equations with a more solid physical basis suffer similar limitations if they are not complete and do not start with a balance of terms that are physically based. Non-physical correlations cannot be extrapolated and even fail within in apparently valid regime when variable surrogacy

breaks down. Clearly, avoiding such traps requires developing independent sources of data and mechanistic understanding, which is the overarching goal of the work partially described in this report.

2 OBJECTIVES, STRATEGY, FOCUS AND ORGANIZATION OF THE REPORT

The UCSB embrittlement research program has a number of objectives ranging from early warnings of possible technical surprises, to improving a broad array of integrity assessment methods, such as the tasks in support of the master curve method [ASTM E1921-97]. The activities pertinent to this report relate specifically to the issues listed at the end of the previous section, viz. - developing an independent database involving controlled, single-variable experiments and mechanistic models. This effort involves:

1. Developing high resolution experimental embrittlement maps of the individual and interactive effects of metallurgical and environmental variables. This task involves irradiation and post-irradiation testing of a very large matrix of alloy/alloy condition-flux-fluence-temperature combinations with precise control and characterization of the embrittlement variables. The primary facility is the Irradiation Variable Facility (IVAR) at the University of Michigan Ford Research Reactor.

2. Detailed pre and post-irradiation (as well as annealing-reirradiation) microstructural studies and focused mechanism experiments in support of physical model development.

3. Development of detailed multiscale embrittlement models that quantitatively treat all key variables and variable interactions.

4. Synthesis of these results with other pertinent information and ultimate application to improved embrittlement correlation equations fit to the PREDB.

A key element of the strategy to meet the first objective is the use of yield stress changes ($\Delta\sigma_y$) as a measure of embrittlement (ΔT). The $\Delta\sigma_y$-ΔT relation is well established [Odette et. al, 1985; Odette and Lucas, 1989]. but will be further developed and quantified as part of this work. The use of $\Delta\sigma_y$ as the key property enables establishing the embrittlement maps using small tensile specimens coupled with semi-automated testing. As a result very large experimental matrices are practical. The use of $\Delta\sigma_y$ also has other advantages, such as generally high precision and physical relationships to other measures of embrittlement, such as shifts in fracture toughness-temperature master curves [Odette and He, 2000, in press]. The results reported here are a small part of the much larger overall study and focus on the specific effects of compositional and heat treatment variations on $\Delta\sigma_y$.

A wide variety of techniques are being used, in combination, for microstructural characterization and other mechanism studies. Methods include small angle neutron and anomalous x-ray scattering, atom probe, transmission electron microscopy, post irradiation annealing, electrical resistively and the Seebeck coefficient. These studies are ongoing and only limited, and in some cases preliminary, results on small angle neutron scattering, transmission electron microscopy, electrical resistively and the Seebeck coefficient are presented in this report.

Models of the key sub-processes mediating embrittlement have been developed and extensively used to improve the understanding of the underlying mechanisms as well as to guide and verify correlation model development. Integration of these components into a comprehensive quantitative embrittlement model is underway. The results of modeling pertinent to interpreting the experimental trends are summarized briefly in this report, with further details presented elsewhere [Odette and Lucas, 1997, 1998; Odette, 1998] or in future publications and reports.

The report is organized as follows. A description of the steels examined in this study, the

experimental test methods and procedures for the data analysis and evaluation are described in Section 3. The $\Delta\sigma_y$ for two sets (CM and LV) of split melt UCSB alloys and a range of steels acquired from other programs irradiated to medium fluence between 0.48 and $1x10^{23}n/m^2$ (E > 1 MeV) are presented in Section 4. Only a limited number of medium fluence capsules tested to date contain complete, or nearly complete, matrices of the steels examined in this program. These data are complemented by the results for a more limited number of key UCSB alloys contained in other medium fluence IVAR capsules. An analysis and evaluation of these results is presented in Section 5, by comparing the $\Delta\sigma_y$ data to predictions of the NUREG/CR-6551 model. Section 6 describes the effects of systematic variations in stress relief time and temperature on $\Delta\sigma_y$ for a subset of the UCSB CM alloys. This section includes the results of a variety of characterization techniques used to evaluate the matrix content of dissolved copper, as well as estimates based on the $\Delta\sigma_y$ measurements themselves. These results are analyzed in Section 7 to assess the mechanisms giving rise to stress relief effects, with particular emphasis on maximum copper limits set by pre-precipitation. Section 8 summarizes the overall results and presents the main conclusions derived from this study.

3 MATERIALS, EXPERIMENTAL METHODS AND DATA ANALYSIS AND EVALUATION PROCEDURES

3.1 Alloys and Specimens

A large set of alloys was investigated in this study. The alloys are classified in four general categories:

1. The compositions of a large set of complex A533B-type split melt steels (CM-series) are shown in Table 3-1. A total of 31 variants around a base composition were used to evaluate the effects of both: a) *combinations* of Cu (0.0 to 0.8%[1]), Ni (0.0 to 1.6%), Mn (0 to 1.6%) and P (0.005 to 0.040%) contents; and b) *single* variable modifications of Mo, N, C, B, Al and As/Sn/Sb contents. All 31 alloys contained about 0.005%Al and 0.25%Si. The alloys were fabricated in collaboration with AEA Technology, Harwell. Chemistries were determined by the manufacturer, and spot checked for several alloys upon receipt by a combination of atomic absorption and interstitial element analysis. Further verification of chemistries is planned. For two of the irradiations, T4 and T14 (described below), the alloys received a base heat treatment consisting of an austenitization at 900°C for 0.5h, followed by a salt bath quench at 450°C for 10min, an air cool, tempering at 660°C for 4h: air cool and a stress relief anneal at 607°C for 24 h, followed by a slow cool at 8°C/h to 300°C, and a subsequent air cool. This is referred to as the standard stress relief (SSR) heat treatment. The SSR yielded prior austenite grain sizes of about 50±10 μm and microstructures ranging from tempered bainite (most CM alloys) to mixed tempered ferrite-bainite. A complete microstructural description for all the alloys will be provided in a future report.

   For one of the irradiations, VSR (described below), nine of the alloys received alternate stress relief anneals; the alloys and the stress relief anneal matrix are shown in Table 3-2.

   Finally, for a piggy-back irradiation, PB (described below), the 31 alloys were irradiated in the as-tempered condition. In addition, several of the alloys received the following alternate heat treatments:

   CM5: as-tempered plus aged 480° for 100 h, air cooled

   CM8: salt bath quenched at 400°C after austenitization, then tempered

   CM12: as-tempered plus stress relieved 600°C 8 h, air cooled

   CM18: as-tempered plus stress relieved 600°C 40h, air cooled

   CM19: as-tempered plus stress relieved 600°C 8, 40 and 80 h, air cooled

   CM19: salt bath quenched at 500°C after austenitization, then tempered

   CM20: as-tempered plus stress relieved 600°C 40h, air cooled

   CM20: salt bath quenched at 500°C after austenitization, then tempered

   CM23: salt bath quenched at 400°C after austenitization, then tempered

   CM26: as-tempered plus aged 480° for 100 h, air cooled

2. The compositions and heat treatment for a set of eight complex commercial type bainitic model steels (LV-series) with systematic variations in copper and nickel are shown in Table 3-3. These steels have been irradiated in previous programs at a variety

[1] Compositions are given in weight per cent, unless stated ortherwise

of conditions, primarily around 300°C,. and are described in more detail elsewhere [Odette and Lucas, 1989]. They have microstructures and unirradiated properties very similar to those in the CM-series.

3. The compositions and heat treatments for a set of 13 commercial steels are shown in Table 3-4. The commercial steel series consists of: 1) three welds (A, B, C) obtained from Babcock and Wilcox, with a range of copper contents from low (0.06) to high (0.28); 2) a set of 5 welds (62W-73W) prepared for and used in the HSSI program; 3) plate 02 of the A533B correlation monitor material prepared for the HSST program; 4) JRQ plate material developed for an IAEA coordinated research program; and 5) a Linde 0091 weld (EPRI C) prepared for and used in previous EPRI-sponsored research. Both baseline and irradiated data have been obtained for all these steels and are largely reported in the literature. The heat treatments and compositions reported in Table 3-4 were taken from the literature or documentation supplied with the plate (e.g., JRQ).

4. The compositions and heat treatment for a set of 18 simple split melt model iron and steel alloys (VM-series) with systematic variations in Cu, C, and N are shown in Table 3-5. These alloys were also fabricated in collaboration with AEA Technology, Harwell. Chemistries were determined by the manufacturer, and spot checked for several alloys upon receipt by a combination of atomic absorption and interstitial element analysis. Further verification of chemistries is planned. The microstructures of these alloys are generally characterized by a wide distribution of ferrite grain sizes (in some cases duplex and/or with processing texture). A complete microstructural description for all the alloys will be provided in a future report. Rapid quenchingwas carried out to maintain copper in solution. These alloys were used in this study to calibrate resistivity and Seebeck coefficients as a function of copper concentration as discussed in Section 6. In addition, several of the alloys were irradiated in the PB and several other IVAR capsules. However, only a limited number have been tested and are reported here.

Sheet tensile specimens with a gage section 9 mm x 2 mm x 0.5 mm were prepared by precision die punching heat treated coupons lapped to 0.5±0.005 mm thick. The quality of the die was monitored by punching and tensile testing a variety of calibration metals after about every 500 specimens had been punched. Baseline tensile tests on unirradiated material indicated some variability in properties in several of the alloys. Hence, to reduce scatter in the subsequent yield stress change measurements, the end tabs of selected tensile specimens were pre-indented to obtain Vickers microhardness numbers. An average of 4 indentations were made on the tab ends of the tensile specimens. The microhardness values were used to help identify which baseline values would be used for the irradiated data to evaluate yield stress change. This was complemented by a system to keep track of the location in the billet from which specimens were obtained, so that in high variability cases, data from specimens from similar regions could be used to evaluate yield stress changes. Wafers comprised of the interstitial pieces between tensile specimen punch-outs were also included in some of the irradiations for the purpose of microhardness and/or microstructural characterization. Small angle neutron scattering (SANS) specimens 1.135 cm x 1.2 cm x 2 mm were also machined from selected materials and included in the irradiations.

3.2 Irradiations

Results for four irradiations, designated T4, T14, VSR, and PB are the primary focus of this report. The specimens and materials included in these irradiations are listed in Tables 3-6 through 3-8. The T4 and T14 capsules contained tensile, wafer and SANS specimens of all of the materials. The VSR capsule contained specimens from the CM alloys subjected to the

Table 3-1. CM-Series Alloy Compositions and Heat Treatments

	COMPOSITION (weight per cent)												
Alloy	Cu	Ni	Mn	Cr	Mo	P	N (ppm)	C	Si	S	As/Sb /Sn	Al	B (ppm)
CM1	0.01	0.01	1.67	0.04	0.56	0.003	<50	0.13	0.15	0.004	0.005	0.025	<1
CM2	0.01	0.01	1.65	0.04	0.56	0.041	<50	0.14	0.16	0.004	0.005	0.022	<1
CM3	0.02	0.85	1.60	0.00	0.49	0.006	<50	0.13	0.16	0.000	0.005	0.002	<1
CM4	0.02	0.86	1.53	0.05	0.55	0.031	<50	0.16	0.16	0.003	0.005	0.006	<1
CM5	0.02	0.86	1.61	0.04	0.53	0.050	<50	0.15	0.16	0.000	0.005	0.005	<1
CM6	0.02	1.68	1.50	0.05	0.54	0.007	<50	0.15	0.17	0.003	0.005	0.006	<1
CM7	0.00	1.70	1.55	0.05	0.56	0.047	<50	0.16	0.17	0.003	0.005	0.003	<1
CM8	0.01	0.86	0.01	0.04	0.55	0.004	<50	0.13	0.14	0.002	0.005	0.026	<1
CM9	0.01	0.86	0.85	0.04	0.55	0.003	<50	0.15	0.15	0.003	0.005	0.013	<1
CM10	0.02	0.88	1.66	0.05	0.53	0.008	<50	0.16	0.17	0.004	0.005	0.003	<1
CM11	0.34	0.85	1.64	0.02	0.53	0.006	<50	0.15	0.18	0.003	0.005	0.003	<1
CM12	0.86	0.84	1.65	0.02	0.51	0.006	<50	0.15	0.17	0.003	0.005	0.002	<1
CM13	0.11	0.83	1.61	0.00	0.51	0.004	<50	0.15	0.16	0.000	0.005	0.002	<1
CM14	0.11	0.83	1.62	0.00	0.52	0.040	<50	0.16	0.17	0.000	0.005	0.003	<1
CM15	0.22	0.02	1.59	0.02	0.58	0.002	<50	0.14	0.15	0.003	0.005	0.019	<1
CM16	0.22	0.82	1.58	0.00	0.51	0.004	<50	0.16	0.25	0.000	0.005	0.003	<1
CM17	0.22	1.59	1.54	0.00	0.50	0.004	<50	0.16	0.25	0.000	0.005	0.003	<1
CM18	0.43	0.02	1.70	0.02	0.56	0.002	<50	0.14	0.15	0.003	0.005	0.017	<1
CM19	0.42	0.85	1.63	0.01	0.51	0.005	<50	0.16	0.16	0.003	0.005	0.003	<1
CM20	0.43	1.69	1.63	0.02	0.50	0.006	<50	0.16	0.16	0.003	0.005	0.003	<1
CM21	0.42	0.84	0.01	0.02	0.58	0.002	<50	0.14	0.14	0.003	0.005	0.015	<1
CM22	0.42	0.84	0.84	0.02	0.56	0.002	<50	0.14	0.14	0.003	0.005	0.010	<1
CM23	0.02	0.83	1.62	0.04	0.55	0.002	<50	0.03	0.15	0.003	0.005	0.015	<1
CM24	0.02	0.87	1.65	0.05	0.52	0.010	<50	0.34	0.15	0.003	0.005	0.004	<1
CM25	0.01	0.87	1.53	0.05	0.52	0.003	200	0.14	0.17	0.002	0.005	0.018	<1
CM26	0.01	0.87	1.66	0.05	0.52	0.006	<50	0.16	0.17	0.003	0.020	0.003	<1
CM27	0.02	0.84	1.60	0.05	0.51	0.002	<50	0.16	0.16	0.003	0.005	0.002	10
CM28	0.42	0.84	1.60	0.02	0.51	0.002	<50	0.16	0.17	0.003	0.005	0.002	10
CM29	0.21	0.02	1.68	0.02	0.02	0.002	<50	0.14	0.14	0.003	0.005	0.015	<1
CM30	0.22	0.86	1.64	0.42	0.50	0.006	<50	0.16	0.16	0.003	0.005	0.003	<1
CM31	0.01	0.80	1.65	0.05	0.51	0.006	<50	0.16	0.17	0.003	0.005	0.034	<1

Table 3-2. Stress Relief Anneal Matrix

Alloys: CM3, CM 5, CM11, CM12, CM13, CM16, CM18, CM19, CM20

Slow Cool Matrix: Stress relieved at the following times and temperatures followed by a program cool at 8°C/h to 300°C followed by an air cool

Temperatures (°C)	Times (h)
590	24, 48, 96
607	12, 24, 48, 96
624	12, 24, 48
641	6, 12, 24
as-tempered	

Variable Cool Matrix: Stress relieve at 607°C for 24h, air cool

Table 3-3. LV-Series Alloy Compositions and Heat Treatments

	Composition (weight percent)††				
Code	C	Cu	Ni	Mn	Si
LA	0.14	0.40	0.00	1.37	0.22
LB	0.14	0.40	0.18	1.35	0.22
LC	0.14	0.41	0.86	1.44	0.23
LD	0.19	0.38	1.25	1.38	0.23
LG	0.16	0.00	0.74	1.37	0.22
LH	0.16	0.11	0.74	1.39	0.24
LI	0.16	0.20	0.74	1.37	0.24
LJ	0.16	0.42	0.81	1.34	0.13
LK	0.13	0.80	0.81	1.13	0.13
LO	0.14	0.41	0.86	1.44	0.23

†† Alloys contained $P < 0.005$, $S \leq 0.015$, $Cr \leq 0.085$, $Mo \approx 0.55$; they were austenitized 900°C/1h; air cooled; tempered 664°C/4h; air cooled; stress relieved 600°C/40h; furnace cooled to 300°C; air cooled. With the exception of LO, which was not stress relieved after tempering

Table 3-4. Commercial Steels

	COMPOSITION (weight per cent)										
Code	C	Mn	P	S	Si	Cr	Ni	Mo	Cu	V	HT*
A	0.08	1.69	0.014	0.013	0.45	0.14	0.63	0.40	0.21	--	1
B	0.09	1.63	0.018	0.009	0.54	0.10	0.69	0.40	0.28	--	2
C	0.08	1.30	0.009	0.010	0.37	0.08	0.62	0.31	0.06	--	3
62W	0.08	1.61	0.020	0.007	0.59	0.12	0.60	0.39	0.23	0.01	4
63W	0.10	1.65	0.016	0.011	0.63	0.10	0.69	0.43	0.30	0.01	5
65W	0.08	1.45	0.015	0.015	0.48	0.09	0.60	0.39	0.22	0.006	6
67W	0.08	1.44	0.011	0.012	0.50	0.09	0.69	0.39	0.27	0.007	7
73W	0.10	1.56	0.005	0.005	0.45	0.25	0.60	0.58	0.31	--	8
Midland	0.08	1.61	0.017	0.007	0.62	0.10	0.57	0.41	0.27	0.004	9
EPRI C	0.16	1.55	0.005	0.009	0.17	0.04	0.60	0.44	0.35		10
A302B	0.21	1.20	0.015	0.017	0.28	0.24	0.20	0.60	0.14	0.004	11
HSST02	0.23	1.55	0.009	0.014	0.20	0.04	0.67	0.53	0.14	0.003	12
JRQ	0.18	1.40	0.019	0.004	0.25	0.12	0.82	0.50	0.14	0.003	13

*Heat Treatments

1. Post weld heat treatment (PWHT) 607°C for 15 h, furnace cool
2. PWHT, 607°C for 23 h, furnace cool
3. PWHT, 607°C for 13.5 h, furnace cool
4. Submerged arc wild (SAW): stress relieved (SR) 8 cycles of 6 h at 593-621°C
5. SAW, SR 48 h at 593-621°C
6. SAW, SR 80 h at 593-621°C
7. Not available
8. PWHT 607°C, 40h
9. PWHT 607°C, 22.5h
10. SAW, PWHT 620°C, 50h
11. Normalized and tempered; tempered for 6.5 h at each of 926°C, 885°C, 648°C, and 607°C, WQ
12. Austenitized 871°C, water quench; tempered 663°C, 4 h; FC; stress relieved 607°C, 40h, FC
13. Normalized @ 900°C, quenched at 880°C, tempered at 665°C for 12 h, SR at 620°C 40h

Table 3-5 VM-Series Alloy Compositions

Alloy	Composition (Weight per cent)* Cu	Mn	N (appm)	C	Ti
VA	0.000	0.00	5	0.00	0.000
VB	0.020	1.01	40	0.01	0.002
VC	0.020	1.03	30	0.17	0.004
VD	0.875	1.03	10	0.00	0.000
VE	0.910	1.08	20	0.16	0.010
VG	0.510	0.06	20	0.01	0.002
VH	0.910	0.01	20	0.01	0.010
VI	0.510	0.05	10	0.17	0.003
VJ	0.890	0.02	10	0.17	0.005
VK	0.020	0.02	100	0.01	0.001
VL	0.010	0.01	100	0.00	0.300
VM	0.510	0.01	120	0.01	0.010
VN	0.875	0.00	110	0.00	0.000
VO	0.910	0.00	110	0.16	0.000
VP	0.900	0.01	110	0.00	0.300
VR	0.010	1.06	100	0.01	0.010
VS	0.920	1.00	110	0.00	0.002
VT	0.880	1.00	90	0.00	0.260

*Solution treat 775°C, 17h; quench in salt bath at 450°C, 3 minutes, air cool

variable stress relief series described above. The PB capsule contained specimens for the LV-series and CM-series. As described previously, for this irradiation the CM alloys were primarily in the as-tempered condition; however, selected alloys were also irradiated in several alternative heat treatment conditions.

For the T4, T14 and VSR irradiations, specimens were loaded into aluminum boxes 2.54cm x 2.54cm x 1cm deep. Once loaded, the specimens were shimmed with aluminum foil, and an aluminum cover plate was screwed on. These capsules were machined to final tolerance and shipped to the University of Michigan for irradiation in the IVAR (Irradiation VARiables) facility.

IVAR was collaboratively designed by UCSB and ORNL, and it was fabricated and is operated by ORNL. It consists of a sealed container incorporating 50 electrical heaters and has 49 thermocouples to monitor temperatures. The entire facility is enclosed in a boral shield to reduce activation from thermal neutrons. Two removable specimen baskets contain the irradiation capsules described above. The facility has two separate sections referred to as the high flux (HF) and the intermediate flux/low flux (IF/LF) sections. The HF portion of the facility consists of a removable specimen basket, which can contain 2 capsules at each of 2 different temperatures (nominally 270 and 310°C) and 14 capsules at a third temperature (nominally 290°C). The IF/LF section consists of a removable basket which can contain 9 capsules and one half capsule at each of 2 different temperatures (nominally 270 and 310°C) and 18 capsules and 2 half capsules at a third temperature (nominally 290°C). The specimen baskets with their sliding cover plate are shown in Figure 3-1 and a schematic diagram of the irradiation facility is shown in Figure 3-2.

The Ford Nuclear Reactor (FNR) is a 2 MW pool-type reactor located on the campus of the University of Michigan in Ann Arbor, Michigan. The reactor nominally operates on a fixed cycle consisting of 10 days of operation at full power, followed by a 4-day maintenance shutdown. Experimental facilities are located in a grid assembly located on the south and east faces of the reactor. The IVAR facility, and two companion ORNL facilities, are located on a movable carriage at the southeast corner of the reactor. The fully loaded IVAR facility, including dummy blocks, is brought to temperature in a retracted position. The facility is then moved up against the reactor face at full power. The HF zone sits closest to and the LF zone furthest from the reactor face. At the end of an irradiation cycle, the facility is moved to the retracted position, away from the reactor face. When a capsule(s) reaches its target fluence, the basket containing it is loaded into a shielded transfer cask. The HF and IF/LF baskets can be removed independently. The basket(s) is transferred to a hot cell in the transfer cask where the capsule(s) is removed and replaced. The basket(s) is then returned to the IVAR facility using the transfer cask. Hence, the desired irradiation temperature, flux and fluence is achieved by locating a capsule at the appropriate site in the facility and exposing it for the requisite time. Estimated uncertainties in the irradiation temperature are ±5°C.

Prior to its installation, the flux in the IVAR location was mapped by a multiple foil activation experiment [Remec, 1998]. During the first cycle of IVAR operation 16 additional sets of Fe and Ni wires and 7 multiple foil sets were located throughout the IVAR baskets and subsequently removed and counted after the first cycle. The fluxes reported [Remec, 1997] were in reasonable agreement with the initial map, although there appeared to be a slight reduction in the high flux positions. In addition, every capsule that has been irradiated in IVAR has included an Fe and Ni wire pair. Nine of these have been counted from 6 locations. The activity measurements were carried out by J. Adams of the Neutron Interactions and Dosimetry Group at NIST in Gaithersburg, MD. Analysis of these data

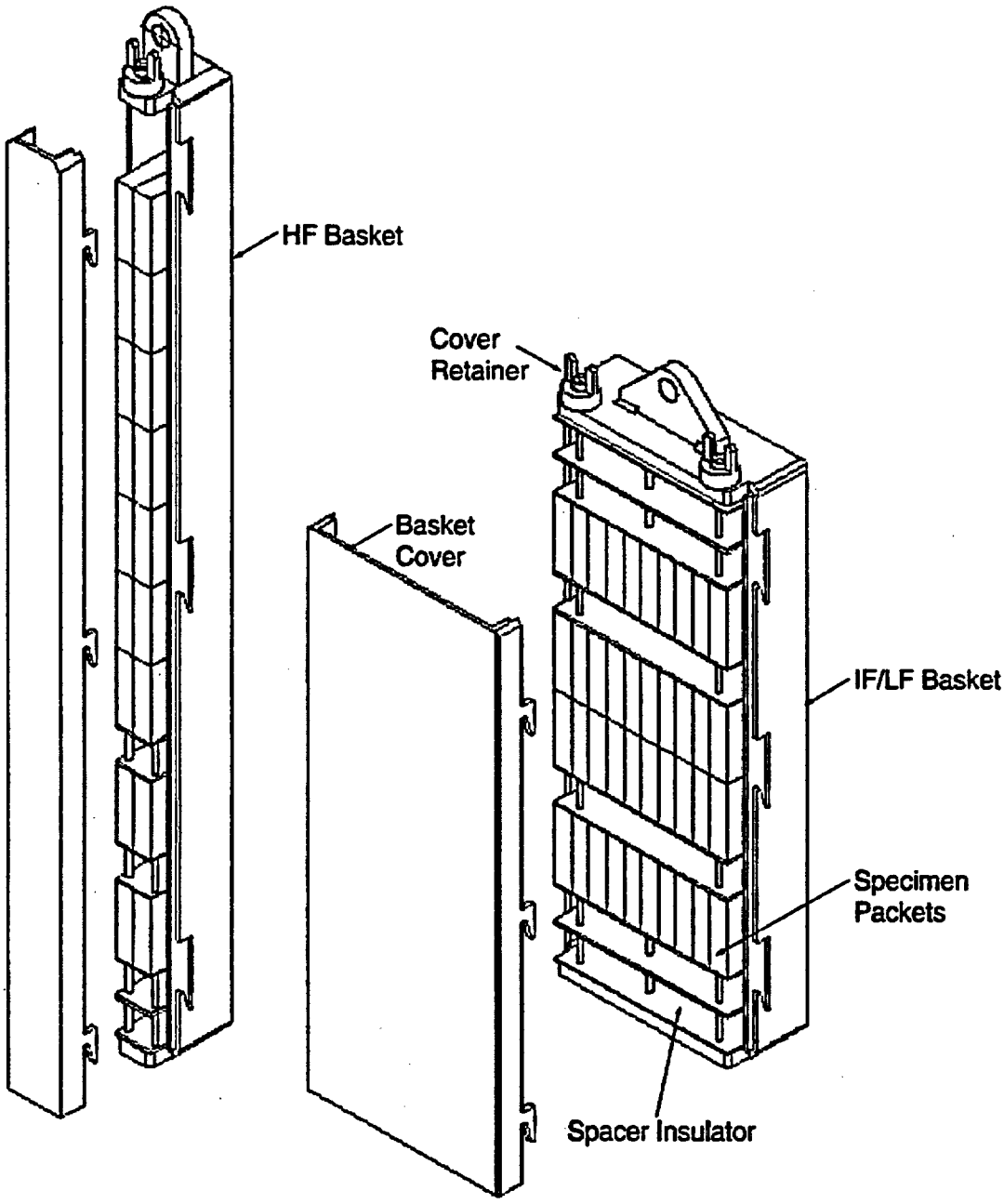

Figure 3-1 Specimen Baskets in the IVAR Facility

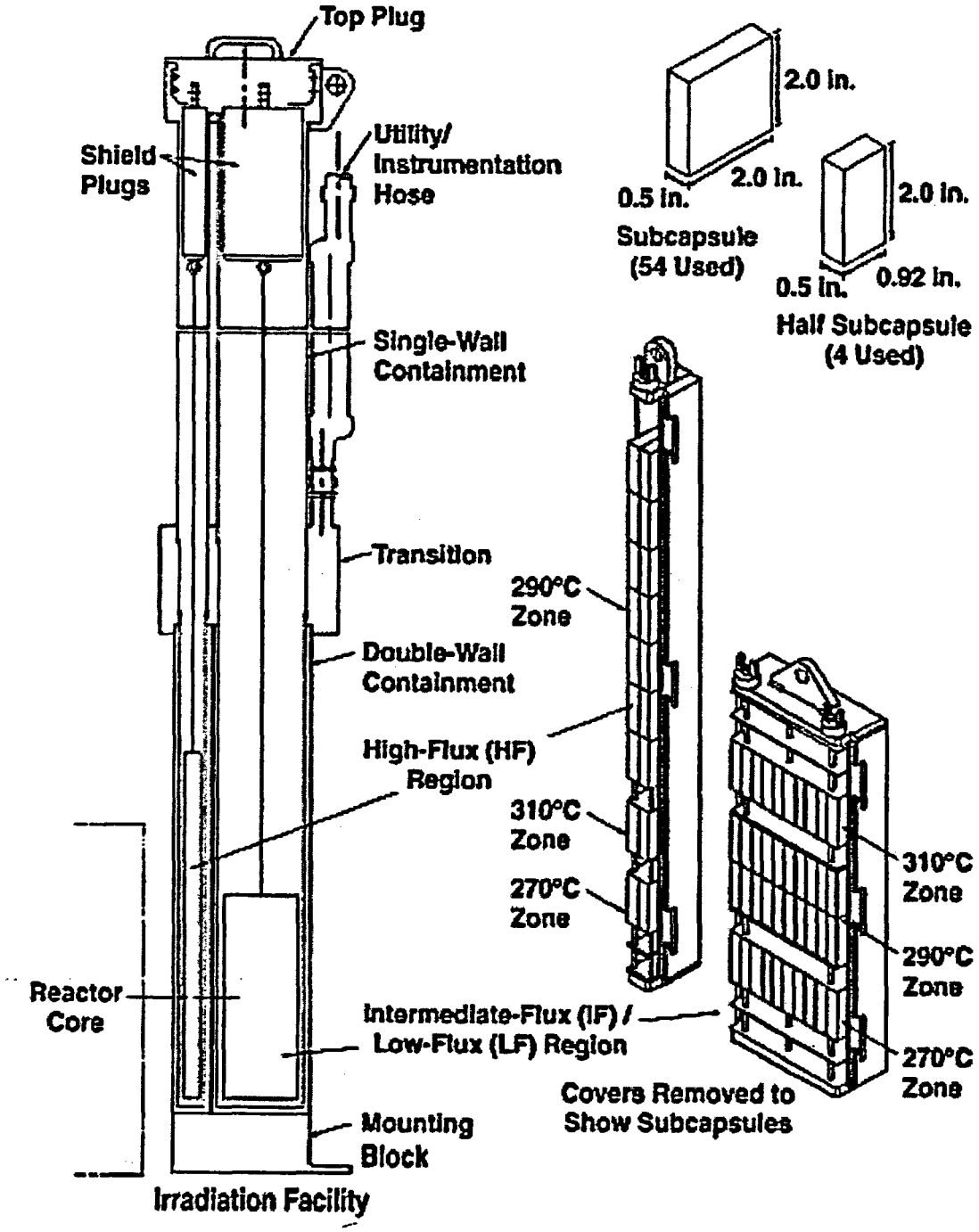

Figure 3-2 Schematic Design of the IVAR Irradiation Facility

Table 3-6. Specimen Loadings for Capsules T4 and T14

material	T4			T14	
	tensile	SANS	wafer	tensile	SANS
ORNL Midland Weld		1	1	3	1
ORNL 73 Weld	3	2	1	3	1
ORNL A302b	3	1		3	1
ORNL HSST02 plate	3	2		3	1
B.W. A508 plate				3	
B.W. A weld			1	3	
B.W. B weld		1	1	3	1
B.W. C weld		1	1	3	1
B.W. 62 weld	3	1		3	1
B.W. 63 weld	3	1		3	
B.W. 65 weld	3	1		3	
B.W. 67 weld	3	1		3	
Rolls Royce WV		1		3	1
Rolls Royce WG		1		3	1
Rolls Royce WP		1		3	1
EPRI C weld	3	2	1	3	1
JRQ	3	1	1		
CM1				4	
CM2				4	
CM3	4	1	1	4	1
CM4				4	
CM5				4	
CM6				4	
CM7				3	
CM8				4	
CM9				4	
CM10	4	1		4	1
CM11	4	1		4	1
CM12				4	
CM13	3	1		3	1
CM14				4	
CM15	3	1		3	1
CM16	4	1		4	1
CM17	3	1		3	1
CM18	4	1	1	4	1
CM19	4	1	1	4	1
CM20	4	1	1	4	1
CM21	4	1		4	1
CM22	4	1		4	1
CM23				4	
CM24				4	
CM25				4	
CM26				4	
CM27				4	
CM28				4	
CM29				4	
CM30				4	
CM31				4	
LA	3	1	1	3	1
LB	3	1		3	1
LC	3	1	1	3	1
LD	3	1	1	3	1
LG	3	1		3	1
LH	3	1		3	1
LI	3	1	1	3	1
LJ	3			3	
LK	3	1		3	1
LO	3	1	1	3	1

Table 3-7. Capsule loading for VSR

Stress Relief time				Alloy					
And temperature	CM3	CM5	CM11	CM12	CM13	CM16	CM18	CM19	CM20
590°C 24h	2t*	2t	2t, 1s	2t	2t	2t	2t	2t	2t
	1w	1w	1w	1w	1w	1w	1w	1w	1w
590°C 48h	2t	2t	2t	2t	2t	2t	2t	2t	2t
590°C 96h	2t	2t	2t	2t	2t	2t	2t	2t, 1s	2t
	1w	1w	1w	1w	1w	1w	1w	1w	1w
607°C 12h	2t	2t	2t	2t	2t	2t	2t	2t, 1s	2t
	1w	1w	1w	1w	1w	1w	1w	1w	1w
607°C 24h	2t	2t	2t, 1s	2t	2t	2t	2t, 1s	2t, 1s	2t, 1s
607°C 48h	2t	2t	2t	2t	2t	2t	2t	2t	2t
607°C 96h	2t	2t	2t, 1s	2t	2t	2t	2t	2t, 1s	2t
	1w	1w	1w	1w	1w	1w	1w	1w	1w
624°C 12h	2t	2t	2t	2t	2t	2t	2t	2t	2t
624°C 24h	2t	2t	2t, 1s	2t	2t	2t	2t	2t, 1s	2t
624°C 48h	2t	2t	2t	2t	2t	2t	2t	2t	2t
	1w	1w	1w	1w	1w	1w	1w	1w	1w
641°C 6h	2t	2t	2t	2t	2t	2t	2t	2t	2t
	1w	1w	1w	1w	1w	1w	1w	1w	1w
641°C 12h	2t	2t	2t	2t	2t	2t	2t	2t, 1s	2t
641°C 24h	2t	2t	2t, 1s	2t	2t	2t	2t	2t	2t
	1w	1w	1w	1w	1w	1w	1w	1w	1w
As-tempered	2t	2t	2t, 1s	2t	2t	2t	2t	2t, 1s	2t
	1w	1w	1w	1w	1w	1w	1w	1w	1w
607°C 24h, air cool	2t	2t	2t	2t	2t	2t	2t	2t, 1s	2t

* t = tensile, w= wafer, s=SANS specimen

Table 3-8. Capsule loading for PB

Material	tensile	SANS	wafer
CM1 as tempered	2	2	3
CM2 as tempered	2		3
CM3 as tempered	2		8
CM4 as tempered	3	2	5
CM5 as tempered	3	2	5
CM6 as tempered	2	2	3
CM7 as tempered	2		3
CM8 as tempered	3		3
CM9 as tempered	3		3
CM10 as tempered	2		3
CM11 as tempered	2		3
CM12 as tempered	2	2	3
CM13 as tempered	2	2	3
CM14 as tempered	2		3
CM15 as tempered	2		3
CM16 as tempered	2	2	3
CM17 as tempered	2		2
CM18 as tempered	3	2	3
CM19 as tempered	11	2	11
CM20 as tempered	3	2	3
CM21 as tempered	3	2	3
CM22 as tempered	3	2	3
CM23 as tempered	2		3
CM24 as tempered	2		3
CM25 as tempered	2		3
CM26 as tempered	2		3
CM27 as tempered	2		3
CM28 as tempered	2		3
CM29 as tempered	2		3
CM30 as tempered	2		3
CM31 as tempered	2		3
CM5 aged 480°C 100h	2		3
CM8 salt quenched 400°C	2		3
CM12 SR 600°C 8h	2	2	3
CM18 SR 600°C 40h	2	2	3
CM19 SR 600°C 8h	2	2	3
CM19 SR 600°C 40h	2	2	3
CM19 SR 600°C 80h	2	2	3
CM19 salt quenched 500°C	2		3
CM20 SR 600°C 40h	2	2	3
CM20 salt quenched 500°C	2		3
CM23 salt quenched 400°C	2		3
CM26 aged 480°C 100h	2		3
LA	2	1	2
LB	2		2
LC		1	
LD	2	1	2
LG	2	1	2
LH	2	1	2
LI	2	1	2
LJ	2	1	2
LK	2	1	2

using cross sections from the preliminary ORNL report indicated good agreement with the previous estimate of flux levels. More recently, ORNL remapped the flux distribution in and around the IVAR facility based on new cross sections and neutron transport calculations. The estimated flux levels were generally slightly lower, but in most cases only by a few percent. However, several locations showed flux reductions as large as 7%. The fluence estimates presented in this report (in units of 10^{23} n/m^2 E > 1 MeV) are based upon the most updated flux levels at each position in the IVAR facility. The fluence estimates for the T4, T14, and VSR capsules are shown in Table 3-9. Final fluences will be based on any further updates of the activation cross sections and activity measurements on the dosimetry wires from individual capsules.

In the case of the PB irradiation, specimens were loaded into a pair of aluminum sub-capsules specifically designed to fill the space between the clevis tabs in a row of large crack arrest specimens. These specimens were included in a large instrumented irradiation capsule built by ORNL as part of the HSSI program. This capsule was irradiated at FNR during the latter part of 1993. Temperature was measured by internal thermocouples and dosimetry was performed by ORNL [Remec, 1998]. The irradiation conditions for the PB irradiation are also given in Table 3-9.

3.3 Tensile Testing

Following irradiation, the IVAR capsules were returned to UCSB where specimens were removed, sorted and cleaned to remove any minor surface contamination . Following careful measurements of the gauge dimensions to about ± 5μm, the tensile specimens were loaded into a linear carriage for automated testing. The automated tensile tester consists of a screw driven load frame, a linear drive, a pneumatically actuated hydraulic upper grip and a computer control and data logging system. The linear carriage holds 29 tensile specimens and serves as the lower grip. It mounts on the linear drive. During a testing sequence, the drive precisely locates a specimen under the upper grip. The upper grip closes, and motion of the is crosshead initiated. Loads are measured with a precision calibrated load cell aligned with the upper grip. Displacements between the bottom of the upper grip and the lower carriage are measured by an LVDT. The load-displacement signals are digitized and continuously recorded and monitored on a desktop computer during a test. The crosshead is stopped when the load has decreased 10% below it's maximum value. The upper grips are opened and another specimen is positioned for the next test. Yield strength, ultimate tensile strength, and uniform elongation are immediately calculated from the load-displacement data and specimen dimensions, and loaded into a data base. However, each test record is also examined to verify the results generated by the computer. Three calibrated standard specimens are included in every carriage to ensure data reproducibility.

A minimum of two tensile tests were conducted for each irradiation and unirradiated control condition. Additional tests were typically carried out on unirradiated specimens, as well as the irradiated specimens in a number of cases. Yield stress changes ($\Delta\sigma_y$) were determined by subtracting the average unirradiated (baseline) from the average irradiated yield stress. As noted previously, both microhardness measurements and billet location tracking were used to reduce scatter in $\Delta\sigma_y$ due to variability in the baseline properties. This included both matching irradiated and control specimens and screening the data for cases where the accuracy of $\Delta\sigma_y$ was in some question. In a very few cases this reduced the number of test points below the normal minimum of two.

The estimated uncertainties in individual $\Delta\sigma_y$ values were based on the root of the sum of the squares of the standard errors (or the $\Delta\sigma_y$ range in the case of only two tests) of the unirradiated and irradiated data. The estimated uncertainties in $\Delta\sigma_y$ averaged about ±11 MPa, but where significantly higher in some cases. The largest uncertainties were experienced in the VSR study.

Table 3-9. Irradiation Conditions

Capsule	Irradiation Conditions		
	Flux (10^{16} n/m^2-s)	Fluence (10^{23} n/m^2)	Temperature (°C)
T4	0.97	0.75	290
T14	0.32	0.48	290
VSR	0.97	0.85	290
PB	0.7	1.0	288

This led to a data screening procedure, described in Section 6.1, for the $\Delta\sigma_y$ used to estimate matrix copper levels.

3.4 Small Angle Neutron Scattering

The Small Angle Neutron Scattering (SANS) measurements were performed at the National Institute of Standards and Technology (NIST). Details of the experiments and data analysis are present elsewhere [Mader, 1995; Wirth, 1998]. The approach can be briefly summarized as follows. All measurements were made in a strong (1.8±0.1T) magnetic field oriented in the $\phi = 0°$ horizontal direction. The scattering at small angles, $\theta \leq 8°$, from a well collimated beam of cold neutrons with a wavelength of $\lambda \sim 0.5$ nm, was measured on a 64x64 cm position sensitive detector located about 2 meters from the sample and rotated off the beam axis by 5° to increase the scattering vector. The detector records the number of scattered neutrons detected in each 0.5x0.5 cm pixel element. The irradiation-induced feature scattering cross-sections are obtained by subtracting off the corresponding, properly normalized (measurement time, sample volume and attenuation) counts from: a) background radiation; b) parasitic scattering not associated with the sample itself; and c) scattering from an unirradiated control. The corrected defect scattering data are then converted to an absolute differential defect scattering cross-section $d\Sigma/d\Omega(q, \phi)$ by a normalization to corresponding measurements on a water reference sample with a 'known' isotropic scattering cross section. (= 0.88 /cm-ster) [Wirth, 1998].

The differential coherent small angle cross section, $\Sigma/d\Omega$, for a dilute distribution of single type scattering feature is given by [Kostorz; Guinier and Fournet, 1955]

$$d\Sigma/d\Omega(q,\phi) = NV^2 \Delta\rho^2 F(qr) \qquad (3\text{-}1)$$

where:

a) N, r and V are the number density, characteristic size (e.g., radius) and volume of the feature, respectively. b) F is the scattering function which depends on feature size (r) and shape, and the scattering vector, $q = 4\pi\sin(\theta)/\lambda$, where θ is half the scattering angle (2θ), and λ is the neutron wavelength; for spherical features,

$$F(qr) = 3\{[\sin(qr) - qr\cos(qr)]/(qr)^3\}^2 \qquad (3\text{-}2)$$

c) $\Delta\rho$ is the difference (or contrast) between the scattering length density of the feature (f) and the matrix (m) or ($\Delta\rho = \rho_f - \rho_m$); here ρ is the scattering length density defined as $\rho = b/\Omega$ where b is the average scattering length (nuclear or magnetic in the feature or matrix) and Ω is the corresponding average atomic volume. Coherent small angle scattering is produced by both nuclear $\Delta\rho_N$ and magnetic $\Delta\rho_M$ contrast, and the total scattering contrast ($\Delta\rho^2$) is given by

$$\Delta\rho^2 = \Delta\rho_N^2 + \Delta\rho_M^2 \sin^2(\phi_s) \qquad (3\text{-}3)$$

where ϕ_s is the angle with respect to the applied magnetic field.

As noted above, the $d\Sigma/d\Omega(q,\phi_s)$ data include contributions from both nuclear (N) and magnetic scattering (M), thus

$$d\Sigma/d\Omega(q,\phi_S) = d\Sigma/d\Omega_{N}(q) + d\Sigma/d\Omega_M(q)\sin^2(\phi_S) \qquad (3\text{-}4)$$

The $d\Sigma/d\Omega$ increases from purely nuclear scattering at $\phi_s = 0°$ to nuclear plus magnetic scattering at $\phi_s = 90°$. The $d\Sigma/d\Omega$ data at each detector pixel were averaged over a set of specified magnetic angle sectors, $\phi_i \pm \Delta\phi_i$, for a set of discrete $q_j \pm \Delta q_j$. The corresponding standard deviations were calculated for each averaged defect cross section.

The nuclear scattering, $\Delta\rho_N^2$, depends on the feature composition. It is assumed that the features are magnetic holes in a saturated ferromagnetic iron matrix; hence, that the magnetic scattering, $\Delta\rho_M^2$, is independent of composition [Fint, 1990; Mader, 1995; Wirth, 1998]. This is useful in two ways. First, the magnetic to nuclear scattering ratio (M/N) provides information about the composition of the scattering feature (see below). Second, good absolute estimates of the number density and volume fraction of the scattering features can be obtained from $d\Sigma(q)/d\Omega_M$, since $\Delta\rho_M^2$ is precisely known. Single, and in some cases multiple, feature fits are made to the $d\Sigma/d\Omega(q,\phi)$ data based on the M/N ratio determined from $d\Sigma_\phi/d\Omega$ vs. $\langle\sin^2(\phi)\rangle$ fits typically over a q-range where irradiation-induced feature scattering is dominant.

The $d\Sigma/d\Omega$ data was analyzed assuming the size distribution of the features can be approximately described by a log-normal distribution characterized by a mode radius r_m and radius distribution parameter, β. Non-linear least squares fits to the data were carried out to determine r_m, β and $d\Sigma/d\Omega_M(\phi = 0)$. These fit parameters can be related to the average of the radius cubed ($\langle r^3\rangle^{1/3} = \langle r\rangle$), number density (N) and volume fraction (f_v) of the features as [Fint, 1990; Mader, 1995; Wirth, 1998]

$$\langle r\rangle = r_m \exp(0.75\beta^2) \qquad (3\text{-}5a)$$

$$N = (3/4\pi)^2\{\exp(-9\beta^2)/[r_m^6\Delta\rho^2]\}\, d\Sigma/d\Omega_M(0) \qquad (3\text{-}5b)$$

$$f_v = (3/4\pi)\{\exp(-6.75\beta^2)/[r_m^3\Delta\rho^2]\}\, d\Sigma/d\Omega_M(0) \qquad (3\text{-}5c)$$

Note the β and r_m parameters have a large covariance coefficient, hence, cannot be independently determined with good precision. This has relatively little effect on the estimates of $\langle r\rangle$ and f, but results in larger uncertainties in N. A fixed β of 0.4 was used for most single defect fits to provide a more self-consistent basis to assess trends in $\langle r\rangle$, f and, particularly, N.

As noted previously the M/N ratio provides information on the composition of the scattering feature. It is useful to characterize the relative strengths of nuclear and magnetic scattering as $R = \sqrt{N/M}$ ($= \Delta\rho_N/\Delta\rho_M$), rather than M/N, since it is approximately a simple linear function of the

composition, $R = C_{Cu}X_{Cu} + C_{Mn}X_{Mn}$, where the C's are known coefficients and X's are the atom fractions [Mader, 1995; Wirth, 1998]. For example, the nominal R for a spherical void and a pure copper precipitate in an iron matrix are about 1.58 and 0.36, respectively [Wirth, 1998]. If the copper-rich precipitates (CRPs) contain more than two elements (e.g. Cu, Mn and Ni), the R is not a unique quantity. However, R constrains and can be used along with other information to estimate CRP composition. The other information includes: a) the CRP volume fraction; b) the amount of copper (and other elements) in the CRPs based on independent measurements of changes in the matrix levels; c) use of isotopically modified constituents; d) data from atom probe and other microanalytical techniques such as positron annihilation spectroscopy; e) thermodynamic calculations; and f) hardening measurements [Wirth 1998].

3.5 Field Emission Gun Scanning Transmission Electron Microscopy

Field Emission Gun Scanning Transmission Electron Microscopy (FEGSTEM) was performed on a number of alloys in the unirradiated condition to evaluate the amount of copper in solution as a function of heat treatment. The FEGSTEM studies were performed at AEA Technology in a collaborative program with UCSB. Standard 0.5x3mm transmission electron microscopy (TEM) specimens were examined in a VG HB501 STEM and a Philips EM430 conventional TEM. The STEM is fitted with a parallel electron energy loss spectrometer (PEELS) and an energy-dispersive X-ray (EDX) detector. The relative concentration of copper interacting with the electron beam is determined from the ratio of the counts under the copper peak to the counts under the peak of a reference element, typically taken as iron [Kenway-Jackson, 1993].

The measurement of matrix copper with the STEM EDX was determined as follows [Kenway-Jackson, 1993]. The foil precisely positioned in the STEM in a specially-modified holder of copper-free construction. X-ray spectra were recorded from regions free of any visible precipitates using the so-called spot mode or small area mode, where the small areas were fitted between dislocations. Precipitates with diameters larger than about 5nm were also generally avoided by the small area measurements. The small area measurements in the STEM determine the average copper content between dislocations and large precipitates, while the spot analyses measure the copper content between dislocations and all visible precipitates. The visibility limit of the HB501 STEM is a precipitate diameter of around 2nm. The relationship of these two types of measurement to the bulk copper content and to each other, and the variation within a series of measurements of a given type, changes with the type and extent of precipitation, as explained below:

1. When no precipitation has occurred and the dissolved copper is evenly distributed, both spot and small area measurements are the same as the bulk measurement and the distribution about the mean will be relatively narrow.

2. When heterogeneous precipitation occurs on dislocations and grain boundaries, then the small area and spot measurements will again be tightly distributed about a mean, but the mean will be less than the bulk copper level. The difference between the bulk and the mean represents the amount of copper heterogeneously precipitated.

3. When some homogeneous matrix precipitation occurs and the precipitates are extremely fine (diameter, $d < 2$nm), the precipitates are not easily visible in the STEM images and are included in both the spot and the small area measurements. In this case the small area measurements overestimate the dissolved copper content. Since the spot measurements, randomly sample both matrix and precipitates, the average spot measurement will be equal to the average small area measurement. However, the distribution of individual spot measurements

becomes skewed and/or broadened, and the lower end of the distribution corresponds more closely to the true matrix level of copper.

4. When homogeneous precipitation has occurred and the precipitates have grown to more than 2nm, the precipitates are visible in the STEM images and can be avoided during spot analysis. Under these conditions, the spot measurement distribution will once again become tight about a mean that represents the best estimate of the matrix copper level.

5. When further growth of matrix precipitates results in diameters well over 5nm, the precipitates can be avoided by the small area measurements as well as the spot measurements; and the spot and small area measurements will again be equivalent. Their means will provide a best estimate of the matrix solute content. The difference between the bulk and small area measurements will then include a contribution from the large matrix precipitates as well as the precipitates on dislocations and grain boundaries.

Hence, the differences between bulk (or large area), small area, and spot measurements as well as the distribution of spot and small area measurements provide a method of estimating both the copper in solution as well as the size and spatial distribution of copper precipitates. When both heterogeneous and homogeneous precipitation occur concurrently (the most typical situation), the bulk measurement will be greater than the STEM small area measurement, and the STEM small area measurement will be greater than the spot measurement. The difference between the bulk and STEM small area measurements will then show the extent of heterogeneous precipitation, the difference between the STEM small area and spot measurements indicates the extent of homogeneous precipitation producing precipitates with diameters greater than 2nm. The distribution of the spot measurements will give information on the precipitates of diameter less than 2nm. Once again, in this case the best estimate of the dissolved copper level is given by the spot measurements. Depending on the situation, the best estimate of copper in solution in the presence of small precipitates can be obtained by either the mean of the lower peak in a spot distribution or the mean of the lowest four measurements. Summarizing, the amounts of copper tied up in the various precipitate size categories can be taken as:

1. The dislocation precipitate content is the bulk copper level minus the mean of the small area

2. The homogeneous precipitate content (diameters above 2nm) is the mean small area level minus the mean spot level

3. The homogeneous precipitate content (diameters below 2nm) is the mean spot level minus the matrix level

4. The matrix copper level taken as the mean of the four lowest spot measurements, or the mean of lowest peak in spot distribution where relevant.

These working rules to establish the matrix copper level from FEGSTEM data were developed based on extensive Monte Carlo studies of STEM electron beam interactions with a range of precipitate structures. However, the overall accuracy is limited and in general is of order ±0.05% copper. The limitations of even these highly sophisticated measurements and analysis methods demonstrate the challenges to precisely characterizing the effects of pre-precipitation during stress relief on matrix copper levels.

3.6 Electrical Resistivity Measurements

Electrical resistivity (expressed in μΩ-cm in this study) is a function of the solute content of the matrix, and it can be precisely measured [Rossiter, 1991; ASTM, 1987]. Tests were

performed on tensile specimens used in the irradiation experiments. The width and thickness of the guage section of the specimens were carefully measured to ±5μm. The specimen was mounted and aligned on a Teflon support block containing two copper electrodes that contacted the tab ends of the specimen. These electrodes were attached to a DC constant current power supply. An upper block containing two copper knife edge electrodes was lowered onto the specimen, guided by alignment pins. The knife edges were located at a precisely known distance apart along the specimen gauge section. They were loaded on the specimen with a fixed weight. A current was applied and measured with a precision ammeter. The corresponding voltage drop across the knife edge electrodes was measured with a high precision DC nanovoltmeter. The current and voltage was read by a desktop computer, and along with the specimen dimensions and knife edge spacing were used to compute the resistivity. The entire apparatus was maintained in an electrically and thermally insulated container The sample temperature was measured with a thermocouple attached to the support block adjacent to the specimen. Tests were performed at ambient temperature, in the range of about 20-25°C. In this range, the resistivity was linear with temperature with a coefficient of about 0.08 μΩ-cm/°C. The resistivities was normalized to a reference temperature of 23°C for data intercomparisons. Resistivities of the alloys examined in this study ranged from about 10-27 μΩ-cm. Typical uncertainties were on the order of ±0.05 μΩ-cm for a single specimen, and up to about ±0.5 μΩ-cm between specimens of the same material. The average uncertainty was about ±0.2 μΩ-cm.

3.7 Seebeck Coefficient Measurements

Similar to resistivity, the Seebeck coefficient of a metal or alloys is very sensitive to the concentration of dissolved solutes [Pollock, 1991; Miloudi et. al, 1999, 2000]. The Seebeck effect relates to the electric potential difference established between junctions of dissimilar conductors in a temperature gradient. Thermoelectric power derives from three interrelated effects: the Peltier effect, the Thomson effect, and the Seebeck effect. These form the basis for both thermocouples and thermoelectric power generators [Pollock, 1991]. As noted above, the Seebeck effect occurs when dissimilar conductors in contact form a circuit that produces an electric potential when the two junctions are held at different temperatures. The Seebeck coefficient, S (in units of μV/°K) is the open circuit potential divided by the temperature difference.

The Seebeck coefficient is determined by measuring the potential difference of an open circuit composed of a pure copper reference material and the samples, typically in the form of tensile specimens. Thus the potential is for the sample relative to copper and is not an absolute value. The absolute value is found by correcting for the absolute potential of the reference material, in this case copper. The sample was aligned in a fixture and held against the copper electrodes with a fixed weight. One of the electrodes was at ambient temperature while the other was heated with a resistance tape to about 10° higher. The temperatures in the knife edges just below the sample were measured with thermocouples to within ±0.1°C. The potential difference was measured with a precision nanovoltmeter to within ±1.5μV. Care was taken to avoid noise or spurious electronic signals, and copper leads of equal length were used to minimize any extra potential not associated with the specimen itself. The instrument was calibrated with copper and aluminum reference materials with known absolute values of S. A nominal temperature coefficient for S of 0.022 μV/°K^2 was used to correct the data to a nominal average sample temperature of 31°C. Typical uncertainties were ±0.05 μV/°K for a single specimen, and up to about ±0.5 μV/°K between specimens of the same material. The average uncertainty is about ±0.25μV/°K.

4 EFFECTS OF COMPOSITION ON IRRADIATION HARDENING AND EMBRITTLEMENT

The empirical trends of $\Delta\sigma_y$ variations with alloy composition are described in this section. The data are derived from the T4, T14, VSR and PB capsules. Except for the PB capsule, which contained specimens in the as-tempered heat treatment condition, or as otherwise noted, all the alloys are in a tempered plus standard stress relief condition. The heat treatment schedules are described in Section 3.

4.1 Summary of the Data Trends

4.1.1 Copper Bearing Alloys

Figure 4-1 plots the $\Delta\sigma_y$ of the intermediate nickel (0.74 to 0.88%) CM and LV alloys versus bulk copper content (Cu_{bk}). The data are from the T4, T14 and VSR capsules. Figure 4-1a presents results for the CM-series (CM3, 10, 11,12, 13,16 and 19) and 4-1b for the LV-series (LG, LH, LI, LC, LJ, LK), respectively. In both cases $\Delta\sigma_y(Cu_{bk})$ has a typical sigmoidal shape, with a low copper threshold region and a high copper saturation, followed by a decrease at very high copper levels. In between $\Delta\sigma_y$ increases rapidly with increasing Cu_{bk}.

Figure 4-2 shows the corresponding effects of nickel variations on $\Delta\sigma_y$ for intermediate and high copper steels. The data are from the T14 and PB capsules. Figure 4-2a shows data for the high copper (0.43%) CM-series (CM18, 19, 20). In all three cases, $\Delta\sigma_y$ increases approximately linearly with nickel, as $\Delta\sigma_y(Ni) = A + BNi$. The average zero-nickel intercept is A = 63± 6 MPa and the average slope is B = 117±8 MPa/%Ni. Figure 4-2b shows a similar plot for the intermediate copper (0.22%) CM alloys (CM15,16,17). In this case, the data for the as-tempered heat treatment condition from the PB capsule is included, since pre-precipitation is not expected to occur at these bulk copper levels (see Section 6). The $\Delta\sigma_y(Ni)$ intercept is A = 45±3 MPa and the slope B = 106±10 MPa/%Ni. Figure 4-2c compares the $\Delta\sigma_y(Ni)$ data for intermediate and high copper steels from the T14 capsule. Notably, nearly doubling Cu_{bk}, results in only relatively small increases in the $\Delta\sigma_y$, from about 18 MPa at low (0.0%) nickel to 32 MPa at the high (1.7%) nickel. Figure 4-2d plots $\Delta\sigma_y$ versus nickel for the high copper (0.40%) LV series. The corresponding data for the high copper CM-series is shown as small filled symbols. The $\Delta\sigma_y(Ni)$ is very similar for the CM and LV steels, with the exception of the LV data from the T4 capsule, which falls well below the other data trends. The LV steels also have a slightly higher average intercept of A = 71.8± 5 MPa than the CM alloys (A = 63 MPa for the CM alloys), and a lower nickel sensitivity with an average slope of B = 101± 15 MPa/%Ni (B = 117 MPa/%Ni for the CM alloys). However, in spite of these modest differences, overall the behavior of $\Delta\sigma_y(Ni)$ for the LV and CM alloys are very similar. These results clearly show that for intermediate-to-high copper steels, nickel is the dominant compositional factor controlling embrittlement.

Figure 4-3 plots $\Delta\sigma_y$ versus manganese content (0.0 to 1.65%) for the intermediate nickel (0.85%), high copper (0.42%) CM alloys (CM19,21,22), as well as the LV steel (LJ) from the T4 and T14 capsules. The $\Delta\sigma_y(Mn)$ is approximately linear, $\Delta\sigma_y(Mn) = A + BMn$, with an average slope of B = 31±5 MPa/%Mn. The $\Delta\sigma_y$ for the CM21 alloy with intermediate manganese (0.84%) falls somewhat above the linear trend line in both cases. Hence a $\Delta\sigma_y(Mn) = A + BMn + CMn^2$ type dependence may actually be more appropriate. The effect of manganese is larger for the intermediate flux, lower fluence T14 irradiation compared to the high flux T4 capsule. This difference is consistent with enhancement of a flux effect by manganese (and nickel) that is discussed in Appendix A.

Figure 4-4 plots $\Delta\sigma_y$ from the a) PB and b) T14 capsules for other compositional variations in intermediate and high copper CM alloys, including: i) a 10 wt.ppm boron addition to the

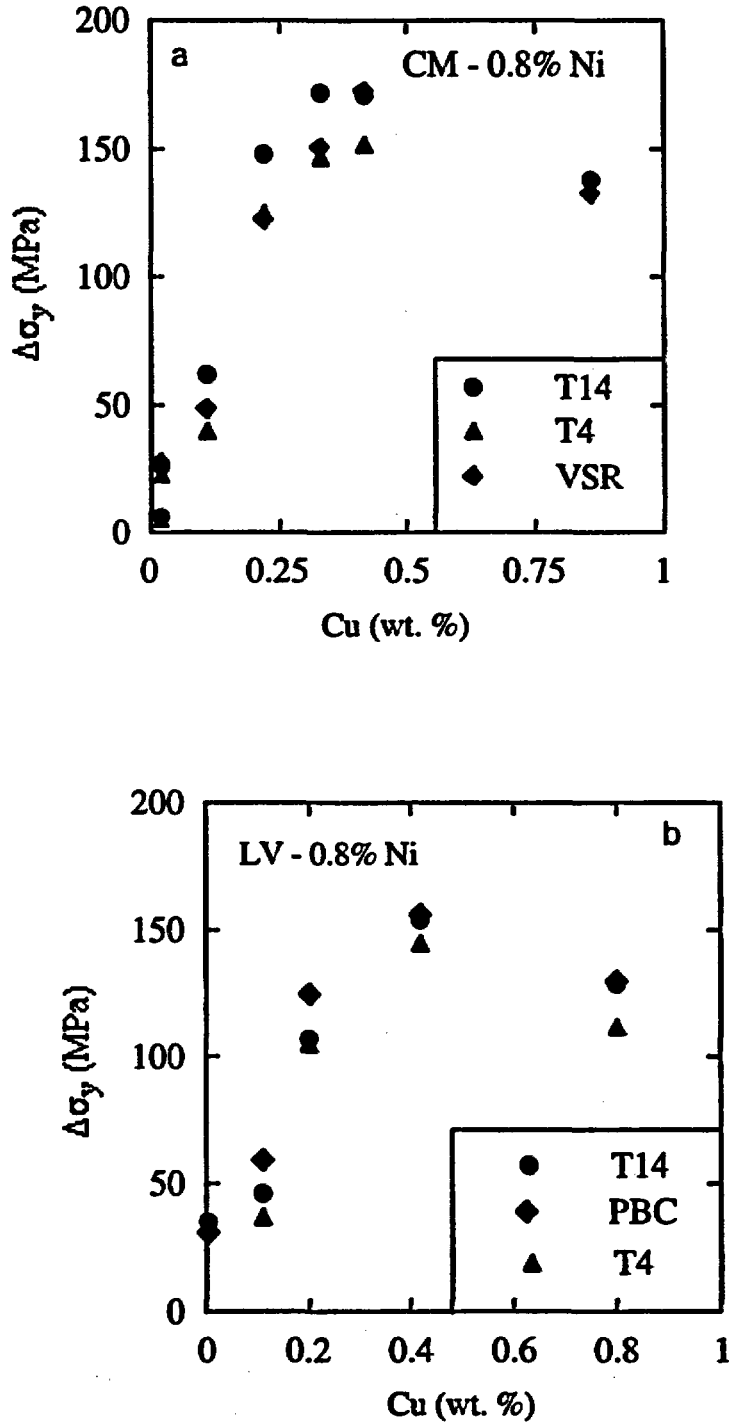

Figure 4-1 Variation of $\Delta\sigma_y$ with bulk copper in intermediate nickel alloys for the a) CM and b) LV series

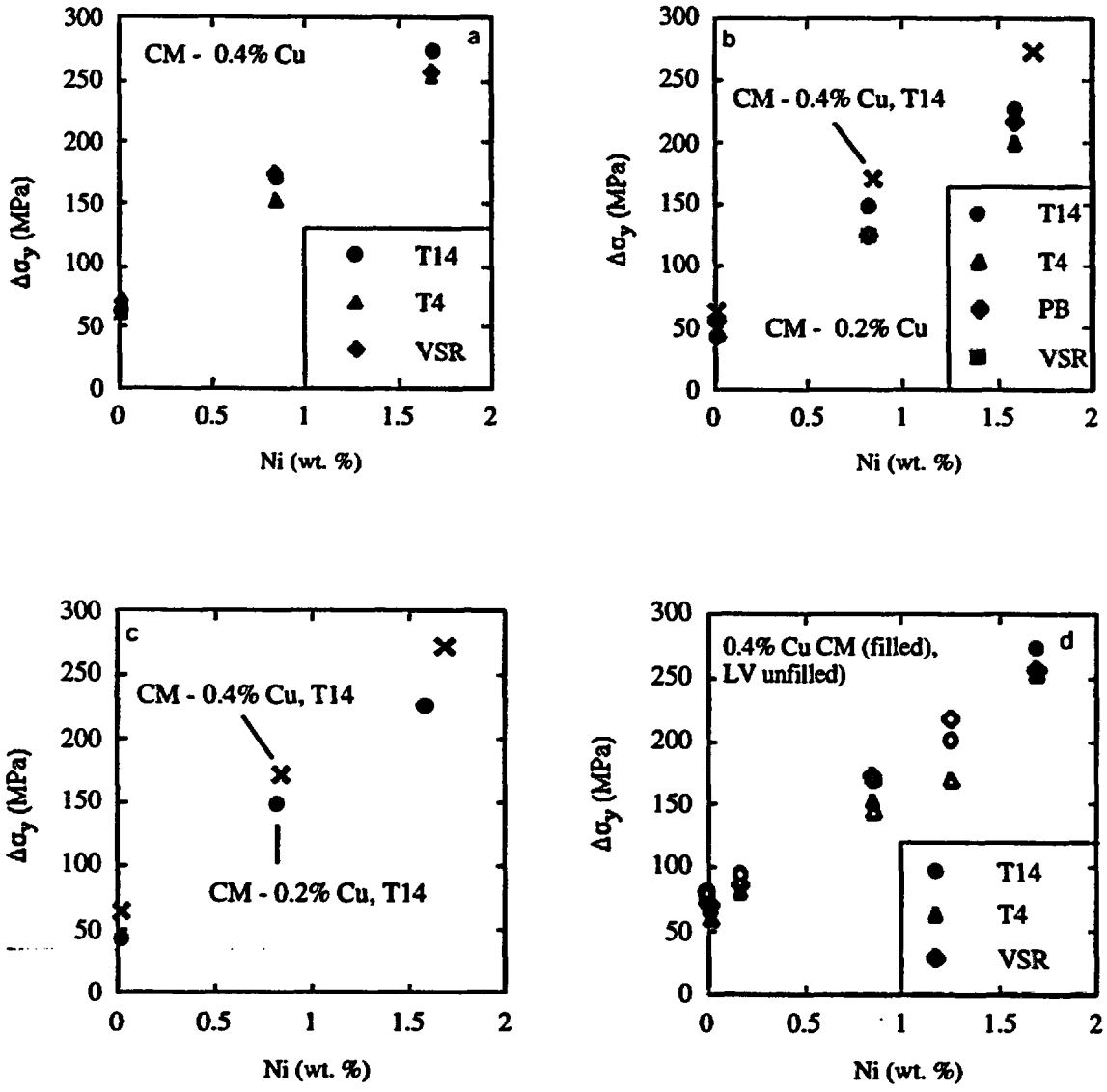

Figure 4-2 Variation of $\Delta\sigma_y$ with nickel for a) 0.4 copper and b) 0.2 copper CM alloys; c) comparison of $\Delta\sigma_y$ versus nickel for intermediate and high copper steels for T14; d) variation of $\Delta\sigma_y$ with nickel for high copper LV series steels (corresponding CM alloys shown for comparison as small filled symbols).

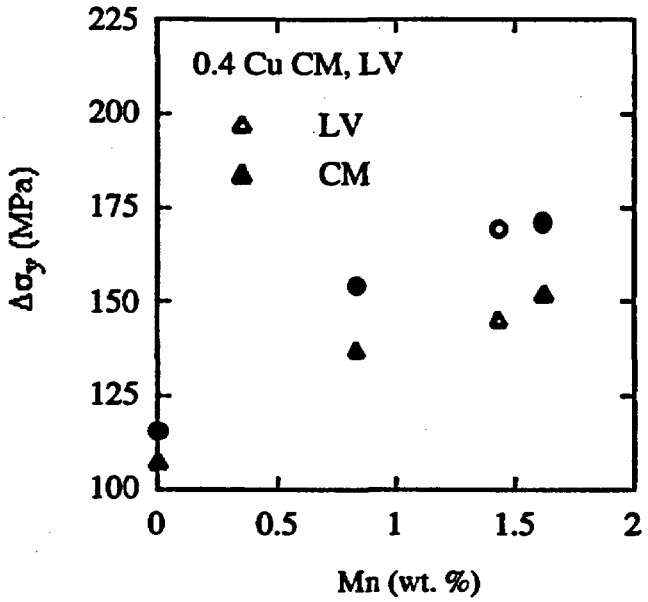

Figure 4-3 Variation of $\Delta\sigma_y$ with manganese for intermediate nickel, high copper CM and LV steels.

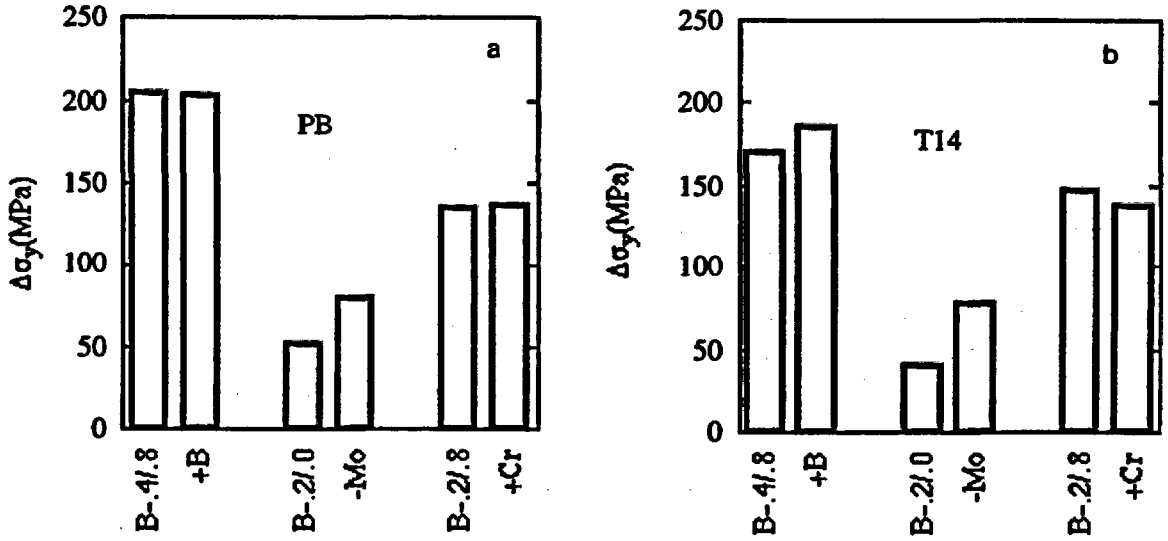

Figure 4-4 Variation of $\Delta\sigma_y$ with boron, molybdenum and chromium for a) PB and b) T14.

high copper (0.42%) and intermediate nickel (0.84%) alloy (CM27); ii) an intermediate copper (0.22%) low nickel (0.02%) alloy (CM29) with no molybdenum (0.02% versus a nominal value of 0.5%); and iii) an intermediate copper (0.22%) and nickel (0.85%) alloy (CM30) with a 0.42% chromium addition. The $\Delta\sigma_y$ for the modified alloys are compared to the corresponding base steels (CM27 vs. CM19, CM29 vs. CM15 and CM30 vs. CM16). The alloys in the PB and T14 capsule are in the as-tempered and standard stress relief conditions respectively. The boron and chromium additions have a small to negligible effect. However, the $\Delta\sigma_y$ in steels without molybdenum is larger in both cases.

While the overall effect of deleting molybdenum is modest (a difference of about 30±6 MPa), this trend is consistent with a lower dispersed obstacle contribution to the unirradiated yield strength in this alloy, that lacks fine scale Mo_2C carbides. As discussed in Section 6, this behavior arises from the fact that the individual strengthening contributions from the unirradiated (σ_u) and irradiation induced (σ_i) dispersed dislocation obstacles must be combined or superposed. For strong unirradiated obstacles and weaker irradiation induced obstacles, the superposition law falls between linear and root sum square limits. Thus for a given σ_i, the net $\Delta\sigma_y$ decreases with increasing σ_u. (see Equation 6-4 below). As a simple example, taking σ_u as 200 and 35 MPa for CM15 and CM29 respectively and assuming a normal CRP superposition parameter of θ = 0.4, a common σ_i = 95 MPa results in a $\Delta\sigma_y$ of 51 (CM15) vs. 78 MPa (CM29), respectively. These are close to the observed values.

Table 4-1 summarizes the trends discussed in the previous paragraphs. Note the magnitudes given are illustrative for 290°C, 0.5×10^{23} n/m^2 low-to-intermediate flux irradiations of intermediate-to-high copper alloys in the standard stress relief condition. The specific values must be viewed as representative, since detailed behavior depends on the entire combination of variables.

4.1.2 Low Copper Alloys

Figures 4-5a, b and c plot $\Delta\sigma_y$ from the T14 and PB capsules versus phosphorous content (0.002 to 0.047%) for low copper (0.02%) CM alloys with low (0.01%), intermediate (0.86%) and high (1.53%) nickel. The effects of increasing nickel are shown in Figures 4-5a (low, CM1, 2), 5b (intermediate, CM3, 4, 5) and 5c (high, CM6, 7), respectively. The $\Delta\sigma_y$ increases approximately linearly with phosphorous in all cases, $\Delta\sigma_y(P) = A + BP$. The slopes of $\Delta\sigma_y(P)$ range from B = 550 to 1450 MPa/%P. Plots of the B versus nickel shown Figure 4-5d do not seem to show any systematic trend. However, the data from the T14 capsule are more scattered, and the high nickel point seems to be anomalously low. The slopes average 1165 MPa/%P with the T14 point included, and 1285 MPa/%P if it is deleted. Figure 4-5e compares the $\Delta\sigma_y(P)$ for alloys with two copper levels (0.02% and 0.11%). The effect of phosphorous on $\Delta\sigma_y$ for the PB capsule (filled symbols) is very similar in both cases. However, the apparent phosphorous sensitivity of the T14 capsule data is higher for the alloy with 0.02% copper and much lower for the alloy with 0.11% copper, with B = 1931MPa/%P and 0 MPa/%P, respectively. Again, these differences may be simply a consequence of the larger scatter in the steels in the T14 capsule. Alternately it may indicate that higher copper decreases the effect of phosphorous for steels in the standard stress relief (T14) versus as-tempered (PB) condition.

The effect of nickel on low (0.02%) copper steels was shown in Figure 4-5a to 4-5c. Cross plots of the CM data are shown in Figure 4-6 for low (Figure 4-6a) and high (Figure 4-6b) phosphorous. In three out of the four cases the $\Delta\sigma_y$ shows a clear linear trend, $\Delta\sigma_y(Ni) = A + BNi$, with an average slope of B = 20±4 MPa/%Ni. The slope for the high phosphorous T4 capsule data is much less (5.4 MPa/%Ni) and the individual $\Delta\sigma_y$ are more scattered. Given the general scatter of the $\Delta\sigma_y$ values, such differences are not unexpected. If this data point is included the nickel sensitivity slope decreases to 16 MPa/%Ni.

Table 4-1. Summary of Compositional Dependence of Hardening in High Copper Steels

Variable	Dependence	Interactions	Magnitude
copper	threshold-saturation sigmoidal	nickel, manganese, HT† (see Section 5)	~ 50 MPa (0.0%Ni)* ~ 150 MPa (0.8%Ni)* ~ 240 MPa (0.8%Ni)* *@ 0.3% Cu
nickel	~ A + BNi	copper, managnese, HT (see section 5)	B ~ 110 MPa%Ni
manganese	~ A + BMn	copper, managnese, HT (see section 5)	B ~ 30 MPa/%Mn
molydebdnum	not established	superposition of the irradiated/unirradiated obstacle strengths	~ -30 MPa with vs. without molydebdnum
boron, chromium	not established		probably minor

†HT=heat treatment

Figure 4-7 plots $\Delta\sigma_y$ of low (0.02%) copper CM alloys (CM8, 3, 9) from the T14 and PB capsules versus the manganese content. The $\Delta\sigma_y$ data scatter around a linear trend, $\Delta\sigma_y(Mn) = A + BMn$, with a slope of $B = 10\pm1$ MPa/%Mn.

Figure 4-8 shows histogram plots of $\Delta\sigma_y$ from the T14 and PB capsules for alloys with single element compositional variations. These include: low (0.02%) copper CM alloys (CM23 to 27) with a) low (0.05%), intermediate (0.15%) and high (0.3%) carbon (CM23, CM3, CM24), b) high nitrogen (CM25), c) doping with a mix of tramp elements (CM26) and d) a boron addition (CM27). There is no systematic trend with carbon. The intermediate carbon base alloy (0.15%, CM3) has the highest $\Delta\sigma_y$ in one case (PB) and lowest in the other (T14). A slight increase in $\Delta\sigma_y$ at the higher nitrogen level (CM25) is observed in data from both capsules. The alloy with the boron addition (CM27) has a lower $\Delta\sigma_y$ in both cases. The $\Delta\sigma_y$ of the alloy with tramp element additions is the same as the base alloy in one case (T14) and slightly less in the other (PB). However, all these $\Delta\sigma_y$ are small and the differences between them are even smaller. Thus the effects of these composition variations, with the possible exception of boron, can be considered to be well within the data scatter. Since boron additions both reduce the magnitude and increase the scatter in the unirradiated σ_y, no firm conclusion can be drawn regarding the effect of this element either. Therefore, it is concluded that the effects of these other composition variations are minor and, if they exist at all, will emerge only at higher fluence, where the matrix defect contribution to $\Delta\sigma_y$ is larger.

Table 4-2 summarizes the trends discussed in the previous paragraphs for low copper (~ 0.02%) steels. Again, the magnitudes given are illustrative for 290°C, 0.5-1x10^{23} n/m^2 irradiations (assuming there is no flux effect in this case) of low copper alloys. The effects of heat treatment have not been determined. The specific values again must be viewed as representative.

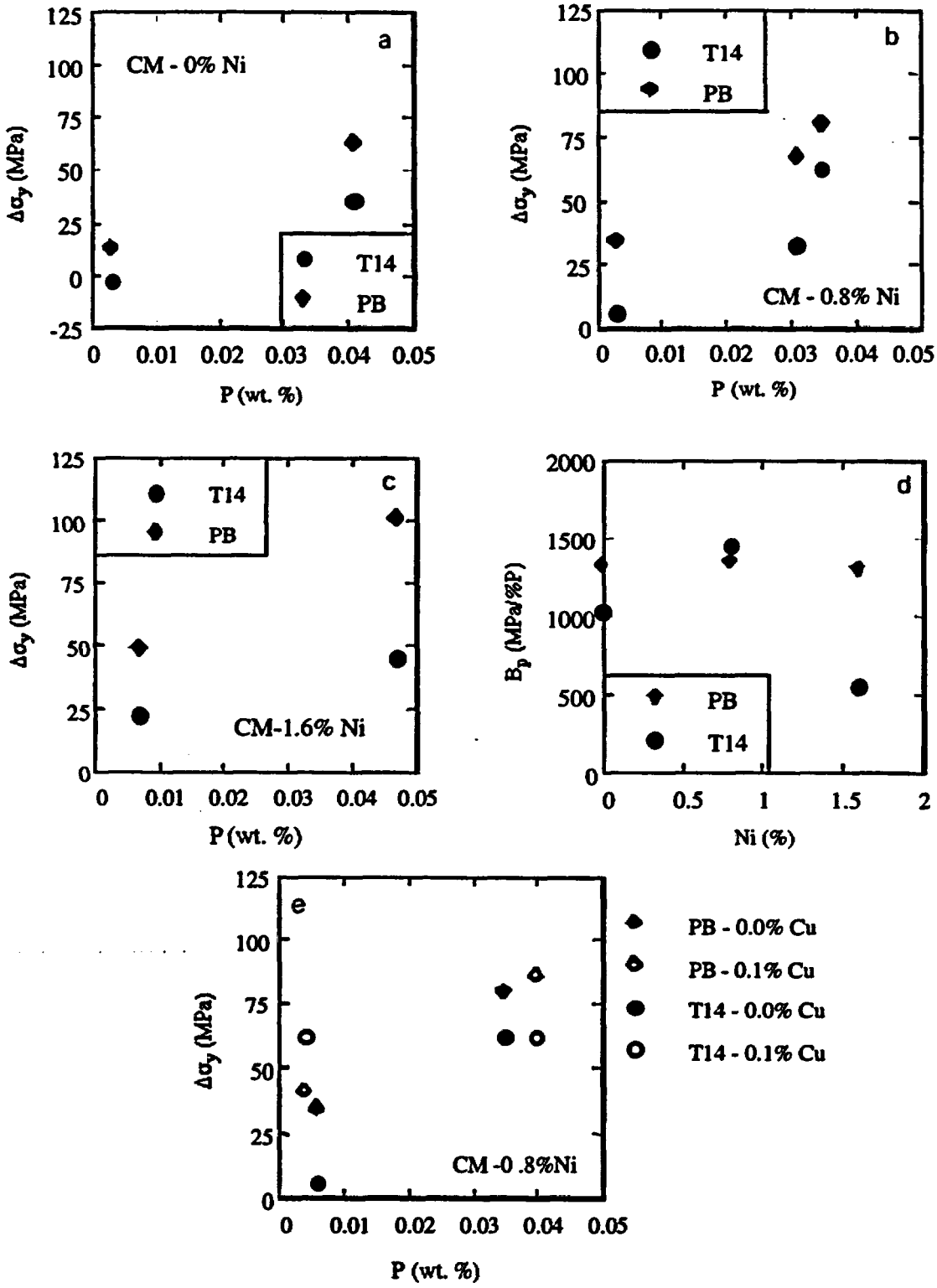

Figure 4-5 Variation of $\Delta\sigma_y$ with P for a) low copper, low nickel; b) low copper, intermediate nickel; and c) low copper, high nickel steels. d) Variation of phosphorous sensitivity (B) with nickel. e) Comparison of $\Delta\sigma_y$ (P) for alloys with 0.02 and 0.11% copper.

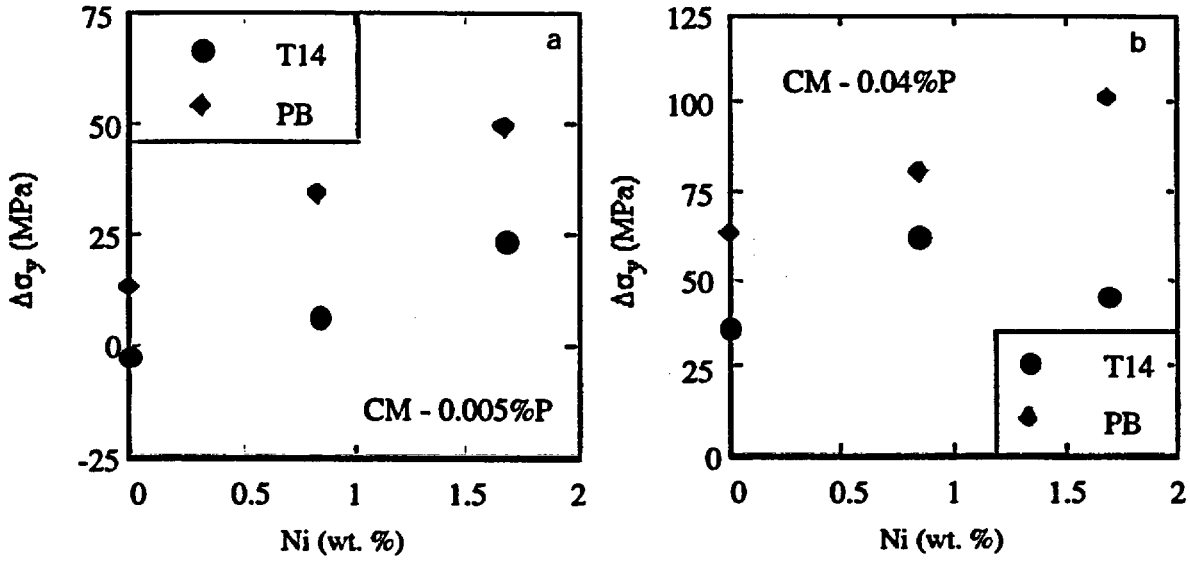

Figure 4-6 Variation of $\Delta\sigma_y$ with nickel for a) low and b) high phosphorous steels.

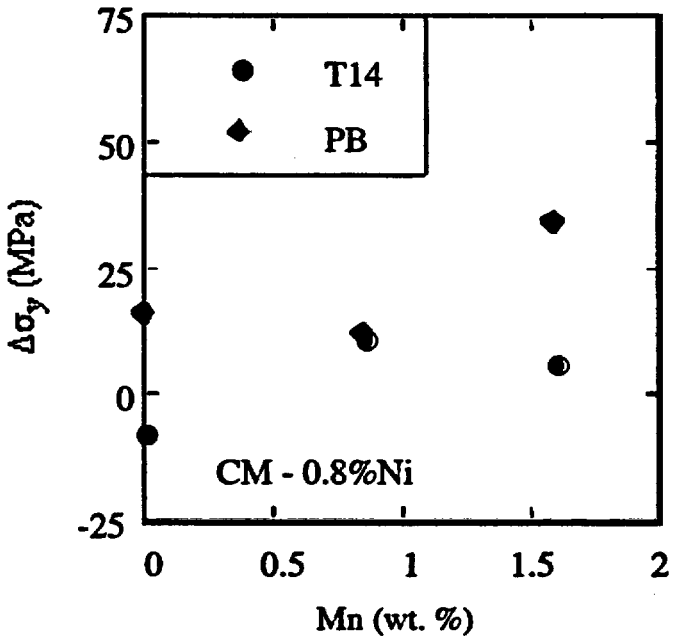

Figure 4-7 Variation of $\Delta\sigma_y$ with manganese for low copper CM alloys.

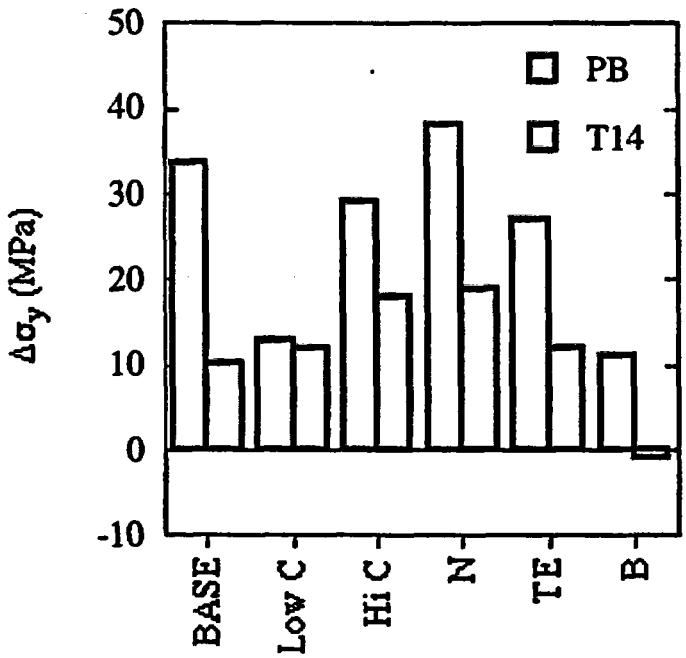

Figure 4-8 Variation of $\Delta\sigma_y$ with carbon, nitrogen, boron and tramp elements (TE) for low copper CM steels.

Table 4-2. Summary of Compositional Dependence of Hardening in Low Copper Steels

Variable	Dependence	Interactions	Magnitude
phosphorus	~ A + BP	possibly copper and HT	B ~ 1200 MPa/%P
nickel	~ A + BNi		B ~ 20 MPa/%Ni
manganese	~ A + BMn		B ~ 10 MPa/%Mn
C, N, B, tramp elements	not established		probably minor

5 ANALYSIS OF THE COMPOSITIONAL TRENDS

5.1 Comparison of the IVAR Results With Predictions of the NUREG/CR-6551 Model

The NUREG/CR-6551 ΔT model (referred to here as the NUREG model) derived from statistical fits of physically motivated embrittlement equations to the PREDB, provides a good basis to analyze and evaluate the data trends described in the previous section. The NUREG-ΔT model was first converted to a corresponding NUREG-$\Delta\sigma_y$ model using an analytical ΔT-$\Delta\sigma_y$ relation. Details are given in Appendix A. Figure 5-1 shows the predicted versus measured $\Delta\sigma_y$ for data from the T14 capsule. The predictions are based on the NUREG-ΔT model parameters for welds. Good agreement is found for all the LV and CM model steels as well as the welds and plates obtained from various sources. The overall bias and standard error between the predicted and measured values are about -1.9 and ±18 MPa, respectively. A least squares fit has a slope of 1.06 and an intercept -6.1 MPa. Thus the mean NUREG-$\Delta\sigma_y$ model predictions are within about 6 MPa of a perfect 1:1 correlation with measured values up to 200 MPa.

Figure 5-2 compares the NUREG-$\Delta\sigma_y$ model predictions of copper dependence of $\Delta\sigma_y$ with the T14 data that has been adjusted to a common nickel (0.8%) and phosphorous (0.005) content. The adjustments are based on the differences predicted by the NUREG-$\Delta\sigma_y$ model for the common versus actual alloy composition. These adjustments are small except in cases where the nickel level is much different than about 0.8%. No correction is made for manganese differences. The CM and LV model steels, with nominal nickel and manganese contents of about 0.8% and about 1.4 to 1.6%, respectively, are shown as the filled circles. The CM and LV steels with higher or lower nickel and manganese are shown as the unfilled circles. The other welds and plates are shown as unfilled diamonds and triangles, respectively. The agreement is generally good. However the $\Delta\sigma_y$ of the intermediate nickel, high manganese CM and LV alloys fall a little higher than the NUREG model predictions in the range of 0.2 to 0.4% copper. As might be expected, the $\Delta\sigma_y$ for the low manganese CM alloys fall below the NUREG model predictions.

Figure 5-3 compares the NUREG model predictions of the effect of nickel on $\Delta\sigma_y$ with LV and CM data from the T14 capsule. Both the magnitude and predicted variation of $\Delta\sigma_y$ with nickel are in good agreement with the high copper (0.42%) data (CM18-20) shown in Figure 5-3a. The agreement is not as good for the intermediate copper (0.22%) CM alloys (CM15-17) where the $\Delta\sigma_y$ are underpredicted at both intermediate (0.85%) and high (1.6%) nickel levels (CM16 and 17).

Figure 5-4 compares the NUREG model predictions of $\Delta\sigma_y$ as a function of fluence to data for low copper (0.02%) intermediate nickel (0.85%) CM alloys (CM3,5) for low and high phosphorous levels. In this case $\Delta\sigma_y$ data from lower fluence[2] capsules have been added to T4, T14 and PB results. The data are scattered around the NUREG predictions, but overall agreement is good. Thus, the IVAR $\Delta\sigma_y$ data suggests that the effect of phosphorous is well represented by the NUREG model.

Given various sources of uncertainties in the data and application the $\Delta\sigma_y$ modification of the NUREG ΔT correlation model statistically fit to the completely independent surveillance PREDB, the overall agreement is remarkable. Thus the $\Delta\sigma_y$ database generated in this study provide a powerful and independent confirmation of the general form of the NUREG model.

[2] These capsules are designated T1, T2, T11-T13, and T21

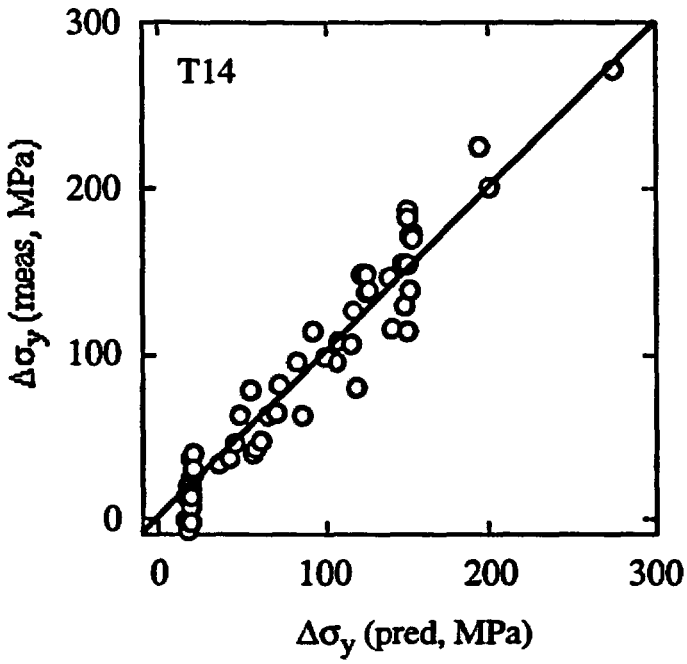

Figure 5-1 Comparison of the NUREG- $\Delta\sigma_y$ model predictions with the data from the capsule T14.

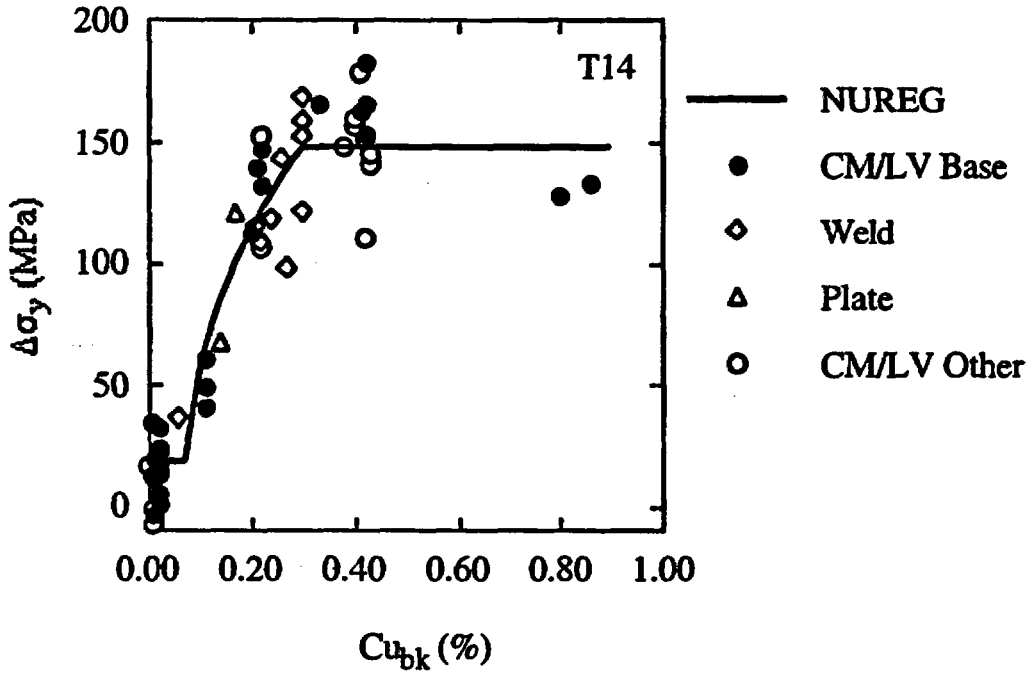

Figure 5-2 Comparison of the NUREG- $\Delta\sigma_y$ model predictions with the data from capsule T14 adjusted to 0.8 nickel and 0.005% phosphorous.

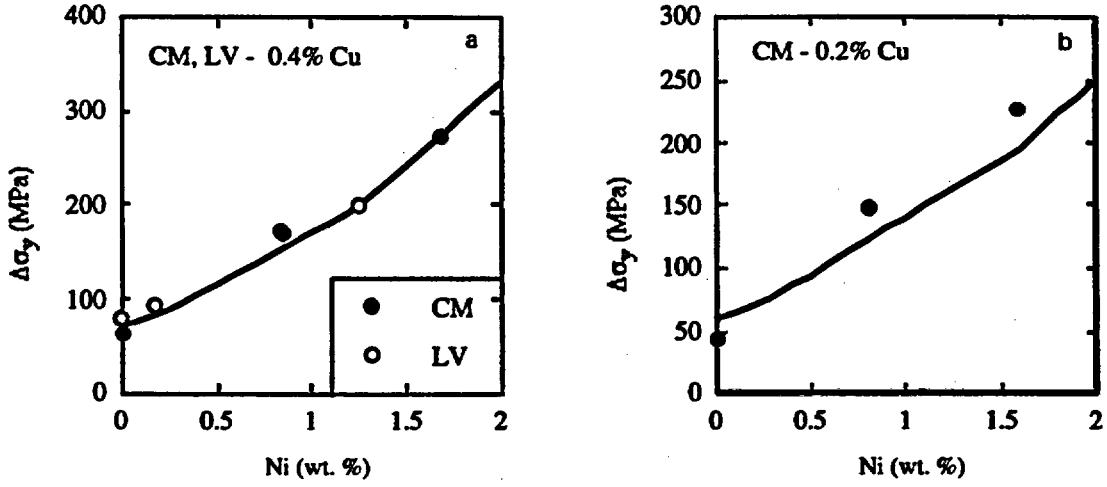

Figure 5-3 Comparison of the NUREG-$\Delta\sigma_y$ model predictions of nickel dependence of embrittlement with the T14 data for a) 0.4% copper and b) 0.2% copper steels.

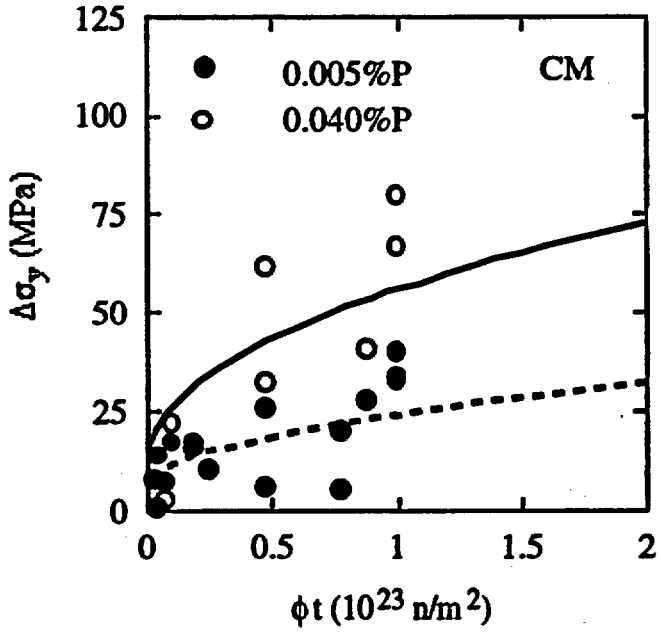

Figure 5-4 Comparison of NUREG-$\Delta\sigma_y$ model predictions with $\Delta\sigma_y$ data as a function of fluence for low copper (0.02%) intermediate nickel (0.85%) CM alloys for both low (0.005%, CM3) and high (0.04%, CM5) phosphorous levels.

5.2 The Microstructural Basis, Mechanisms and Models for the Composition Dependence of Hardening and Embrittlement

The primary cause of ΔT is irradiation hardening, $\Delta\sigma_y$ [Odette et al, 1985; Fisher and Buswell, 1987]. Hardening is in turn caused by the irradiation induced formation of a large population of nanoscale features that act as obstacles to dislocation slip.[Odette, 1983; Odette and Lucas, 1998; Fisher and Buswell, 1987]. The irradiation-induced nanofeatures are significantly weaker than strong, pre-existing obstacles to dislocation slip, such as fine scale Mo_2C carbides, that are largely unaltered by irradiation. The latter require dislocations to bow around them, while dislocations can penetrate the irradiation nanofeatures. The individual strength contribution of the nanofeatures (σ_i) is a function of their specific character, size [r_i], number density (N_i) and volume fraction (f_i) as [Odette and Lucas, 1998]

$$\sigma_i \sim \Lambda_i(r_i)\sqrt{f_i} \qquad (5\text{-}1)$$

where the $f_i = [4\pi r_i^3/3]N_i$, and the Λ_i describes the strength of the feature that depends on r_i. Peak strength occurs at roughly $r_{ip} = 1$ to 1.5 nm. The $\Lambda_i(r_i)$ decreases rapidly below this peak hardening size (r_{ip}), and roughly proportionately to $(r_{ip}/r_i)^n$, where $n < 1$ at larger sizes. As discussed elsewhere in this report, the net $\Delta\sigma_y$ is less since, σ_i must combine with the contribution of pre-existing strong obstacles (σ_o) [Odette and Lucas, 1998].

Current understanding of the embrittlement nanofeatures is based on combinations of sophisticated microstructural and microchemical characterization studies and physical models. Characterization methods include: small angle neutron and x-ray scattering that provide size, volume fraction and compositional information [Odette, 1995; Odette and Lucas, 1998; Phythian and English, 1993; Solt et al, 1990, 1993; Mader, 1995; Williams and Phythian, 1996; Wirth, 1998; Wirth et. al, 1999; Alexander et. al, 1999], various types of electron microscopy that provide both high resolution structural images and compositional information [Phythian and English, 1993; Jenkins 1994; Williams and Phythian, 1996] and 3-dimensional atom probe-field ion microscopy that measures the configuration of the elements within a small sampling volume to near atomic resolution [Miller et al, 1993; Miller et al, 2000]. Thermo-dynamic-kinetic models are used to track the transport and fate of irradiation defects and solutes and to predict the number, size distribution and composition of the nanofeatures [Odette and Wirth, 1997; Odette and Lucas, 1998; Odette 1998; Wirth, 1998]. For pressure vessel and surveillance conditions and the irradiations in this study, the nanofeatures can be divided into two broad categories [Odette and Wirth, 1997; Odette and Lucas, 1998; Odette, 1998; Fisher and Buswell, 1987; Mader, 1995; Wirth 1998; Liu et al, 1997]:

- copper-rich or catalyzed Mn-Ni rich precipitates (CRPs/MNPs)

- matrix features primarily in steels with low or no copper The matrix features are defect (vacancies and possibly interstitials)-solute cluster complexes that are probably formed directly in displacement cascades. Other precipitate phases, such as phosphides, may also contribute to matrix feature hardening.

5.2.1 Copper Rich Precipitates

Following typical heat treatments, copper can remain dissolved in the in the iron matrix up to about 0.3% [Odette, 1995; Odette and Lucas, 1986, 1988, 1997, 1998; Buswell and Jones, 1993; Williams and Phythian, 1996; McElroy and Lowe, 1996; English et al, 1997]. However, the solubility of copper decreases at lower temperatures, to <0.01% at around 290°C. The supersaturated copper diffuses and precipitates into a separate phase. Enhanced diffusion, caused by excess vacancies produced by irradiation, enormously accelerates processes that are normally thermally sluggish, resulting in the rapid formation of a high number ($\geq 10^{23}$ m^{-3}) of small (~1.5-3 nm diameter) CRPs with a

BCC crystal structure that is coherent with the iron matrix.

The CRPs are the dominant hardening feature in sensitive steels that have copper contents greater than about 0.05-0.1%, which is the minimum needed for rapid nucleation. The CRP volume increases with copper up to an effective upper limit around 0.3%, imposed by copper pre-precipitation at the final stress relief temperature (typically about 610°C). The CRP contribution has a relatively weak irradiation temperature dependence and saturates at high fluence, due to copper depletion from the matrix. The CRP evolution is delayed at higher fluxes by interstitial recombination with vacancies that are trapped at solutes and in small transient clusters [Odette et al., 1993; Odette and Lucas, 1998; Odette, 1998]. The amount of recombination increases with increasing flux. At very low flux, CRP evolutions may be accelerated due to a contribution of thermal diffusion to copper precipitation [Odette et al, 1999].

The precipitates are not pure copper, but are enriched in manganese and nickel as well as smaller amounts of phosphorous and silicon [Mader, 1995; Liu et al, 1997; Odette and Lucas, 1998; Odette, 1998; Wirth, 1998; Wirth and Odette, 1997]. The thermodynamics of the copper-manganese system is such that at low temperatures around 290°C manganese partitions from the matrix and is enriched in copper precipitates. Nickel itself does not interact as strongly as manganese. However, if nickel and manganese are both present, they interact strongly with each other, and synergistically increase the concentration of both elements in the precipitates. In some cases this can result in the replacement of CRPs with manganese-nickel rich precipitates (MNPs) with a small copper rich core [Wirth and Odette, 1999; Liu et al, 1997]. Manganese-nickel enrichment of the precipitates is promoted by higher alloy contents of these elements, lower copper (beyond the amount needed for nucleation) and low irradiation temperature. The increase in the volume fraction of CRPs (or MNPs) with manganese and nickel explains the strong effect of these elements on increasing $\Delta\sigma_y$ and ΔT.

Typical values for the A_i for CRPs at peak strengthening size are about 3750 MPa. Thus, a $f_{crp} = 3x10^{-3}$ produces a $\sigma_{crp} \sim 240$ MPa. Taking $\sigma_s = 200$ MPa and a superposition parameter of $\theta = 0.4$ (see Equation 6-4 below) typical of CRPs, gives a net $\Delta\sigma_y \sim 135$ MPa.

Figure 5-5 plots the estimated volume fraction of CRPs from SANS measurements on CM and LV alloys from the PB capsule as a function of the alloy nickel and manganese contents. The corresponding estimated precipitate volume fractions of copper, nickel, manganese and vacancies (lumped together for clarity) are also shown. The composition evaluations are consistent with the magnetic to nuclear scattering ratios measured in the SANS studies. Thermodynamic model predictions of the CRP (MNP) composition are used to guide this assessment [Wirth, 1998]. The thermodynamic model generally predicts higher nickel and manganese levels in the precipitates than is consistent with the experimental scattering ratio. Thus the amounts and relative proportion of these elements are minimally adjusted to provide consistency. The resulting estimates of the composition of the precipitates are not unique and are subject to considerable uncertainty. However, these estimates are reasonable and certainly provide insight into the general trends. Further details are given elsewhere [Wirth, 1998; Wirth et al, 1999].

Figure 5-5a shows differences in the precipitate parameters as a function of nickel from 0.02 to 1.69% for the CM alloys (CM18, 19, 20). The f_{crp} increases linearly with nickel. Higher alloy nickel levels increases the CRP manganese and nickel contents, with a big jump between 0.84 and 1.69%. Indeed, at highest nickel the precipitates are actually manganese-nickel rich (MNP). Figure 5-5b shows similar but more modest increases that are observed for the LV alloys with 0.85 to 1.25% nickel (LC, LD). Similar effects of increases in the CM alloy manganese content from 0 to 1.6% (CM21, 19,

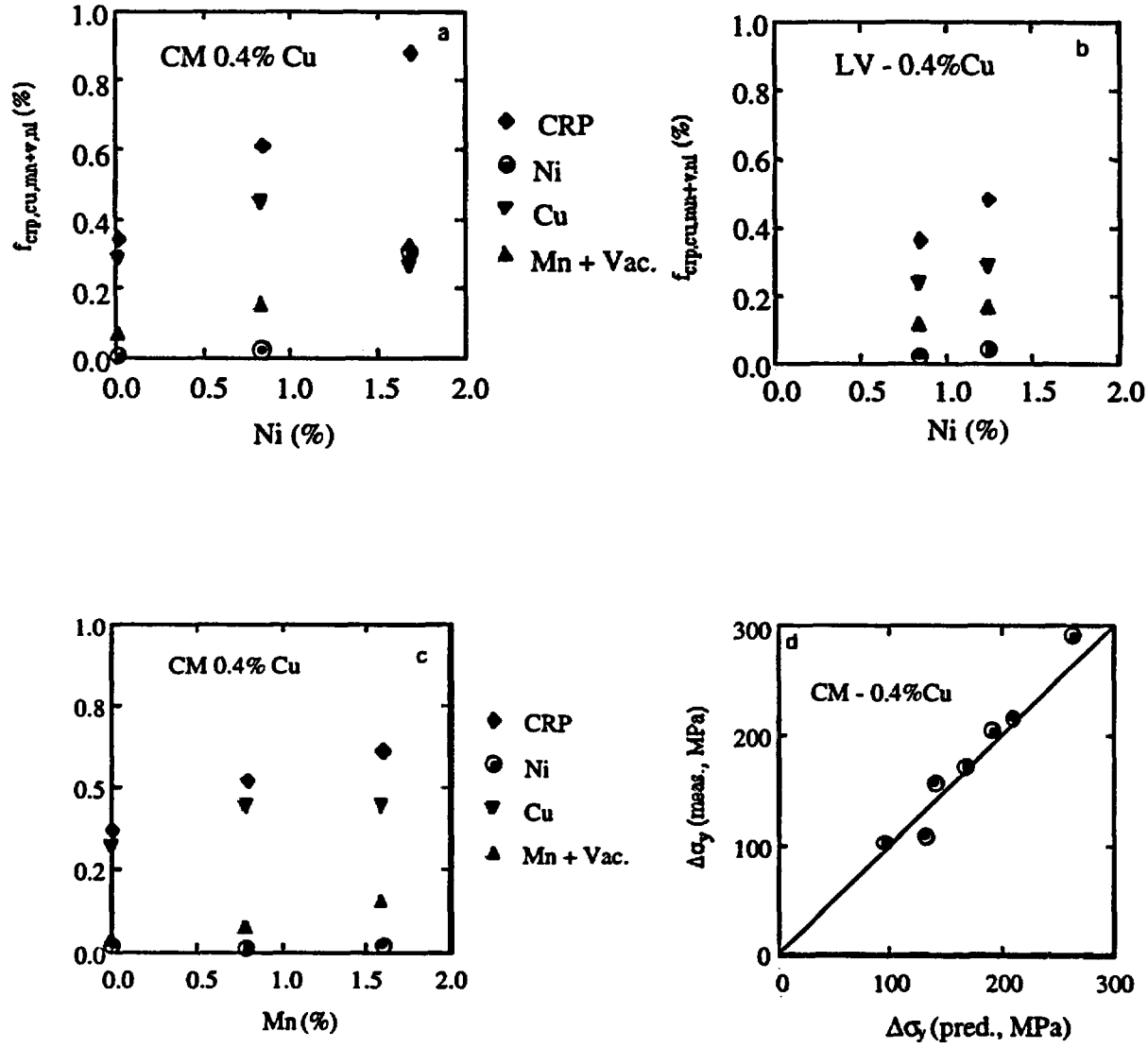

Figure 5-5 Volume fraction of CRP's estimated from SANS measurements on CM and LV alloys for the PB capsule as a function of a) nickel for CM alloys, b) nickel for LV alloys, and c) manganese for CM alloys; d) comparison of measured $\Delta\sigma_y$ with values predicted from SANS microstructural parameters.

22) are shown in Figure 5-5c. Higher nickel and manganese alloy contents also increase N_{crp} [Wirth, 1998]. In this study, the increase in N_{crp} is more than a factor of 7 between 0 and 1.69% nickel, with a corresponding reduction in r_{crp} from ~ 2 to 1.4 nm. Figure 5-5d compares the $\Delta\sigma_y$ predicted by a hardening model based on the SANS measurements of f_{crp} and r_{crp}, to experimental values. Details of the procedure are described elsewhere [Wirth, 1998; Wirth et. al, 1999]. The agreement is good, demonstrating that the effects of manganese and nickel on the CRP contribution to hardening and embrittlement, as summarized in Table 4.1, can be understood on the basis of the corresponding effects of these elements on the f_{crp} and r_{crp}.

5.2.2 Matrix Features

The matrix features are generally not as well understood as CRPs. Atom probe studies have shown regions enriched in solutes like manganese, nickel and silicon [Pariege, 1994; Miller et. al, 2000]. These features are probably formed directly in cascades, where the solutes are complexed with defect clusters [Wirth, 1998; Wirth and Odette, 1999]. Vacancy cluster solute complexes are the most likely candidate, although small interstitial cluster-solute complexes are also a possibility. Even if the defect clusters dissolve, or migrate to sinks, the solute enriched regions are left in their wake. The atom probe studies suggest that about $2.5x10^{17}$ matrix features form per 10^{23} n/m^2 (roughly 1 for every 10 cascades). Assuming an effective r_{mf} ~ 0.7 nm and f_{mf} ~ $5x10^{-4}$ per 10^{23} n/m^2, as suggested by SANS studies [Wirth, 1998] (although the size of the actual enriched region may be larger) results in an estimate of A_{mf} ~ 1350 MPa. Since the matrix features are significantly weaker than CRPs, it is generally assumed that their entire σ_{mf} contributes (adds) to $\Delta\sigma_y$. Thus the matrix features are expected to produce about 30 MPa hardening at 10^{23} n/m^2. Since the number of matrix features increases in rough proportion to fluence (ϕt), at a roughly constant size, their contribution to $\Delta\sigma_y$ is predicted to increase with $\sqrt{\phi t}$. Note that given their typical concentration and composition, depletion of matrix manganese and nickel does not lead to a saturation of the matrix features in the fluence range of interest. However, a slow decrease in the fluence exponent in the NUREG model can be understood based on depletion and overlap effects, as well as some thermal recovery of the strengthening contributions of the matrix features over long periods of time.

At low concentrations phosphorous may also segregate to the matrix feature complexes. However, phosphorous has a very low equilibrium solubility in steels that can form alloy phosphides like Mo_3P, which are much more stable than the Fe_3P phase in binary alloys [Odette, 1998]. Thus alloy phosphides are expected to form and contribute to $\Delta\sigma_y$. Fine scale features containing phosphorous, nitrogen and carbon have been observed in atom probe studies [Pareige, 1994, Miller 2000]. Phosphorous also interacts strongly with copper, and segregates to CRPs. Phosphorous gettered by CRPs is not available to form phosphides. This rationalizes an interaction that reduces the effect of phosphorous at higher copper levels. A phosphorous-copper interaction of this sort can also be produced by the strength superposition mechanism noted previously. That is the individual strength contribution of phosphides to the net $\Delta\sigma_y$ is reduced in the presence of CRPs.

As noted above both SANS and atom probe studies have detected matrix features, either directly (atom probe) or through scattering responses (SANS), that indicates a role of manganese, nickel and phosphorous. Further, atom probe studies of samples from the decommissioned CHOOZ reactor vessel have beautifully quantified the number and general dilute solute enrichment characteristics of matrix features over a wide range of fluence [Pariege, 1994, Auger et al, 1994]. While efforts to better quantify the matrix features are continuing, these observations, and others [Wirth and Odette, 1999], clearly rationalize

the $\Delta\sigma_y$ trends with these elements as summarized in Table 4-2. That is, higher alloy nickel, manganese and phosphorous contents increase some combination of the solute content, volume fraction and strength of the matrix features, leading to increased $\Delta\sigma_y$. It should be noted that the role of phosphorous is somewhat special, since well-formed phosphide precipitates may be responsible for the hardening caused by this element. Further, depletion of matrix phosphorous would be expected to lead to an eventual saturation of the phosphide matrix feature contribution. However, the evolution of the phosphides appears to be much slower than characteristic of CRPs, consistent with their narrow range of chemistry and the low phosphorous concentration. Thus for practical purposes, it is a reasonable engineering expedient to lump them with the other matrix features.

More detailed discussions of the experimental and modeling that underpins the preceding discussion can be found elsewhere [Odette and Lucas, 1998, 1999; Odette, 1998; Eason et al, 1998] and will be elaborated on in future reports. For the present purposes, however, it is sufficient to conclude this section by noting that all the major trends in both the NUREG model and observed in the IVAR database are consistent with current understanding of embrittlement mechanisms. However, a number of open questions and unresolved issues remain, providing further opportunities for improvements in the NUREG embrittlement correlation models. These are briefly described in the following section.

5.3 Discussion of Improvements in the NUREG Embrittlement Correlation Model Treatment of Composition Effects

It must be stated at the outset that it is not possible to separate compositional effects on embrittlement from other metallurgical variables, such as product form and heat treatment, and irradiation variables, including flux, fluence and temperature. Some of the effects of heat treatment are presented in the following section. Thus, a comprehensive reassessment of the NUREG models and progeny correlation models will be based on the on the entire IVAR database in the future. Nevertheless, the information presented in this report provides some insight into what such improvements may entail.

First, the overall treatment of copper-nickel interactions in the NUREG model seems fairly robust. However, IVAR data indicate that manganese is also a key element in the CRP contribution to embrittlement. This may at least partly explain why the forging CRP coefficient (70°C) is lower by about 22% compared to that of plates (95°C). Assuming typical copper, nickel, and phosphorous contents of 0.15%, 0.6% and 0.01%, respectively, and an irradiation fluence of $5x10^{22}$ n/m^2 at 288°C, the NUREG plate model predicts a $\Delta\sigma_y$ of about 70 MPa. However, forgings have about half the manganese content (~ 0.7%) as plates (~1.4%). Based on coefficients in Table 4-1 this translates to a reduction in $\Delta\sigma_y$ by about 20 MPa, or a 29% reduction.

There are even larger differences between the NUREG CRP coefficients for forgings and welds; and manganese differences do not explain differences between the NUREG plate and weld CRP coefficients. However, the IVAR $\Delta\sigma_y$ data for the CM/LV steels and the welds and forgings do not indicate such large differences. Other factors that may influence the apparent product form sensitivity include the variations in both the average and range of copper content in the PREDB, which are significantly higher for welds. Effects that are not accounted for in the NUREG model, such as an influence of copper and nickel on the fluence dependence of $\Delta\sigma_y$ and the effects of start-of-life Charpy properties on the $\Delta\sigma_y/\Delta T$ relation, may also play a role in apparent product form sensitivity. Further, a number of other variables are known to influence both CRP microstructures and $\Delta\sigma_y$ at an otherwise

specified set of conditions. These variables include: a) a range of heat treatment effects (see below); b) phosphorous and silicon, which are enriched in CRPs and increase their number densities; and c) coarser scale dislocation sink microstructures which influence the radiation enhanced diffusion rate — hence, the fluence dependence — of the CRP contribution [Odette and Lucas, 1998; Odette, 1998]. Finally, the current IVAR database shows that flux and composition interact to influence CRP contributions to $\Delta\sigma_y$. Data on such interactions will be extended to irradiation temperature in the future.

In summary, the part of the IVAR database presented here provides a partial basis to narrow differences in the CRP contribution now empirically attributed to a product form arising from mechanisms that are not understood. More importantly, these results lead to the anticipation that, in the future, such differences can be further reduced and explicitly modeled to reflect the responsible variables.

Similar arguments pertain to the matrix feature contributions to $\Delta\sigma_y$. Clearly some of the product form variability in the NUREG model can be attributed to variables that are not explicitly treated. Manganese and nickel enhance hardening but are not accounted for in the matrix feature contribution in the NUREG model. Figure 5-6 plots the low copper LV and CM $\Delta\sigma_y$ data (LG, CM1to10) from the T14 and PB capsules versus a matrix feature solute chemistry factor (CF_{mf}) simply defined by scaling the results as shown in Table 4-1 by dividing by 10, where

$$CF_{mf} = 120P + 2Ni + 1Mn \qquad (5\text{-}2)$$

The PB data correlate very well with CF_{mf} (filled circles) while the T14 data (open circles) follow a similar trend, but are more scattered. In both cases the least squares fit to the $\Delta\sigma_y(CF_{mf})$ have a negative value at the $CF_{mf} = 0$ intercept, suggesting that there is a threshold solute concentration for hardening in low copper steels. However, it is not clear that this is actually the case, as illustrated by VM-series data from the PB capsule shown as the open diamonds at $CF_{mf} = 0$. These VM alloys do not contain manganese and nickel but do include small concentrations of nitrogen and in one case a 0.25% titanium addition.

The $\Delta\sigma_y$ data from the PB capsules for other simple VM-series alloys shown in Figure 5-7 also illustrate the role of solutes and solute interactions on matrix hardening. The unalloyed iron (VA) with low (10 ppm) nitrogen has a $\Delta\sigma_y$ of 42 MPa. Increasing the nitrogen to 100 in unalloyed iron (VK, VV, VW) has little effect on hardening with an average $\Delta\sigma_y$ of 36 MPa. However, the $\Delta\sigma_y$ for the VB alloy with 40 ppm nitrogen and 1% manganese increases to 102 MPa. The VR alloy with 120 ppm nitrogen and 1% manganese has an even larger $\Delta\sigma_y$ of 152 MPa, suggesting a strong interaction between these elements. In contrast the VC alloy with 0.15% carbon, 30 ppm nitrogen and 1% manganese has an intermediate $\Delta\sigma_y$ of 70 MPa. Most of this reduction (~ 24 MPa) can be attributed to the precipitation of manganese in $Fe(0.2Mn)_3C$ phases, and a lesser amount (~ 8 MPa) is estimated be due to the lower nitrogen in this steel (VC) compared to the 1% Mn alloy without carbon (VB). Without nitrogen present the effect of manganese is estimated to be small ($\leq$10 MPa/%Mn), but similar to that found for RPV steels in Table 4-2. The VB alloy with 40 ppm nitrogen and 1% manganese showed a strong SANS signal similar to scattering from matrix features in complex steels [Wirth, 1998]: a radius of about 0.76 nm, a volume fraction of 0.052%, and a low magnetic-to-nuclear scattering ratio (0.57). This scattering ratio is characteristic of manganese-vacancy clusters.

Such subtle interactive effects rationalize the very large relative scatter in matrix features, $\Delta\sigma_y$ and ΔT that are observed in low copper steels. The scatter in ΔT is illustrated in Figure 5-8a, comparing the NUREG matrix feature

predictions with the data from the French power reactor surveillance program [Brillaud and Hedin, 1992]. Figure 5-8b shows the large scatter also observed in $\Delta\sigma_y$ in the low copper steels irradiated in the IVAR capsules, including an apparent difference between the LV and CM alloys of unknown origin. The significance of this scatter has been discussed elsewhere [Odette and Lucas, 1999]. Briefly, it is not of much practical significance in low copper steels which experience only small to modest ΔT. However, since the matrix features add to the CRP contribution, presumably along with its attendant scatter, this variability may be much more serious in sensitive high copper and high nickel steels. This is of particular concern at high fluence, where the matrix feature contribution becomes more significant. Indeed, based on these considerations it has been shown that ΔT in excess of upper bound estimates from the NUREG model based estimates might be anticipated in some cases [Odette and Lucas, 1999]. However, this potential non-conservatism may be mitigated by the simplified treatment of phosphorous in the NUREG model. In particular both synergistic interactions with copper and phosphorous depletion at high fluence would reduce actual ΔT compared to the NUREG model predictions. Additional data generated in the IVAR program will help to resolve these issues.

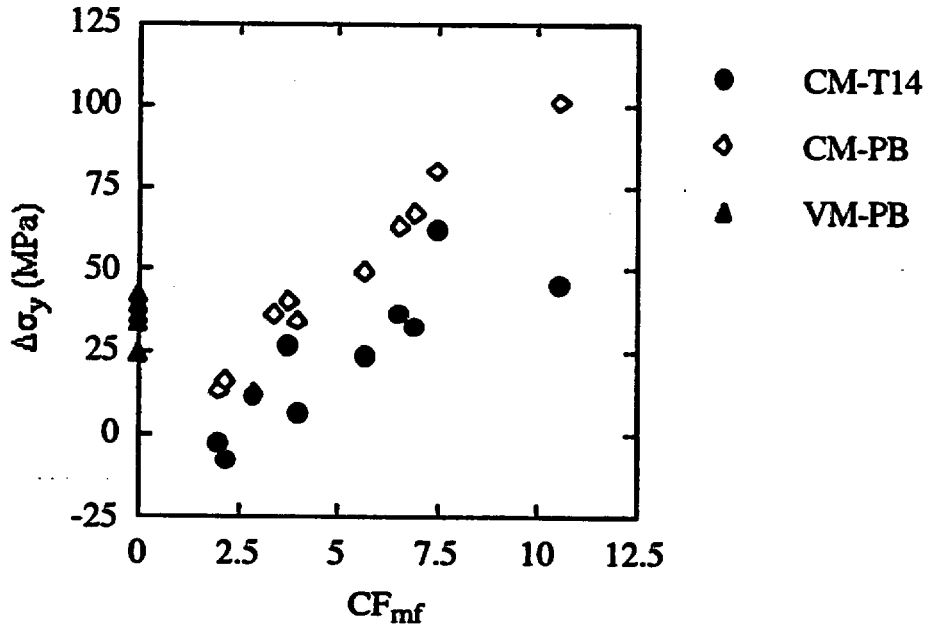

Figure 5-6 Variation of $\Delta\sigma_y$ with a matrix feature chemistry factor given in Equation 5-2 for low copper CM and LV steels for capsules T14 and PB. The unalloyed VM steels are shown as filled triangles.

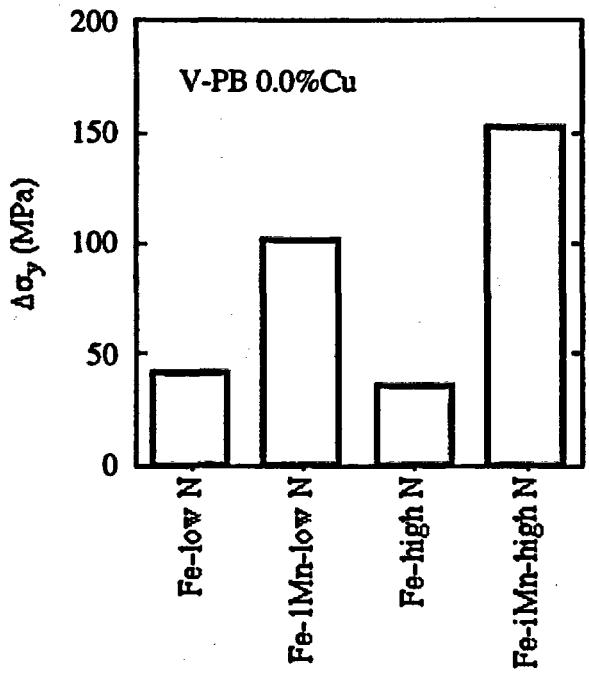

Figure 5-7 $\Delta\sigma_y$ for various V-series alloys with no copper irradiated in PB.

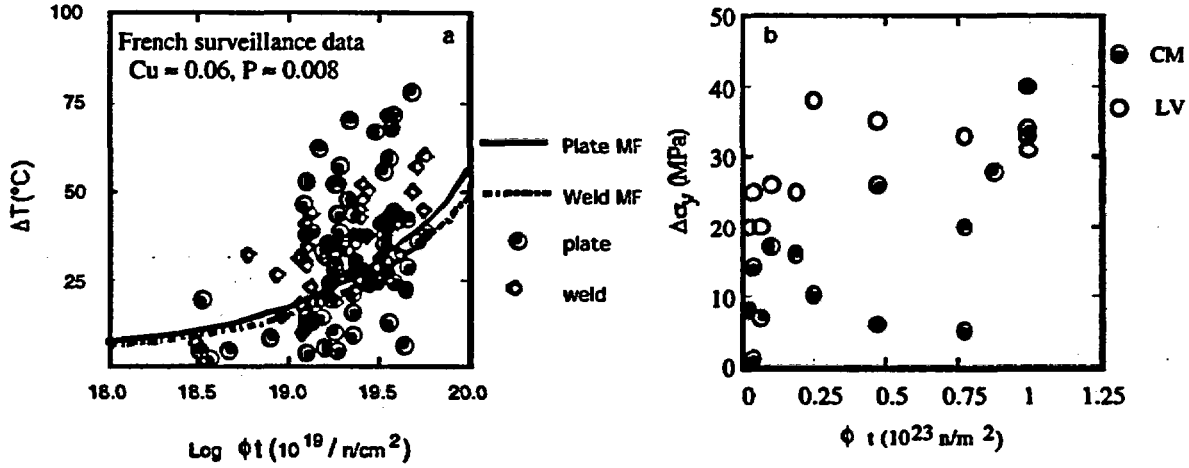

Figure 5-8 a) Comparison of NUREG matrix feature predictions with low copper French power reactor surveillance data; b) plot showing scatter in $\Delta\sigma_y$ in low copper steel irradiations in this study and unexplained differences between CM and LV alloys.

6 EVALUATION OF THE MATRIX COPPER CONTENT

A key issue in developing embrittlement models is determining the amount of copper in solution, thus available for precipitation under irradiation. Bulk copper (Cu_{bk}) that is tied up in coarse precipitates, or other phases (e.g., copper sulfide inclusions [Fisher et. al, 1985; Fisher and Buswell, 1987]), at the start-of-life does not contribute to subsequent hardening and embrittlement. The difference between Cu_{bk} (in wt%) and effective dissolved, or matrix, copper content (Cu_m) is determined by both the alloy composition and heat treatment history. Pre-precipitation of large ε-phase copper particles, primarily on dislocations, during tempering and stress relief (SR), is a primary mechanism controlling Cu_m below bulk levels. The Cu_m approaches thermodynamic solubility limits after long times at around 600°C. However, thermal precipitation is a complex process. As well as time-temperature kinetics, alloy chemistry (thermodynamics) and microstructure likely influence pre-precipitation behavior. In NUREG/CR-6551 a statistical fit to the overall PREDB gave the maximum Cu_m (Cu_{max}) of 0.3%. This result is broadly consistent with data trends and various estimates in the literature, although both higher and lower values have been reported [Odette, 1995; Odette and Lucas, 1986, 1988, 1997; Buswell et al, 1993, Williams and Phythian, 1996; McElroy and Lowe, 1996; Williams and Phythian, 1996; Kenway-Jackson et. al, 1993; English et al, 1997]. Indeed, both information in the literature, and more recent analysis of the PREDB, have suggested that the actual value varies, depending on the alloy nickel content [McElroy and Lowe, 1996; Odette and Lucas, 1990, 1998; Williams and Phythian, 1996].

Accurate direct estimates of Cu_m require detailed and costly measurements that push, or even exceed, the capabilities of state-of-the-art modern microanalytical characterization methods. While some of these studies have been carried out, much more work will be required to provide a useful microanalytical database necessary to develop models for Cu_m. However, mechanical property changes are the issue of prime concern and can provide *indirect* estimates of matrix copper. Thus, the variable stress relief (VSR) study was primarily intended to conveniently assess the effects of the heat treatment and nickel content on Cu_m by simply assessing the corresponding effects on $\Delta\sigma_y$. While this objective was largely achieved, the results of the VSR study also showed that heat treatment effects extend well beyond matrix copper levels, and influence both the start–of-life properties and microstructures of RPV steels. The start–of-life condition, in turn, affects the irradiation-induced changes in mechanical properties.

The use of a large set of small split-melt model steels with a wide range of compositions and heat treatments in the VSR study resulted in confounding effects that complicated assessment of Cu_m in a fraction of cases. The complications included large σ_y variations and variability (scatter) for some heat treatments. These σ_y variations also reflect underlying microstructural differences. These problems were exacerbated by the effects of banding and ghost lines found in a number of the CM forgings, coupled with the use of a slow cooling schedule of about 8°C/h. The as-tempered alloys and the CM alloys that were furnace cooled following stress relief were more stable and less variable.

Thus for purposes of assessing the matrix copper, the VSR $\Delta\sigma_y$ data were carefully screened to avoid or minimize the confounding effects noted above. The screened VSR data were used to assess the Cu_m based on the NUREG model. The NUREG-ΔT model was first converted to corresponding $\Delta\sigma_y$ predictions using analytical ΔT-$\Delta\sigma_y$ relations (see Appendix A). The NUREG-$\Delta\sigma_y$ model was then used to calculate values of Cu_m for the VSR data set as well as alloys subject to different heat treatments in the PB experiment, consistent with the measured $\Delta\sigma_y$ for the specific alloy and irradiation condition (phosphorous, nickel content, flux, fluence and temperature). Other

modifications of the NUREG-$\Delta\sigma_y$ model to account for flux-composition and product form effects are discussed below.

A second approach to estimating Cu_m from the $\Delta\sigma_y$ data was based on examining deviations from the NUREG model form

$$\Delta\sigma_y = A + B\chi \qquad (6\text{-}1)$$

where χ is the NUREG copper factor, $\chi = 0$ for $Cu_m \leq 0.072\%$ and $\chi = (Cu_m\text{-}0.072)^{0.678}$ for $Cu_m > 0.072\%$. In this case, no assumptions were made about A and B, or their dependence on embrittlement variables. The A and B were found by fitting the $\Delta\sigma_y$ data from sets of alloys with different copper levels, but nominally similar compositions and heat treatment. Minor corrections were made for nickel differences in the LV alloys (LG, LH at 0.74% vs. LI with 0.85%). The fits to Equation 6-1 were restricted to alloys with copper levels below the maximum precipitation limit ($\leq 0.22\%$ for the standard stress relief condition and $\leq 0.33\%$ for the as-tempered condition). The A and B fits were then used with the measured $\Delta\sigma_y$ for higher copper steels (not used in the fitting) to calculate Cu_m as,

$$Cu_m = [(\Delta\sigma_y - A)/B]^{1.475} + 0.072 \qquad (6\text{-}2)$$

The second method was applied to $\Delta\sigma_y$ from the T4, T14 and PB capsules as well as some averaged data from the VSR study.

The $\Delta\sigma_y$-based estimates of Cu_m were complemented by several other sources of microanalytical information including field emission scanning transmission electron microscopy (FEGSTEM), Seebeck coefficient, electrical resistivity and small angle neutron scattering (SANS) measurements. The FEGSTEM provides direct evaluation of the Cu_m subject to uncertainties and assumptions used in the analysis. The Seebeck coefficient (S) and electrical resistivity (ρ) evalutions were also based on deviations from low copper linear trends in S and ρ plotted against Cu_{bk}, indicating pre-precipitation. The limited SANS data provided direct evidence of the effect of stress relief on the volume fraction of CRP's from the PB experiment.

6.1 General Effects of Heat Treatment on σ_y and $\Delta\sigma_y$

To provide a proper framework for assessing Cu_m, it is necessary to begin with a description of the general effects of heat treatment on σ_y as well as possible effects of σ_y on $\Delta\sigma_y$. This provides a basis to identify the subsets of data that can be used most reliably to estimate Cu_m. As is a general characteristic of quenched and tempered low alloy steels, the σ_y in RPV steels decreases with increasing stress relief time (t_{sr}) and temperature (T_{sr}). This trend is shown in Figure 6-1 where the σ_y data from the VSR study are plotted as a function of a temperature compensated time parameter P_{Ti} defined as

$$P_{Ti} = \Sigma_i \exp(-260{,}000/RT_{sr}(i))t_{sr}(i) \qquad (6\text{-}3)$$

Here T_{sr} is in °K, t_{sr} is in h and i represents T_{hr}-t_{hr} increments of 8°C-1h at the various stages of the heat treatment, including the 660°C-4h temper, the actual isothermal t_{sr}-T_{sr} stress relief and subsequent slow cooling that was truncated at 450°C. For most stress relief conditions, the σ_y is well behaved; but substantial softening generally occurs at high P_{Ti}. However, in some cases a large decrease in σ_y is observed indicating instability in the alloy microstructure. Such instability is indicated by the data below the horizontal lines in Figures 6-1a to 6-1c. The reasons for such large reductions in σ_y are not known.

Thus the following question must be addressed. Does the lower σ_y affect $\Delta\sigma_y$ due to mechanisms that are not related to copper pre-precipitation and Cu_m? Figure 6-2a illustrates the general trend to lower $\Delta\sigma_y$ with increasing σ_y for the set of high copper (~ 0.42%) CM alloys with varying nickel content. The effect is minimal for the low nickel (0.0%) CM18 alloy and only apparent for the lowest σ_y data in the case of the intermediate nickel (0.85%) CM19 alloy. However, the trend appears to be more systematic for the high nickel (1.69%) CM20

alloy. Since all these alloys contain more than 0.4% copper, pre-precipitation probably contributes to the σ_y-$\Delta\sigma_y$ trend in this case. Figure 6-2b shows similar plots for intermediate nickel (~0.85%) alloys with 0.22% (CM16) and 0.33% (CM11) copper levels. Both alloys show a trend of lower $\Delta\sigma_y$ with increasing σ_y, at least for the highest and lowest σ_y. However, little or no pre-precipitation is expected in CM 16, with only 0.22% copper. Thus other explanations of the σ_y-$\Delta\sigma_y$ trend must be sought in this case. Possible reasons include:

1. Random variations in the σ_y of the specimens used for both the unirradiated baseline and irradiated testing produce random scatter in $\Delta\sigma_y$. However, corresponding plots of σ_y versus $\Delta\sigma_y$ will show an apparent bias of the type observed in Figure 6-2. The apparent bias increases with the scatter in σ_y. Since the number of redundant tests in the VSR study were limited, and in some cases the scatter was rather large, such apparent bias is to be expected. The scatter in σ_y adds to the scatter in $\Delta\sigma_y$, and the Cu_m derived from $\Delta\sigma_y$. However, the apparent bias does not directly confound assessment of trends in heat treatment effects of Cu_m.

2. The individual contribution of the irradiation induced features (σ_i) is less than $\Delta\sigma_y$, since σ_i must combine with other pre-existing dispersed barrier contributions (σ_u). The σ_u strength component is due to fine scale carbides and dislocation intersections that are strong obstacles dislocation slip. The carbides coarsen and the dislocations recover with increasing P_T, thus decreasing the number of pinning points and σ_u. The superposition of the σ_u and σ_i strength contributions falls between linear and root sum squares laws as [Odette and Lucas, 1998; Foreman and Makin 1967]

$$\Delta\sigma_y = \theta\sigma_{bi} + (1-\theta)(\sigma_{bi}^2 + \sigma_{bu}^2)^{1/2} - \sigma_{bu} \quad (6\text{-}4)$$

   Here θ (= 0 to 1) is a superposition parameter that depends on the strength of the weaker irradiation induced barriers, as discussed elsewhere [Odette and Lucas, 1998]. For example if $\sigma_i = \sigma_u = 150$ MPa, and $\theta = 0.4$ (a typical value for CRPs), then $\Delta\sigma_y$ is only 97 MPa. However, if σ_u is decreased to 50 MPa, $\Delta\sigma_y$ increases to 125 MPa. That is, while σ_i does not change, the net $\Delta\sigma_y$ increases by about 25% because of the lower σ_u. The solid line in Figure 6.2b shows the predicted effect on $\Delta\sigma_y$ of variations in σ_u from 40 to 210 MPa for $\sigma_i = 185$ MPa and $\theta = 0.4$. Note the σ_u scale assumes that there are 300 MPa of contributions to the total yield stress other than σ_u. Thus, at least part of the variation in $\Delta\sigma_y$ with σ_y can be understood in terms of the strength superposition mechanism. An increase in $\Delta\sigma_y$ with a decrease in σ_u due to stress relief, potentially confounds estimates of Cu_m based on the irradiation hardening data.

3. The recovery of dislocation structures during heat treatment can also influence the σ_i itself. A lower dislocation sink density (ρ_d) increases the radiation enhanced diffusion coefficient, thus accelerating CRP growth, shifting the $\Delta\sigma_y$ versus fluence curve down to lower fluence (ϕt). In the simplest case $\sigma_y \sim \alpha + \beta\sqrt{\rho_d}$ and the ϕt at a specified $\Delta\sigma_y$ is roughly proportional to ρ_d. Thus there an indirect physical relation between $\Delta\sigma_y$ and σ_y, mediated by ρ_d. The dashed line in Figure 6-2b is a crude estimate of this effect for CM11 in the VSR study. Thus, dislocation recovery during heat treatment also potentially confounds estimates of Cu_m based on $\Delta\sigma_y$ data.

It must be emphasized that the increases in $\Delta\sigma_y$ due to both superposition effects of reduced σ_u and dislocation recovery leading to faster copper diffusion are real consequences of longer t_{ir} and higher T_{ir}. Hence, these mechanisms should be considered in future research, including their influence on the start-of-life Charpy properties and the corresponding relation between ΔT and $\Delta\sigma_y$.

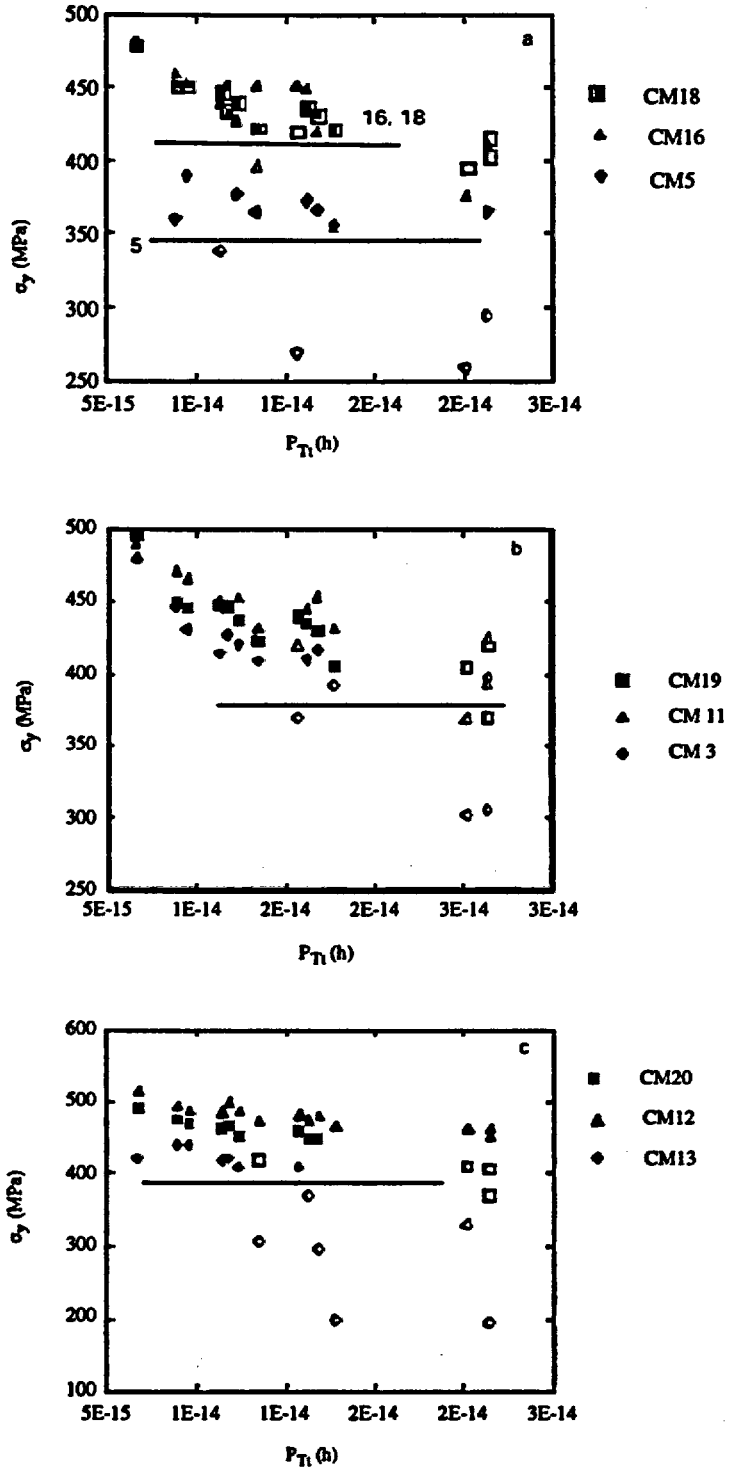

Figure 6-1 Variation of σ_y with P_{Ti} for a) CM5, 11, 18 b) CM3, 11, 19 c) CM12, 13, 20

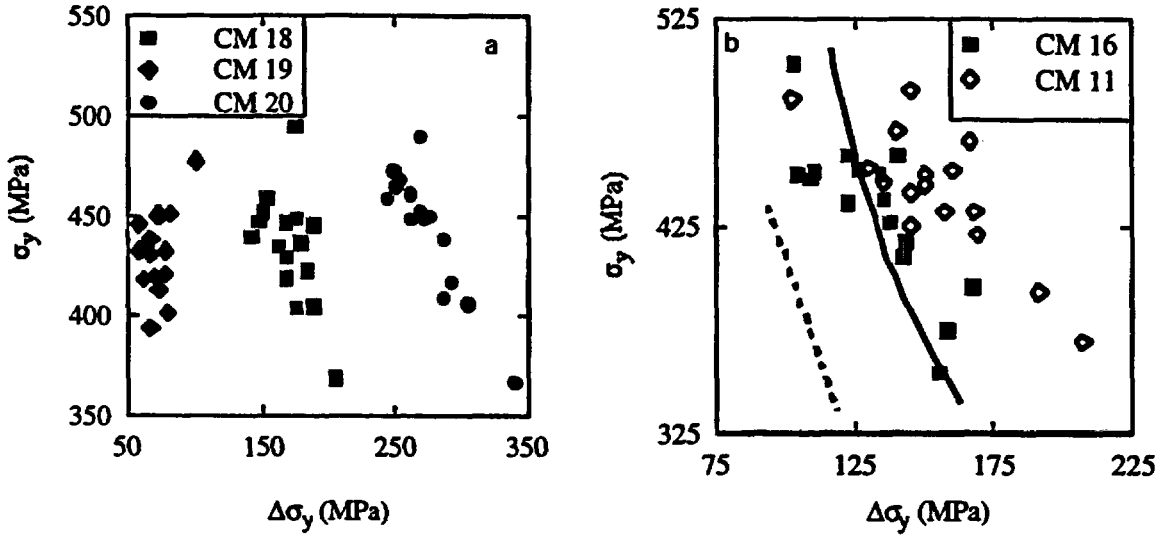

Figure 6-2 Variation of $\Delta\sigma_y$ with σ_y (unirradiated) for a) high (.42%) copper CM alloys, b) intermediate (0.8%) nickel, 0.22% copper alloys.

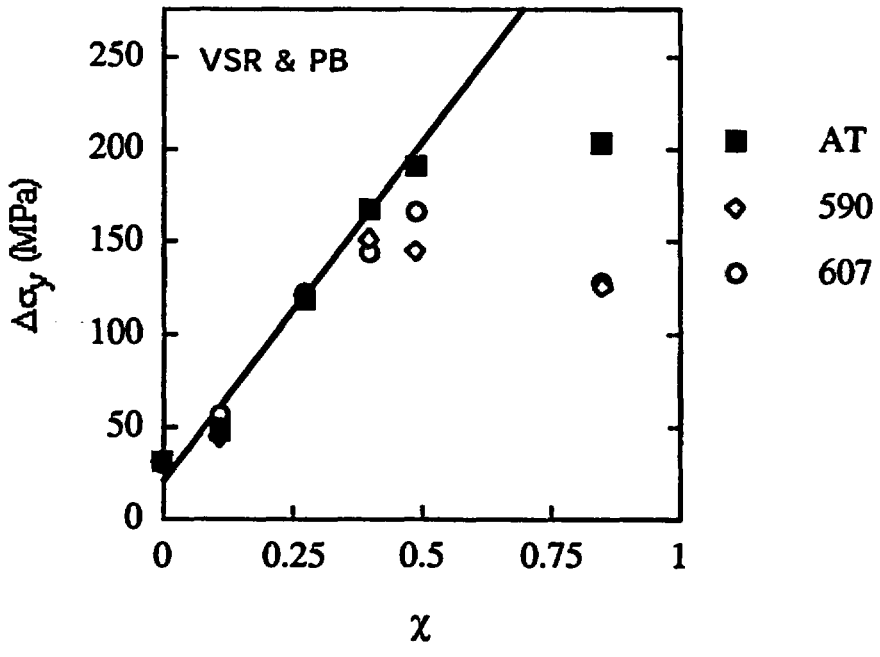

Figure 6-3 Variation of $\Delta\sigma_y$ with χ for irradiated intermediate nickel alloys.

However, it is not possible to completely disentangle σ_y reductions and dislocation recovery from the effects of copper pre-precipitation at this time. Indeed, this may not be necessary if the viewpoint is adopted that Cu_m derived from $\Delta\sigma_y$ data is a practical surrogate for all three of these real mechanisms. Nevertheless, the following procedure was used to screen the data for use in assessing matrix copper levels.

1. In order to minimize the effects of scatter, preliminary hardness measurements were made on the end tabs of most of the VSR specimens. Large variations in the unirradiated yield σ_y and/or differences in end-tab hardness between the specimens used for baseline and irradiated testing were used to screen the quality of the $\Delta\sigma_y$ data, and to eliminate the points of suspicious accuracy.

2. The $\Delta\sigma_y$ data for alloys showing significant mechanical instability during heat treatment, shown as the open symbols below the dashed lines in Figures 6-1a to 6-1c were not used to estimate Cu_m.

3. The $\Delta\sigma_y$ data for alloys that were stable, but that showed a significant reduction in σ_y relative to the other stress relief conditions for a particular steel, were also not used to estimate Cu_m. These are shown as the other open symbol in Figures 6-1a to 6-1c.

The remaining filled symbols in Figures 6-1a to 6-1c fall within σ_y and $\Delta\sigma_y$ quality limits judged to be useful for estimating the effects of heat treatment on matrix copper. It should be noted that this is scientifically and practically a conservative approach. Beyond the issue of scatter, if the other mechanisms contribute some residual fraction to reducing $\Delta\sigma_y$ due to stress relief treatments, the corresponding estimates of Cu_m will be biased towards higher levels of matrix copper.

6.2 Estimates of Matrix Copper Levels

6.2.1 Estimates of Cu_m Based on $\Delta\sigma_y$ Deviations From the Low Copper χ Trend Line

Results of the evaluation of Cu_m based on the method represented by Equations 6-1 and 6-2 are presented first. Figure 6-3 plots the $\Delta\sigma_y$ for intermediate nickel (~ 0.84%) alloys versus $\chi = (Cu_m\text{-}0.072)^{0.678}$, for both the as-tempered condition and averages for selected points for the 590 and 607°C stress relieved conditions. In order to increase the reliability of the key baseline comparison data, the as-tempered $\Delta\sigma_y$ data for the VSR study were averaged with the corresponding data from the PB irradiation at a similar flux, fluence and temperature. These averages include a small adjustment, based on the NUREG-$\Delta\sigma_y$ model, to account for minor differences in fluence (0.85 versus 1×10^{23} n/m^2) and irradiation temperature (288 versus 290°C) for PB and VSR, respectively. The average values for VSR data are for the t_{ir} of 48 and 96h at the T_{ir} of 590°C and the t_{ir} of 24 and 48 h at the T_{ir} of 607°C. The P_{Ti} at these two T_{ir} span a similar range. The data points at $\chi = 0$ are for the CM3 and CM10 alloys with $Cu_{bk} = 0.02\%$. The as-tempered PB and averaged VSR data overlap at lower Cu_{bk}. The as-tempered PB data follow a linear trend with χ up to approximately $Cu_{bk} = 0.42\%$ (CM19) but the 0.33% copper alloy (CM11) in the stress relieved condition deviates from this trend. The least square fit to the 'low' copper data (filled symbols and solid line) is $\Delta\sigma_y = 20 + 365\chi$ MPa. The 'high' copper $\Delta\sigma_y$ data (open symbols) for CM12 in both as-tempered and standard stress relief conditions and CM 11 and 19 in the standard stress relief condition fall below the trend line, indicating that $Cu_m < Cu_{bk}$ in these cases.

Table 6-1 summarizes the Cu_m found by solving Equation 6-2, which in this case is $\chi_m \sim [(\Delta\sigma_y(\text{meas.}) - 20)/365$ and $Cu_m \sim \chi_m^{1.475} + 0.072$. A similar analysis was carried out for the intermediate nickel CM and LV $\Delta\sigma_y$ data from the T14, T4 and PB capsules. The results are shown in Figure 6-4a to 6-4f and the

Table 6-1. Estimated Cu_m for Intermediate Nickel High Copper CM Alloys in VSR Study

Alloy	Cu_{bk}	Cu_m- AT	Cu_m – 590°C	Cu_m – 607°C
CM11	0.33	0.33	0.28	0.28
CM19	0.42	0.41	0.29	0.28
CM12	0.86	0.43	0.23	0.23

Table 6-2. Estimated Cu_m for Intermediate Nickel High Copper CM Alloys in Various Capsules

Alloy	Capsule	Bulk Cu	Matrix Cu - SSR	Matrix Copper as-tempered
CM11	T14	0.33	0.26	
CM19	T14	0.42	0.27	
CM12	T14	0.86	0.21	
CM18	T14	0.43	0.22	
CM20	T14	0.42	0.27	
LC	T14	0.41	0.34	
LJ	T14	0.42	0.30	
LO	T14	0.41		0.36
LK	T14	0.80	0.24	
LJ	PB	0.42	0.25	
LK	PB	0.80	0.20	
LO	PB	0.42		0.41
CM19	PB	0.42		0.43
CM12	PB	0.86		0.44
CM18	PB	0.43		0.35
CM20	PB	0.43		0.35
CM11	T4	0.33	0.28	
CM19	T4	0.42	0.29	
LC	T4	0.41	0.25	
LJ	T4	0.42	0.26	
LK	T4	0.80	0.18	
LO	T4	0.41		0.34

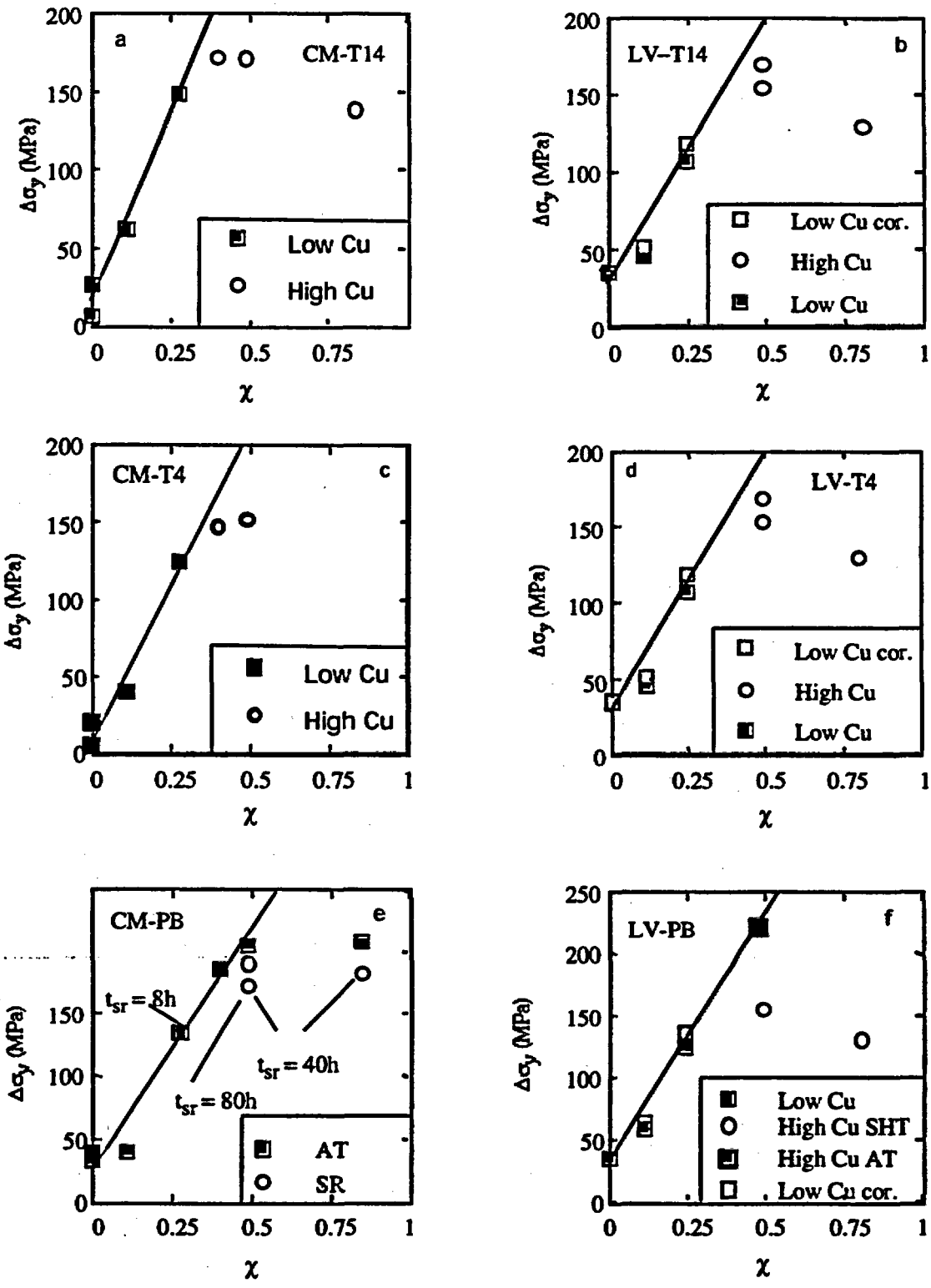

Figure 6-4 Variation of $\Delta\sigma_y$ with χ for intermediate Ni LV and CM alloys in capsules T14 (a and b), T4 (c and d) and PB (e and f)

corresponding estimates of Cu_m are given in Table 6-2 for the SSR condition.

6.2.2 Estimates of Cu_m Based on the VSR $\Delta\sigma_y$ Trends and the Modified NUREG/CR-6551 $\Delta\sigma_y$ Model

Figure 6-5a to 6-5i summarizes the $\Delta\sigma_y$ results for the screened data set for the various heat treatment conditions. The dashed line is the measured $\Delta\sigma_y$ for the as-tempered condition to help guide the eye to $\Delta\sigma_y$ differences for various T_{st} and t_{st}. The general trends can be summarized as follows.

1. In the steels with $Cu_{bk} \geq 0.3\%$, stress relief following tempering systematically reduces $\Delta\sigma_y$. The strongest effect is seen in high copper (0.86%), intermediate nickel (0.8%) CM12 alloy and the intermediate copper (0.43%), low nickel (0.0%) CM18 alloy. Similar but much weaker trends are observed in the intermediate copper (0.42%), high nickel (1.69%) CM20 alloy. The intermediate nickel (0.8%) alloys, CM11 with $Cu_{bk} = 0.33\%$ and CM19 with $Cu_{bk} = 0.42\%$, fall in between. There is also a general trend towards larger $\Delta\sigma_y$ at higher T_{st} in CM12, CM19 and CM 20. In the cases of CM19 and CM20, the $\Delta\sigma_y$ for the $T_{st} = 641°C$ stress relief are similar to the $\Delta\sigma_y$ for the as-tempered condition. The effect of t_{st} is clearest for the CM19 alloy for T_{st} from 590 to 624°C. This trend is also seen in some other cases (CM11 at 607 and 624°C, CM18 at 590°C), but is reversed, or within the scatter, for the other high copper alloys and heat treatments.

2. For the intermediate nickel (~0.85%) low copper alloys with $Cu_{bk} = 0.02\%$ (CM3) and $Cu_{bk} = 0.11\%$ (CM13) the $\Delta\sigma_y$ for the stress relieved and as-tempered conditions are similar, and suggest no general trend. The $\Delta\sigma_y$ are lower for the stress relieved conditions for the intermediate nickel (~0.85%) low copper $Cu_{bk} = 0.02\%$ (CM5) steel containing high phosphorous (0.035%). This may indicate some phosphorous removal from the matrix during stress relief, but the magnitudes of the differences are small and probably within the data scatter. Contrary to the general trend, $\Delta\sigma_y$ are generally higher for the stress relieved conditions of the intermediate nickel (0.85%) steel with intermediate $Cu_{bk} = 0.22\%$ (CM16). This may be a partial consequence of the mechanisms associated with reductions in σ_y and dislocation recovery discussed previously. However there is no overall trend in the CM 16 data, and this deviation from the norm is also probably primarily associated with scatter.

The trends in the VSR $\Delta\sigma_y$ data are certainly consistent with significant pre-precipitation in high copper steels. The behavior of the CM11 alloys with 0.33% Cu suggests that the effective maximum copper following typical T_{st}-t_{st} schedules is 0.3% or less. Further, the results are qualitatively consistent with more efficient pre-precipitation at very high copper contents (e.g., CM12) and decreasing pre-precipitation with increasing nickel content (e.g., CM 18,19, 20).

Further quantification of these results was carried out by using the modified NUREG-$\Delta\sigma_y$ model to calculate the Cu_m required to produce the measured $\Delta\sigma_y$ for the various alloys and heat treatment conditions. The basis for the modified NUREG-$\Delta\sigma_y$ model and Cu_m predictions are described in more detail in Appendix A. Briefly, however, as shown in Section 5, the NUREG-$\Delta\sigma_y$ model predictions are generally very consistent with the data from the intermediate flux T14 capsule. This consistency was found using the NUREG CRP term for welds for all of the steels irradiated in this program, irrespective of their specific product form. Similar comparisons show that the NUREG-$\Delta\sigma_y$ model overpredicts the measured $\Delta\sigma_y$ from the high flux T4 capsule. The difference between the T4 (high flux) and T14 (intermediate flux) data suggests a flux effect on $\Delta\sigma_y$. A strong and systematic effect of flux has also been observed in several other IVAR data sets. Low flux accelerates the CRP evolution and shifts $\Delta\sigma_y$ to lower fluence.

The discrepancy between the NUREG-$\Delta\sigma_y$ model predictions and T4 observations (or

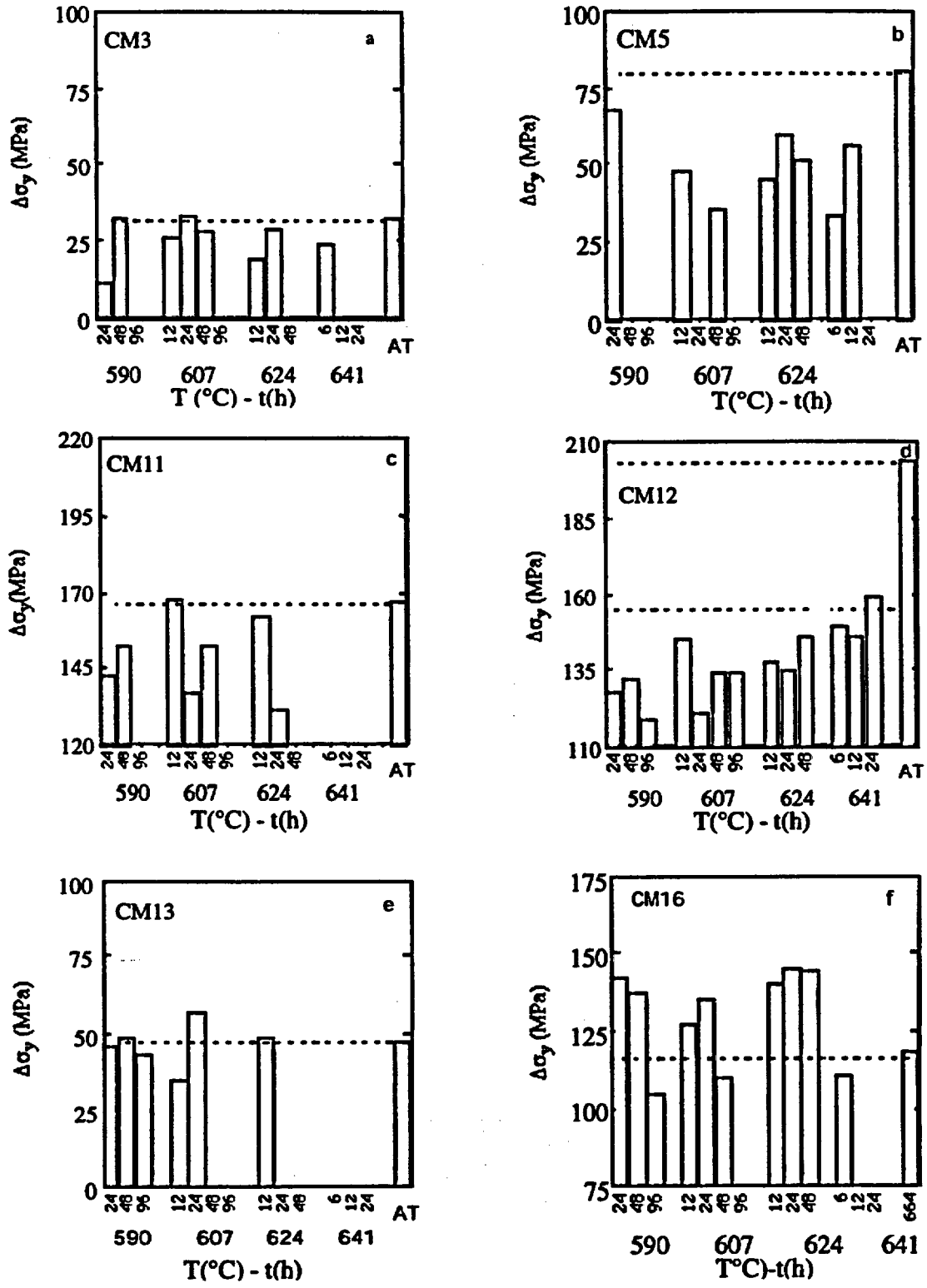

Figure 6-5 Variation of $\Delta\sigma_y$ with SR condition for a) CM3, b) CM5, c) CM11, d) CM12, e) CM13, f) CM16

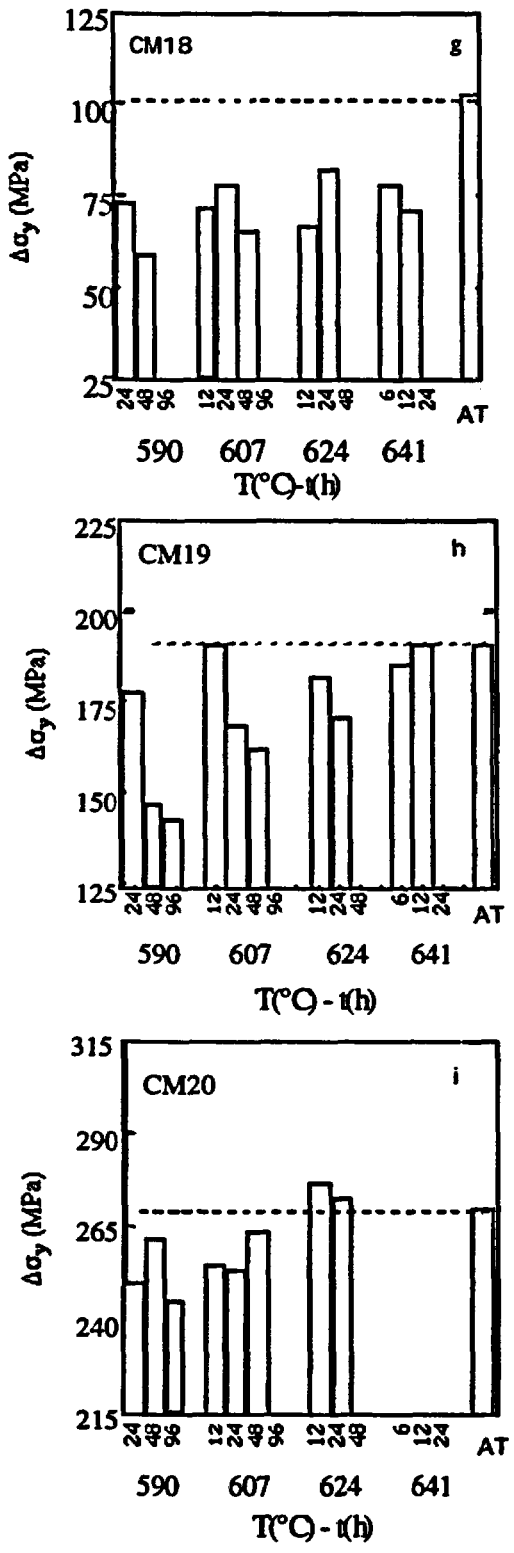

Figure 6-5 (cont.). Variation of $\Delta\sigma_y$ with SR condition for g) CM18, h) CM19, i) CM 20

between the T14 and T4 results) increases with increasing alloy nickel and manganese content. The interactive effect of composition and flux is consistent with defect trapping by these elements. Trapping increases defect recombination, hence, slows radiation-enhanced diffusion. Slower diffusion shifts the $\Delta\sigma_y$-curves to higher fluence. Details of the ongoing investigations of the effects of flux will be presented in the future. For the present purposes, however, the NUREG-$\Delta\sigma_y$ model was further modified to account for composition dependent flux effects by including a nickel dependent flux-factor $f_\phi(Ni) = 1/(1+\gamma Ni, \gamma \sim 1.3)$ that decreases the effective fluence as $\phi t_e = f_\phi \phi t$, in the CRP term of the NUREG-$\Delta\sigma_y$ model. This flux-dependent version of NUREG-$\Delta\sigma_y$ model fitted the high flux T4 data was used to estimate Cu_m for the high flux VSR data.

Figures 6-6a to 6-6e show the Cu_m estimates for the VSR study plotted against t_{ar}. The corresponding T_{ar} is indicated by the various filled symbols and Cu_{bk} by the unfilled circle. The Cu_m in all the high copper (> 0.3%) alloys are substantially less than bulk levels. For intermediate nickel (0.84% Ni) alloys, Cu_m falls below 0.25% Cu. The Cu_m generally decreases with increasing t_{ar}, and more weakly with decreasing T_{ar}, although individual data points scatter around these broad trends. The low nickel CM 18 alloy (0.02% Ni) shows a rapid drop, approaching 0.2% Cu at 40 h for T_{ar} = 590°C. In contrast, the high nickel (1.68% Ni) CM20 decreases less, with $Cu_m \sim$ 0.29 after the longest t_{ar} at the lowest T_{ar}. Figure 6-6f compares the Cu_m trend in CM19 with those for low copper alloys with Cu_{bk} = 0.22% (CM16) and 0.11% (CM 13). For clarity no distinction is made between the various T_{ar} in this case. The data for the low copper steels scatter around Cu_{bk}.

Table 6-3 summarizes the Cu_m estimates from the VSR study for the as-tempered condition and the average values for the stress relieved conditions for 48 and 96h at 590°C and 24 and 48 h at 607°. A similar analysis was carried out for as-tempered and limited stress relief data from the PB experiment. The results are shown in Figure 6-7 and the corresponding Cu_m estimates are given in Table 6-4.

Averaged results of the various estimates of Cu_m for high copper, intermediate nickel steels following typical stress relief treatments from about 590 to 610°C are summarized in Table 6-5. The overall average for the intermediate nickel steels (CM11, 19, LC and LJ) with nominal levels of Cu_{bk} from 0.3 to 0.4% is $Cu_m \sim$ 0.28%. In alloys with a high Cu_{bk} of 0.8%, the matrix copper is lower, with $Cu_m \sim$ 0.21%. This can be understood based on higher pre-precipitation nucleation and growth rates in steels that start with higher copper in solution. The matrix copper in the high nickel alloy (CM20) is larger with $Cu_m \sim$ 0.31%. The $Cu_m \sim$ 0.27% in the low nickel steel (CM18), is similar to that for the intermediate nickel alloys; however, this limited data may be biased by the high estimate of Cu_m from the PB capsule.

These estimates of Cu_m based on $\Delta\sigma_y$ measurements are subject to considerable uncertainty, but reflect relative trends and the 'practical' effects of stress relief. They support the following general conclusions:

1. Typical heat treatments in the range of 590-610°C for periods between 20 and 80 h of intermediate nickel, high copper ($Cu_{bk} \leq$ 0.3%) steels result in a reduction of Cu_m to below 0.3% Cu, with even lower values frequently observed.

2. General trends towards decreasing Cu_m with decreasing nickel, very high copper, lower T_{ar} and longer t_{ar} are observed. However, the data do not allow precise quantification of these effects.

3. The best maximum copper fit value of 0.25%Cu for intermediate nickel welds in the PREDB is credible and consistent with these result of this study. The observation

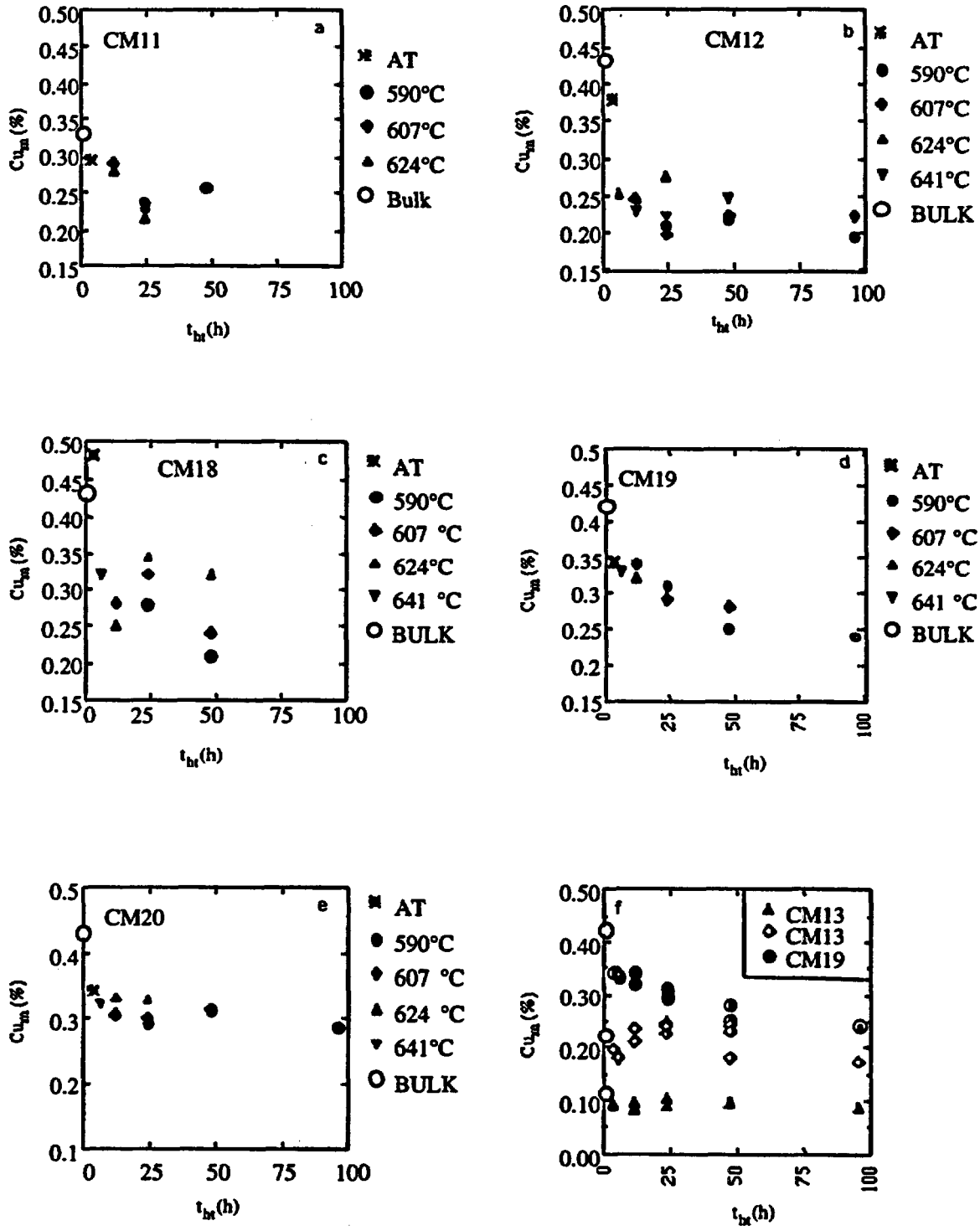

Figure 6-6 $\Delta\sigma_y$-based NUREG model prediction of the variation in Cu_m with SR time for the VSR data for a) CM11, b) CM12, c) CM18, d) CM 19, e) CM20; f) Comparison of high Cu CM19 to two lower copper steels

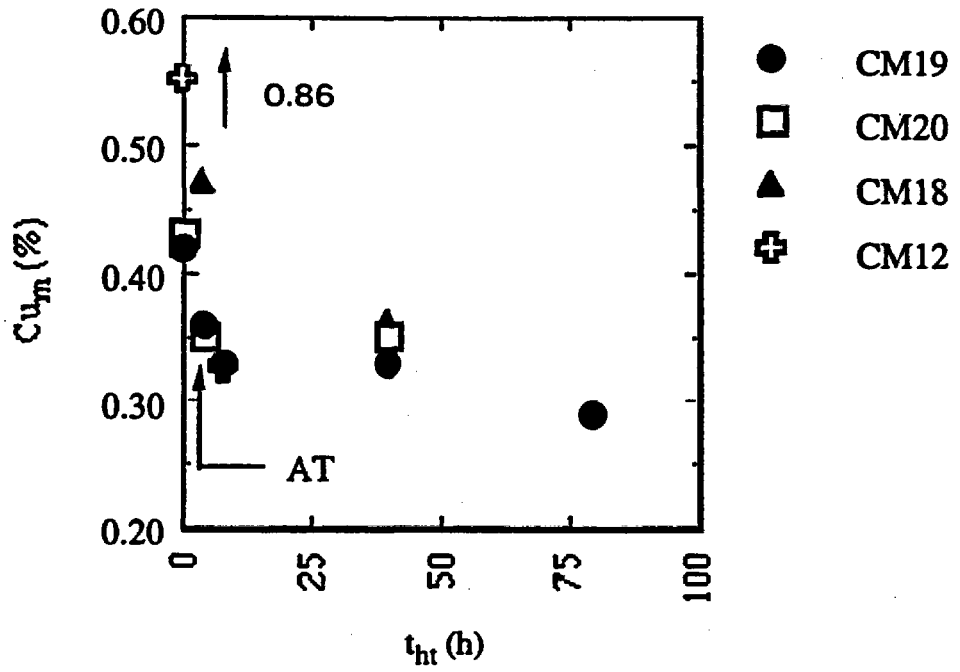

Figure 6-7 $\Delta\sigma_y$-based NUREG model prediction of the variation in Cu_m with stress relief time for the PB data for CM12, CM18, CM19, CM20

Table 6-3. Estimated Cu_m for High Copper CM Alloys in VSR Study

Alloy	Cu_{bk}	AT-Cu_m	590°CCu_m	607°C-Cu_m
CM11	0.33	0.29	0.26	0.25
CM19	0.42	0.34	0.25	0.29
CM12	0.86	0.38	0.21	0.21
CM18	0.43	0.48	0.21	0.28
CM20	0.43	0.34	0.30	0.31

Table 6-4. Estimated Cu_m for High Copper CM Alloys in the PB Study

Alloy	Cu_{bk}	AT-Cu_m	607°C/8h-Cu_m	607°C40h-Cu_m	607°C-80h-Cu_m
CM12	0.86	0.37	-	0.32	-
CM18	0.43	0.47	-	0.35	-
CM19	0.42	0.36	0.33	0.33	0.29
CM20	0.43	0.33	-	0.35	-

Table 6-5. Averaged Cu_m Following Heat Treatment at ~590-610°C

	Cu_{bk}/Ni	T14	T4	PB	PBSR	VSR-1	VSR-2	AVG
CM11		0.26	0.28			0.25	0.28	0.27
CM19		0.27	0.29		0.31	0.27	0.28	0.28
LC		0.34	0.25					0.30
LJ		0.30	0.26	0.25				0.27
CM12		0.21			0.32	0.22	0.23	0.24
LK		0.24	0.18	0.20				0.21
CM20		0.27			0.35		0.32	0.31
CM18			0.22		0.35			0.27

that this maximum is lower in low nickel steels and higher in high nickel steels is also broadly consistent with the present results. However, these statistical fit results do not preclude a slightly higher actual maximum copper or a heat-to-heat variability in this value depending on many details of the alloy and its processing history.

6.3 Microanalytical Assessments of Cu_m

The Cu_m estimates based on $\Delta\sigma_y$ data have been complemented by limited microanalytical studies that are summarized below. These include field emission scanning transmission microscopy (FEGSTEM) carried out at AEA Harwell, electrical resistivity and Seebeck coefficient measurements and small angle neutron scattering (SANS).

6.3.1 Field Emission Gun Scanning Transmission Electron Microscopy

Table 6-6 summarizes the FEGSTEM results on Cu_m for CM 19, CM 20 and CM 12. Most of these measurements were made after a so-called UK quench and temper (Q&T) which differed somewhat from the UCSB base Q&T. However, the alternative Q&T are not expected to make a substantial difference to the Cu_m results.

An intercomparison of these and other results is given below. However, overall they are very consistent with results of the Cu_m assessment based on the $\Delta\sigma_y$ data trends.

6.3.2 Electrical Resistivity

As discussed in Section 3, electrical resistivity, ρ, of metals and alloys can be precisely measured. While there are many contributions to resistivity, in dilute alloys the total is usually dominated by the resistance of the pure solvent (e.g., ρ_{Fe}) plus dissolved solutes (e.g., Cu, Ni, Mn,...), with lesser contributions from microstructural defects, trace impurities and precipitates, ρ_m [Rossiter, 1987]. In RPV steels, these 'other' factors typically contribute about 3 $\mu\Omega$-cm, out of a total of more than 20 $\mu\Omega$-cm. The ρ of simple dilute binary alloys can be precisely related to the solute distribution. Alloying and impurity elements located in large precipitates contribute little to ρ and to first order can be neglected [Rossiter,

Table 6-6. FEGSTEM Estimates of Cu_m for CM12, CM19 and CM20

Alloy	T_{ht}(°C)	Cu_m (As Quenched)†	Cu_m (t_{ht} short -h)	t_{ht} = int. (h)	t_{ht} long (h)
CM 19	550	0.35 ±0.05	—		
CM19	600	0.35 ±0.05	0.34 ±0.04 (8)	0.32±0.05 (40)	0.25±0.05 (80)
CM19	630	0.35 ±0.05	0.29 ±0.05 (8)	0.30±0.03 (40)	0.24±0.05 (200)
CM19	660	0.35 ±0.05	0.36 ±0.03 (4)	0.31±0.03 (40)	—
CM19*		—	0.42 ±0.03 (8)	0.28±0.03 (40)	0.27±0.07 (80)
CM12	660	—	0.49 ±0.05 (4)		—
CM12	600	—	—	0.28±0.05 (40)	—

* Tempered at 660°C for different times; stress relieved at 600°C
† UK base was as quenched

1987]. The resistivity coefficients (k_i) of common elements (i) dissolved in iron are known or can be established. For example, in the case of copper, $k_{cu} \sim 3.5\mu\Omega$-cm/wt% [Mathon, 1995]. In the dilute solution range, the resistivity coefficients are approximately independent of composition ($\rho_i = k_i C_i$), although deviations from such linearity occur for some elements like manganese (perhaps due to clustering). Further, to first order, the net contribution of different solutes in more complex dilute solutions is simply the linear sum of the individual contributions.

$$\rho \sim \rho_{fe} + \rho_{ms} + \Sigma_i k_i C_i \qquad (6\text{-}5)$$

Consider an idealized case of a set of complex alloys that are identical except for the amount of one element x illustrated in Figure 6-8. In this example, the ρ of the alloy with $C_x = 0$ is $\rho_0 = \rho_{fe} + \rho_{ms} = 22\ \mu\Omega$-cm and $k_x = 5\ \mu\Omega$-cm/%x. Based on the assumptions listed above the ρ of the alloys would increase with the bulk solute content C_{xb} up to the point where precipitation occurs at ρ_e. For equilibrium conditions the ρ would remain constant at higher C_{xb} (filled circles). The break point at $\rho = 23.5\mu\Omega$-cm defines the solubility limit of $C_{xe} = 0.3\%$. Thus alloys with $C_{xb} > C_{xe}$ and measured $\rho_{m1} > \rho_e$ (e.g., the open circle with $C_{xb} = 0.6\%$ and $\rho_{m1} = 24\ \mu\Omega$-cm) reflects non-equilibrium levels C_{xm1} in solution. The C_{xb1} can be determined by the fit to the alloys with C_{xb} less than the solubility limit (dashed line) as

$$C_{xm1} = (\rho_{m1} - \rho_0)/k_x = (24 - 22)/5 = 0.4\%. \qquad (6\text{-}6)$$

Precipitation following additional stress relief or irradiation would be reflected in ρ_{m2} (= 23.75) < ρ_{m1}, hence, lower dissolved C_{xm2} (=0.35%).

Such idealized conditions cannot be met in practice, except in the simplest cases. Complications include alloy-to-alloy variations in solutes other than x, including the effects of precipitation during processing and confounding variations due to other uncontrolled contributions from microstructure. However, the approach illustrated in Figure 6-8 can be facilitated by calibrating the k_i plus a general alloy category term, ρ_j, accounting for all other factors for a particular alloy class j, including contributions from microstructure and precipitates. Further a term can be added to account for any second order nonlinearities in the composition dependence of $\rho_i = k_i C_i + k_i' C_i^2$. Thus Equation 6-5 is modified as

$$\rho \sim \rho_j + \Sigma_i (k_i C_i + k_i' C_i^2) \qquad (6\text{-}7)$$

Fitting Equation 6-7 requires a set of alloys with a range of known compositions. The k_i can be found only where there is a significant variation in C_i. Further, the C_i must be corrected for the fraction that is not in solution, thus not contributing to ρ. For the present purposes this means that alloys with 'high' copper cannot be used in the fit, since the corresponding Cu_m are not known. However, since the corrections are generally small, other elements were considered to be in solution at bulk levels (e.g., Mn) or completely precipitated (e.g., C), hence lumped in with ρ_j. Finally, it is assumed that the ρ_j accounts for all other factors in alloys in category j.

Equation 6-7 was fit to alloys in four classes: a) the VM series of simple ferritic alloys with variations in Cu, Mn, C and N and heat treated to retain copper in solution; b) the LV alloy series in its standard stress relief condition and one high copper alloy in the as-tempered condition (LO); c) the CM alloys series in the standard stress relief condition; and d) the CM alloys series in the as-tempered condition. The k_i terms included Cu, Ni, Mn, Si and P. Only Mn benefited from a nonlinear k_i term. The effects of other compositional variables (C, N, Mo,..) were generally too small to be established and were lumped into the ρ_j term. As noted above, all alloys were assumed to have dissolved solute levels equal to the bulk chemistry with the exception of copper.This clearly is an approximation, particularly for the manganese which is incorporated into M_3C phases in carbon containing alloys, as well as for low solubility elements like phosphorous.

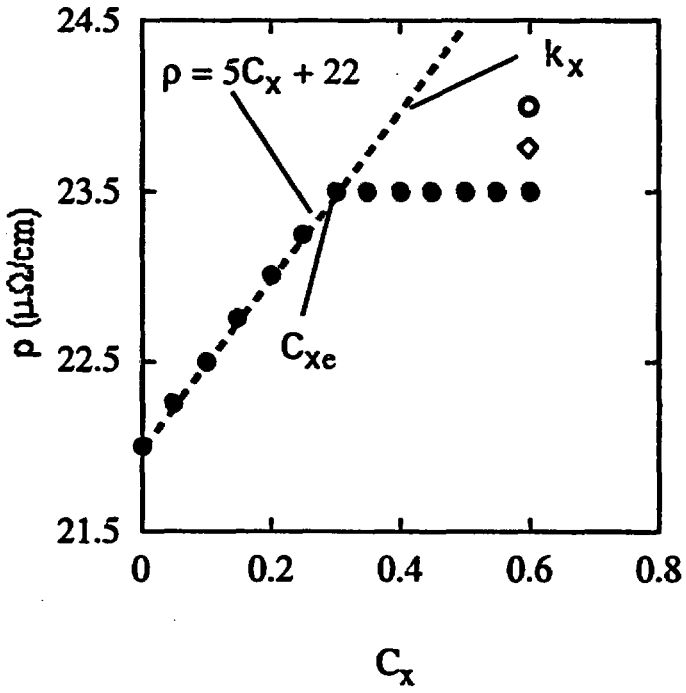

Figure 6-8 Idealized variation of resistivity with content C_x of solute x.

The resistivity data trend themselves were used to guide the assumptions concerning the definition of low copper alloys fit to Equation 6-7: VM $Cu_m = Cu_{bk}$; LV and CM-standard stress relief Cu_m up to 0.22 % copper; CM-as-tempered Cu_m up to 0.33% copper.

The k_i and ρ_j were used to normalize the measured ρ to a common composition and alloy condition: Mn = 1.6%, Ni = 0.8%, Si = 0.15% P = 0.005%, Ti = 0.0 and VM. Figure 6-9 shows the resulting variation in a normalized resistivity, ρ_n, with copper. The overall standard error in the fit is ±0.25 μΩ-cm, or only about 1 to 3% of the measured values. The individual fit parameters are given in Table 6-7. The k_i are also generally in agreement with published values. The low copper data used in the fitting are shown as the filled symbols. A least squares fit line to all this data gives a k_{cu} = 3.54 μΩ-cm/% Cu in excellent agreement with results in the literature [Mathon, 1995]. The standard error for this fit to the ρ_n data was ±0.2 μΩ-cm. The open symbols are for the high copper alloys not used in the fitting, since their Cu_m were unknown.

The high copper ρ_n data for the CM alloys fall below the low copper fit line, indicating pre-precipitation. This is also the case for the intermediate nickel (0.85%), high copper (0.42%) LC alloy. However the other high copper LV alloys with lower (LA and LB) and higher (LD) nickel contents fall on or above the low copper fit line. This suggests that in addition to this contribution to ρ_i, nickel may also influence the microstructure term, ρ_j.

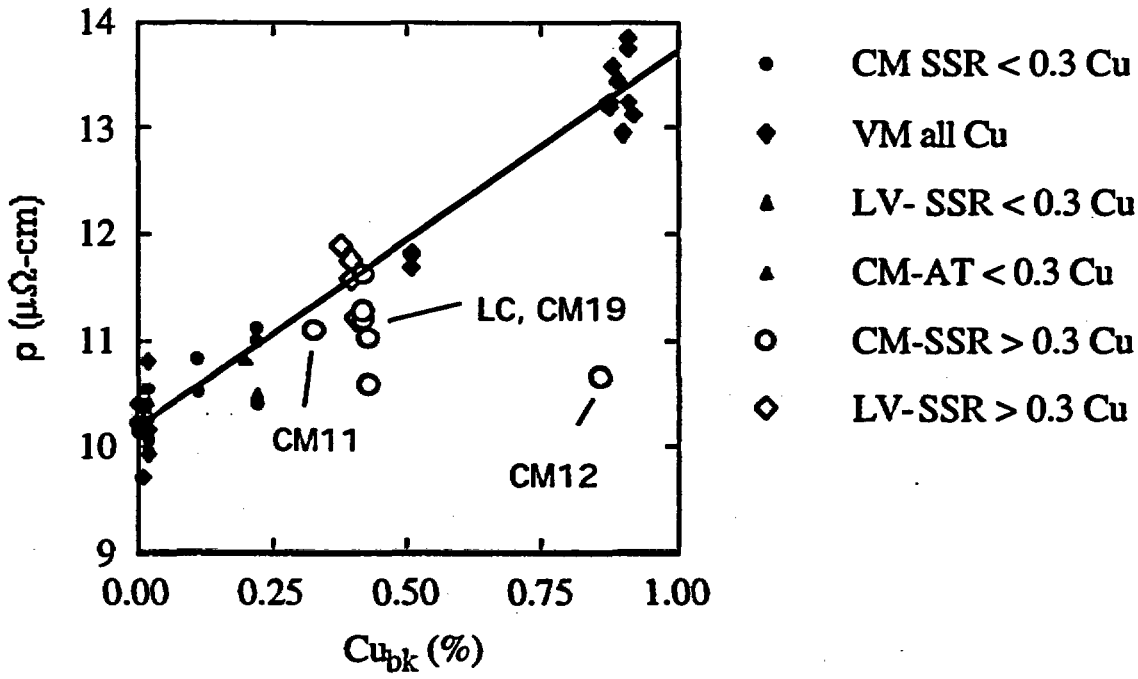

Figure 6-9 Variation of resistivity with copper content for a range of alloys

In order to further minimize possible effects of heat-to-heat variability in estimating Cu_m, analysis of the normalized resistivity data was restricted to the intermediate nickel alloys. The low copper data were fit both with (solid lines) and without (dashed lines) an imposed k_{cu} = 3.5 μΩ-cm/% Cu. Figure 6-10a shows the results for the CM series with about 0.85% nickel in the standard stress relief condition. The estimated Cu_m for alloys with Cu_{bk} = 0.33% (CM11) and 0.42% (CM19) are Cu_m = 0.20±0.01 and

0.24±0.02 respectively. Note, somewhat higher values are found if the data point for CM10 with 0.02% copper is included in the analysis. However, since this data point is inconsistent with the trend for other low copper alloys (CM3, CM13 and CM16), it was not used in the analysis. The corresponding Cu_m estimate for the CM12 alloy with Cu_{bk} = 0.86% copper is also unrealistically low (< 0.1% Cu), perhaps also indicating an effect of very high copper on ρ_j. Since this value is well below the solubility limit at 607°C, it is not shown. Figure 6-10b shows the corresponding result for the LV alloys. The ρ of alloy LC with Cu_{bk} = 0.42% deviates from the lower copper trends (LG, LH and LI), with an estimated Cu_m = 0.3±0.01. Figure 6-10c shows the results for the CM series in the as-tempered condition. In this case, as expected, both the CM19 and CM12 show higher estimated values of Cu_m ~ 0.32 and 0.48%Cu, compared to the standard stress relief condition. Unfortunately there is not sufficient data to carry out a similar analysis on the high and low nickel CM series.

In summary the ρ-based Cu_m estimates for the high copper steels are consistent with significant pre-precipitation of copper during both tempering and stress relief and stress relief heat treatments. For the standard stress relief condition Cu_m ~ 0.2-0.3%. The lowest Cu_m was found for the alloy with the highest copper (CM12). This Cu_m is quantitatively unreliable, but the indicated trend is qualitatively consistent with the previous analysis.

6.3.3 Seebeck Coefficient

As described in Section 3, the Seebeck coefficient (S, μV/°C) can be measured precisely and is also sensitive to the concentration of dissolved solutes in alloys and to a lesser extent microstructure [Pollock, 1991; Miloudi et al, 1999, 2000]. The effect of solutes can be described by element-specific κ_i factors in forms roughly analogous to Equation 6-7. Most, but not all, solutes have negative κ_i, hence, S usually decreases with increasing C_i. Thus an analysis similar to that used to estimate Cu_m from the ρ data was carried out based on measurements of S in the VM, CM and LV series alloys. However, there are some possible differences between the S and ρ behavior that require some modifications of the approach. First, the dependence of S on C_i is generally not well established. Further, both theoretical considerations and experimental observations suggest that the S-dependence may be non-linear and sensitive to the total alloy solute content [Pollock, 1991]. Thus the effects of C_i on S are represented by linear (κ_i), non-linear (κ_i') and a solute-total solute interactive ($\kappa_{ii}\Sigma_i C$) terms as

$$S = S_j + \Sigma_i(\kappa_i C_i + \kappa_i' C_i^2) + \kappa_{ii}\Sigma_i C_i \qquad (6\text{-}8)$$

Fitting Equation 6-8 to the VM, CM and LV series database showed that good results could be obtained without the $\kappa_{ii}\Sigma_i C_i$ terms, and that nonlinear terms were (moderately) significant only for nickel and copper. The fitting results are also given in Table 6-7. Note, not only do the κ_{ii} have different values than ρ but they also vary in sign (e.g., $\kappa_{mn} > 0$). The standard error of the fit was about 0.22 μV/°C or roughly 2 to 3% of the measured S. The normalized S_n versus Cu_{bk} is shown in Figure 6-11. The normalization procedure and symbol designation showing low copper (fitted - filled) versus high copper (not fitted-unfilled) are the same as those used in the ρ plots. The

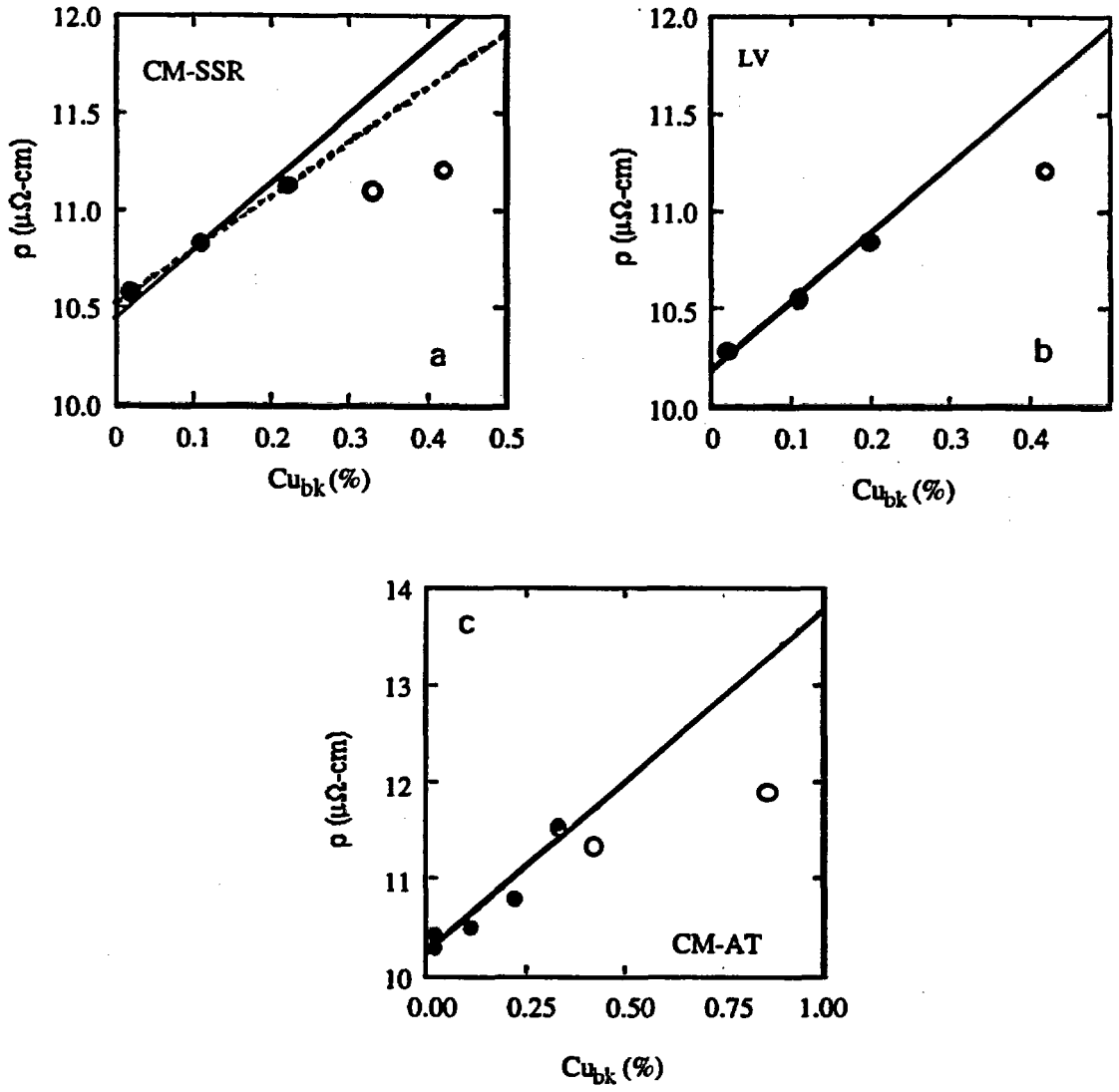

Figure 6-10 Variation of resistivity with copper content for a) CM, b) LV and c) as-tempered CM alloys.

Table 6-7 Least square fit calibration of Equations 6-7 and 6-8

Technique, Parameter	Fe + "Microstructure" r_j (μ-cm) S_j(μV/°K)				Elements – k_i (μW-cm/%i, k_i(μV/°K/%i)								
	LV_w	VM	CM_w	CM_a	Si*	Ti*	P*	Mn	Mn^2	Ni	Ni^2	Cu	Cu^2
ρ, k_i	15.1	10.5	14.8	13.9	2.5	1.78	12.2	6.56	1.05	2.42		3.52	
S, κ_i	8.0	13.7	10.3	10.1	3.56	0.49	16.1	0.24		1.62	0.31	5.94	0.54

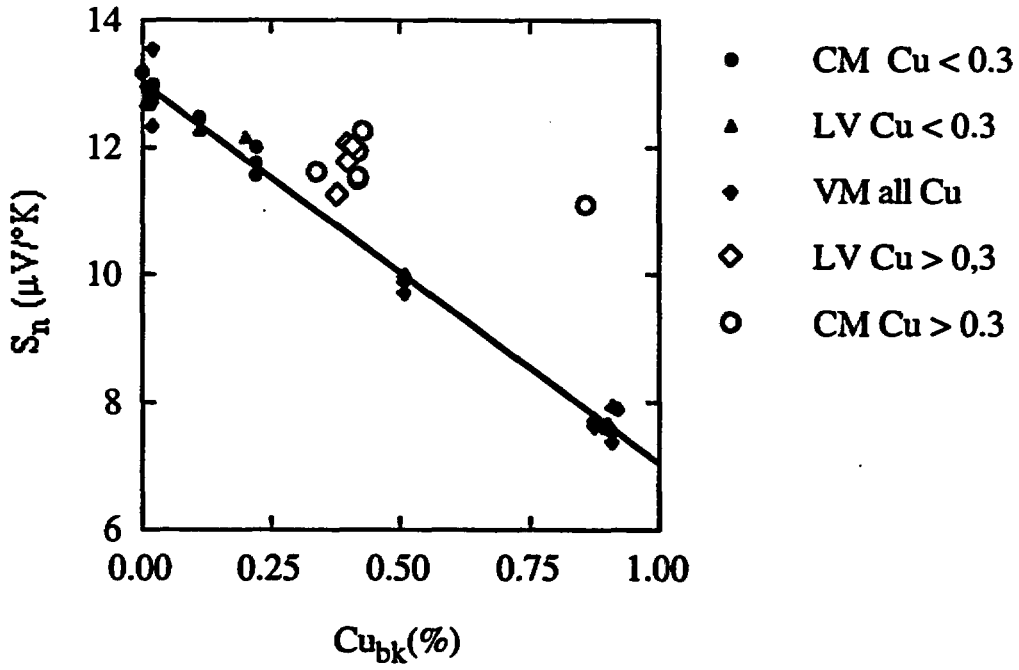

Figure 6-11 Variation of Seebeck coefficient with copper content

normalized S decreases with increasing Cu_m with a linear slope of -5.98 μV/°C/%Cu. This is about 16% less than the value reported for iron-copper binary alloys reported in the literature [Miloudi et. al, 2000] and may reflect the interactions and non-linearities noted above. The S_n data for high copper alloys fall above this line, again indicating pre-precipitation.

The overall standard error to the simple linear trend line of 0.2 μV/°C indicates that a simpler expression in the form

$$S = S_j + \kappa_{cu} x_{cu} \qquad (6\text{-}9)$$

can be used to estimate Cu_m for the high copper steels. In order to minimize the effects of alloy-specific confounding factors not accounted for, Equation 6-9 was again fitted to the various individual subsets of the normalized (e.g., corrected for composition and alloy category) intermediate (~0.85%) nickel CM and LV S_n data. However, in this case no effort is made to fix κ_{cu} at a nominal value.

The results are shown in Figure 6-12. The data for the model VM alloys are included but are not used in the fitting. Figure 6-12a shows the results for the CM standard stress relief condition. The fitted κ_{cu} is 5.61 μV/°C/%Cu, reasonably close to the overall fit to the data. For the alloys with Cu_{bk} = 0.33% (CM11), 0.42% (CM19) and 0.86% (CM12) the estimates are Cu_m = 0.25, 0.19 and 0.35%, respectively. Figure 6-12b shows the corresponding results for the CM series in the as-tempered condition. In this case κ_{cu} = 5.57 μV/°C/%Cu is essentially the same as for the standard stress relief case. As expected, however, the corresponding Cu_m are generally higher for the as-tempered relative to the standard stress relief condition with values of Cu_m = 0.25, 0.26 and 0.42% respectively, for CM11, CM19 and CM12. Figure 6-12c shows the results for the LV series. The estimated Cu_m for the intermediate nickel (0.86%) high copper alloy (LC) is 0.24% Cu.

In summary the S-based Cu_m estimates for the high copper steels are also consistent with significant pre-precipitation of during both tempering and stress relief heat treatments. For the standard stress relief condition Cu_m for high copper alloys ranged from ~ 0.19-0.25%. The estimated Cu_m for the alloy with very high copper (CM12) gave the highest Cu_m = 0.35, which is qualitatively inconsistent with the other data trends and may be due to an effect of very high copper on S_j.

6.4 Summary and Discussion of the $\Delta\sigma_y$ and Microanalytical Based Estimates of Cu_m

Table 6-8 summarizes the microanalytical estimates of Cu_m for intermediate nickel, high copper steels for typical as-tempered and stress relieved conditions. Note however, the specific heat treatments in these broad categories vary slightly. For example, most of the FEGSTEM CM data involve a so-called UK austenitize-temper treatment and air/furnace cooling following isothermal stress relief. This differs somewhat from heat treatment schedules used in this program. The ρ and S data are for the CM and LV alloys are in their specified as-tempered (CM) and standard stress relieved conditions (LV and CM). The $\Delta\sigma_y$/VSR entries are averages for both a range of typical T_{sr} = 590-610°C and t_{sr} = 24-96 h, as well as for different Cu_m assessment methods. Overall there is reasonable agreement. These results are summarized in Figure 6-13.[3]

[3]Recent results have been obtained that provide further support for the conclusion reached in this section regarding copper in solution following stess relief heat treatment for intermediate nickel steels. These new results include the following items. 1) Changes in both Seebeck coefficient (ΔS) and resistivity (Δρ) measurements on CM, LV alloys and several welds following irradiation show a similar pattern to the trends for the absolute values of these parameters (S and ρ) in the unirradiated condition as shown in Figures 6-9 and 6-12. That is, the low copper steels follow a linear trend but at higher copper levels the ΔS and Δρ fall below the linear trend line indicating pre-precipitation. For alloys with Cu_{bk} > 0.30% a preliminary analysis indicates an

6.5 Small Angle Neutron Scattering Studies from the PB Experiment

Figure 6-14 shows data from Small Angle Neutron Scattering studies on the effect of t_{ar} from 0 to 80 h for T_{ar} = 607°C on the CRP features for the high copper (0.42%) intermediate nickel (0.85%) alloy (CM19) irradiated in the PB capsule [Wirth, 1998]. Figure 6-14 shows both the total CRP volume fractions (f_{crp}, filled circles) and the corresponding estimates of the copper volume fraction (f_{cu}, unfilled circles), based on the magnetic to nuclear scattering ratio. Figure 6-14 also shows the SANS volume fraction data for the CM19 with t_{ar} = 24h at T_{ar} = 600°C, irradiated in the T4 capsule (open triangle). The x symbol is an adjustment to approximately account for the lower fluence of T4 (0.75×10^{23} n/m^2) versus the PB (1×10^{23} n/m^2) capsule based on the corresponding ratio of the NUREG CRP fluence functions (see Appendix A). The f_{cu} decreases with increasing t_{ar} to values of $f_{cu} \sim 0.25\%$, consistent with the corresponding evaluations of Cu_m described above. Clearly the effects of t_{ar} on Cu_m in the unirradiated condition are reflected in the f_{cu} following irradiation. However, the f_{cu} cannot be used to directly evaluate Cu_m, since precipitation is presumably not complete at this fluence. However, the relative values are certainly meaningful and also correlate well with the $\Delta\sigma_y$ changes. Further, since the as-tempered alloy has a nominal $f_{cu} \sim Cu_{bk} \sim 0.42\%$, it is not completely unreasonable to assume that $f_{cu} \sim Cu_m$. The open diamonds are adjustments to estimate the saturation f_{cu} based on dividing the experimentally derived f_{cu} values by the NUREG CRP fluence function for the PB and T4 capsules. These estimates of the saturation f_{cu} also fall below 0.3% at long t_{ar}

---

average $Cu_m \sim 0.26 \pm 0.03\%$. 2) Recent AP data reported by Miller show Cu_m in the range of 0.19 to 0.27% for a weld with Cu_{bk} = 0.3% depending on the stress relief temperature and cooling rate. Note the effect of air versus slow cooling following a stress relief at 607°C for 24h was also explored in this study. No systematic pattern was observed in the $\Delta\sigma_y$ for the high copper CM alloys (11, 12, 19 and 20) for these two cases. The average difference in $\Delta\sigma_y$ was approximately zero. Thus while slow cooling is expected to lead to lower Cu_m, the effect does not appear to be large at least in this case.

Table 6-8. Microanalytical and $\Delta\sigma_y$ Based Estimates of Cu_m for Typical As-tempered and stress-relieved conditions

Alloy/HT	FEGSTEM	ρ	TEP	$\Delta\sigma_y$(av)	Av.
CM19/AT	0.36	0.32	0.26	0.38	0.34
CM11/AT		0.33	0.25	0.33	0.30
CM12/AT	0.49	0.48	0.42	0.39	0.43
CM19SR	0.28	0.23	0.19	0.28	0.25
CM11/SR		0.19	0.25	0.26	0.23
CM12/SR	0.28		0.34	0.24	0.23
LC/SR	0.28	0.30	0.24	0.27	0.27
CM18/SR				0.27	0.27
CM20/SR				0.31	0.31

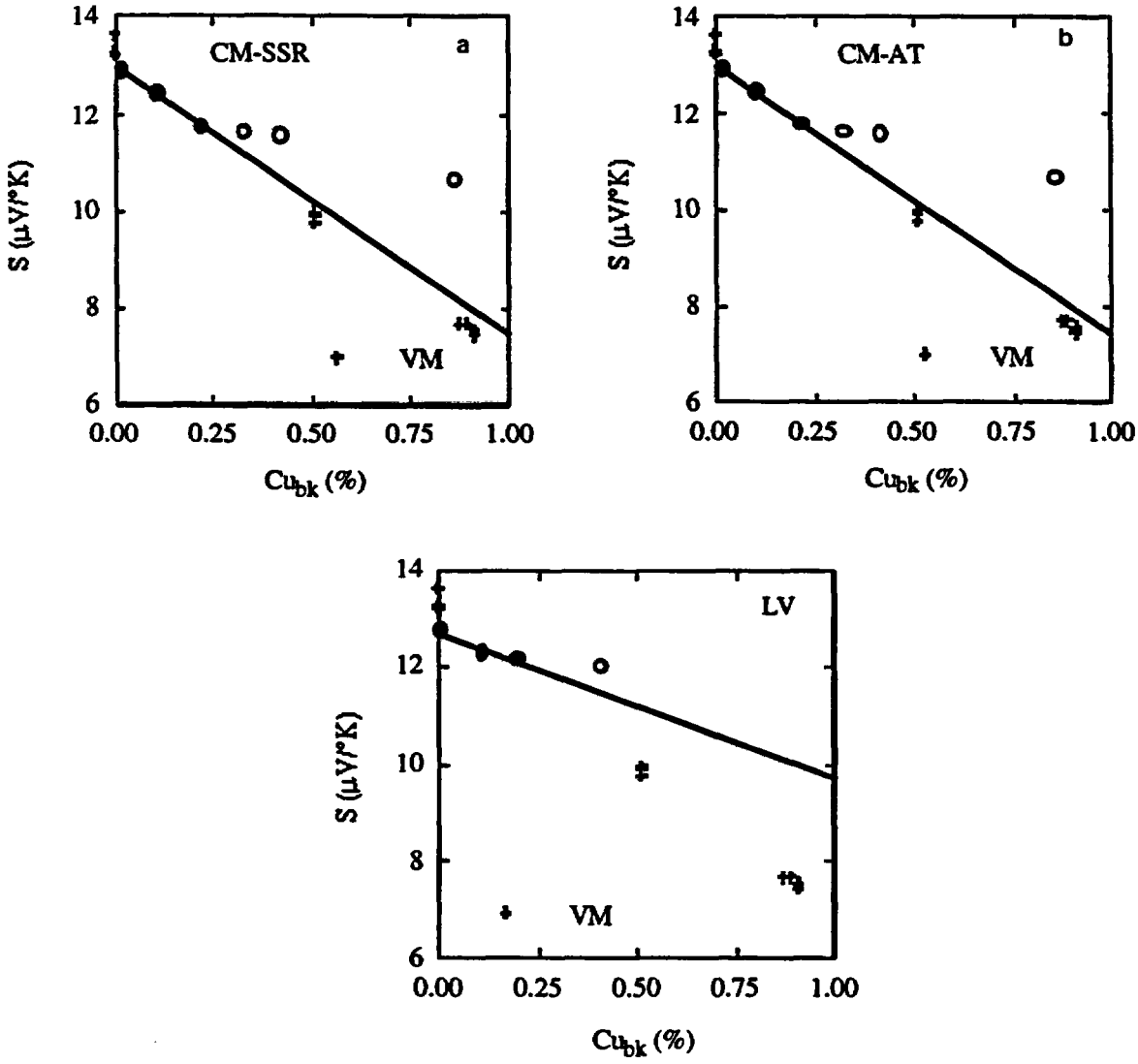

Figure 6-12 Variation of Seebeck coefficient with copper content for a) stress-relieved CM, b) as-tempered CM and c) LV-series alloys.

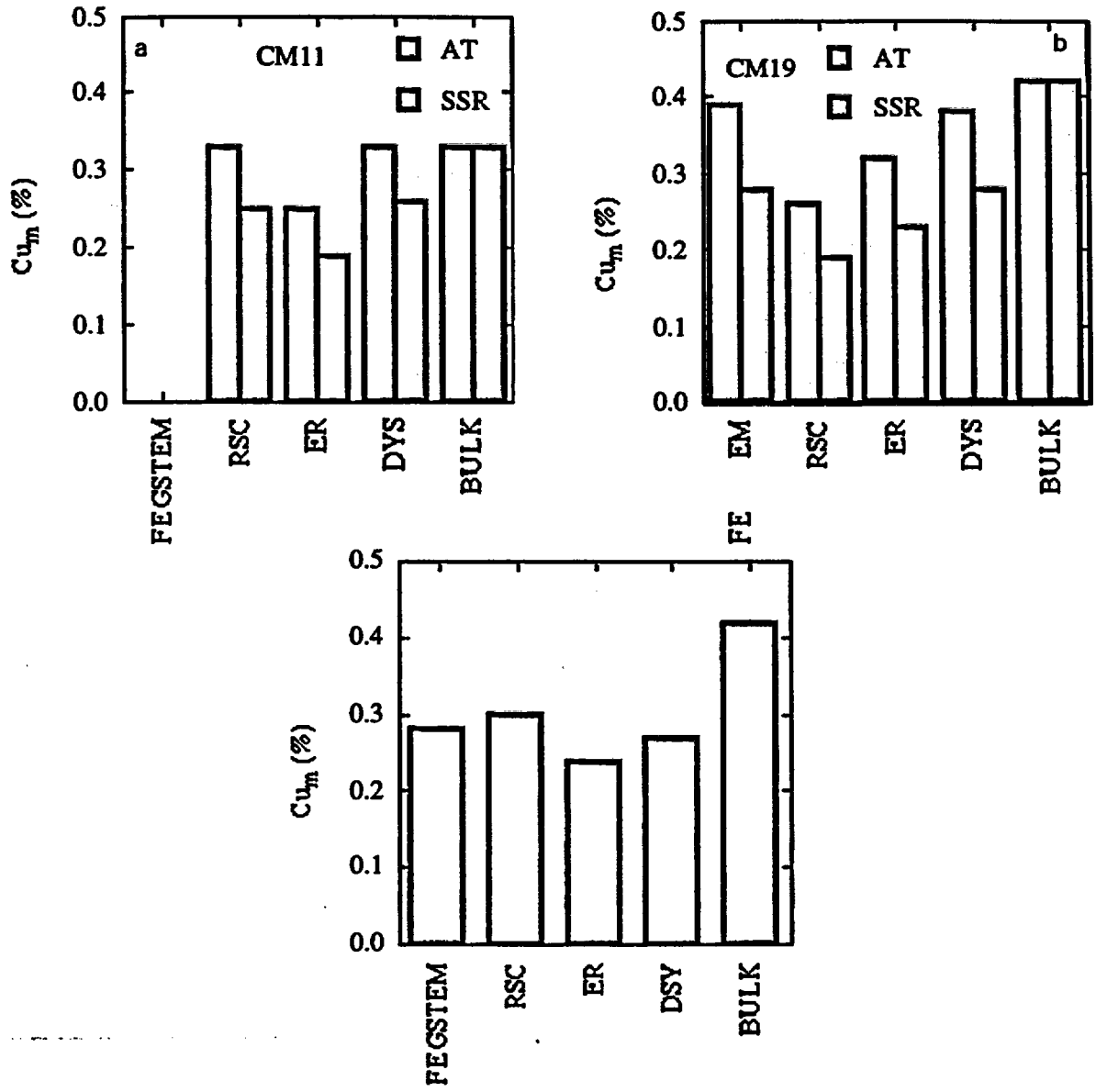

Figure 6-13 Cu_m measurements from various techniques for a) CM11, b) CM19, c) LC

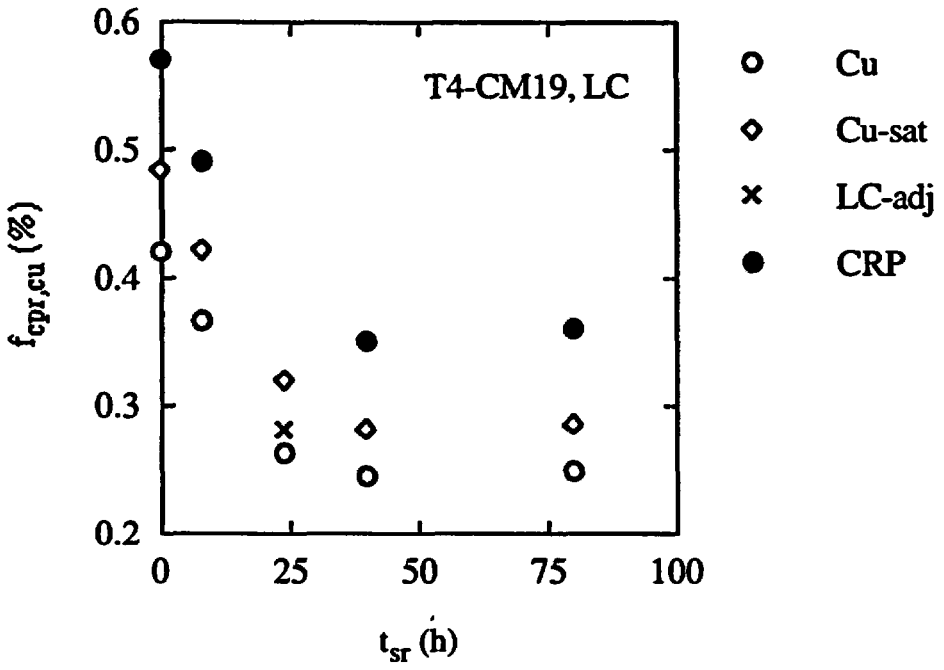

Figure 6-14 Effects of t_{sr} on CRP features as measured by SANS on CM19 from the PB capsule.

7 A PRE-PRECIPITATION MODEL FOR Cu_m

As noted above the data developed in this study are not sufficiently accurate to derive a detailed time-temperature-precipitation C-curve model relating Cu_m to the Cu_{bk}, T_{sr}, t_{sr}, as well as metallurgical factors such as nickel and bulk copper content. However, it is useful to evaluate general trends in the data to provide additional guidance on Cu_m limits within the framework of such a model. The most robust physical consideration is that Cu_m must remain at or above the equilibrium solubility limit of copper (Cu_e) in ferrite. The solubility limit has been examined with a number of techniques and is given by [Kenway-Jackson et al, 1993]

$$Cu_e(wt\%) = 120\exp[-5560/T\ (°K)] \quad (7\text{-}1)$$

Figure 7-1 compares Cu_e to Cu_m estimates for high copper CM alloys (CM11,12,18,19,20) from the VSR study based on the NUREG assessment method. The available data for 48 and 96h at 590°C, 24 and 48 h at 607°C, 12 and 24h at 624°C and 6 h at 641°C have been averaged in this plot (note data were not available for all materials for all these conditions). The general trend is for Cu_m to increase with T_{sr} at a small increment above Cu_e. The divergence between Cu_m and Cu_e increases with decreasing T_{sr}. The high nickel CM20 data fall above the others, while the intermediate nickel and alloys with 0.33 and 0.86% copper (CM11,12) copper fall near or slightly below Cu_e. The low and intermediate nickel alloys with Cu_{bk} ~ 0.42% lie in between. The dashed line, in the form of Equation 7-1, is a fit to the average (large plus symbols) of the high copper, intermediate nickel CM11 and CM19 data and is given by

$$Cu_m \sim 11.1\exp(-3282/T_{sr}) \quad (7\text{-}2)$$

Equation 7-2 represents a reasonable basis to estimate Cu_m for 'typical' high copper intermediate nickel RPV steels as a function of T_{sr}, assuming reasonably long t_{sr}. The stress relief time dependence of pre-precipitation can be crudely modeled in terms of standard equations for diffusion-controlled growth of precipitates [Porter and Easterling, 1987] as

$$Cu_m(t_{sr},T_{sr}) = Cu_m(AT)-[Cu_m(AT)-C_e(T_{sr})][1-\exp(k_{sr}t_{sr}^{3/2})] \quad (7\text{-}3)$$

Here $Cu_m(AT)$ is the Cu_m in the as-tempered (AT) condition and k_{sr} is a transformation rate coefficient that depends on the $Cu_m(AT)$, the copper thermal diffusion coefficient and the number density of the pre-precipitates. Thus, k_{sr} is also expected to depend on T_{sr} and $Cu_m(AT)$. The transformation rate coefficient is physically complex but is crudely modeled as

$$k_{sr} = \gamma_{sr}Cu_m(AT)\ Cu_{bk}\exp(-E_s/T) \quad (7\text{-}4)$$

where γ_{sr} is a numerical constant, and the Cu_{bk} term represents the effect of the bulk copper on the pre-precipitate number density (or nucleation rate) and E_s is an activation energy term that accounts for the combined effect of T_{sr} on copper diffusion and pre-precipitate number density.

Figure 7-2 compares the results for the high copper intermediate nickel CM alloys (C11,12,19) from the VSR study, using the NUREG-$\Delta\sigma_y$ model to assess Cu_m, to predictions using Equations. 7-1 through 7-4, with γ_{sr} = 1.33 x 10^9 and E_s =20,000°K. The resulting predicted Cu_m values for CM19 are in good agreement with the VSR estimates, while the CM12 results are more scattered and the CM11 values are lower by an average of about 0.05%. Figure 7-3 compares the corresponding predictions of Cu_m as a function of t_{sr} for CM19. The effects of the variation of k_{sr} with T_{sr} are small and less than the uncertainties in the data. Thus it is reasonable to use a constant value of k_{sr}, equal to that predicted for 590°C to model the average t_{sr} behavior of a typical high copper, intermediate nickel steel as

$$Cu_m(t_{sr},T_{sr})=Cu_m(AT)-[Cu_m(AT)-Cu_e(T_{sr})][1-\exp(-0.017t_{sr}^{3/2})] \quad (7\text{-}5)$$

Here $Cu_m(AT) = 0.35\%$ for $Cu_{bk} > 0.35\%$ and $Cu_m(AT) = Cu_{bk}$ for $Cu_e(T_{sr}) < Cu_{bk} < 0.35\%$.

At best Equation 7-5 can be used as a rule of thumb for assessing the effects of stress relief conditions on Cu_m in low to intermediate nickel steels. The Cu_e accounts for T_{sr} and the constant k_{sr} crudely accounts for the t_{sr} dependence. However, Equation 7-5 should not be extrapolated below about 590°C, because of slower diffusion rates, or above 640°C because reduced rates of pre-precipitate nucleation. Equation 7-5 is also not applicable to high nickel steels, where higher Cu_m are anticipated.

Verification and further refinement of the Cu_m model will require additional data and more detailed modeling.

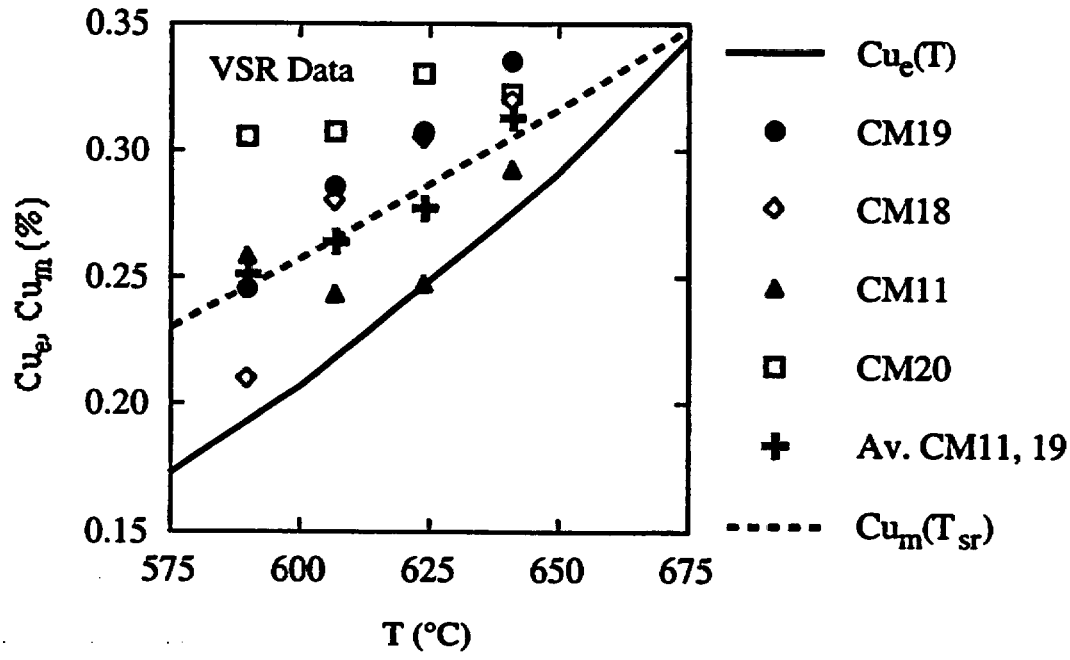

Figure 7-1 Comparison of Cu_e to Cu_m for high copper CM alloys from VSR

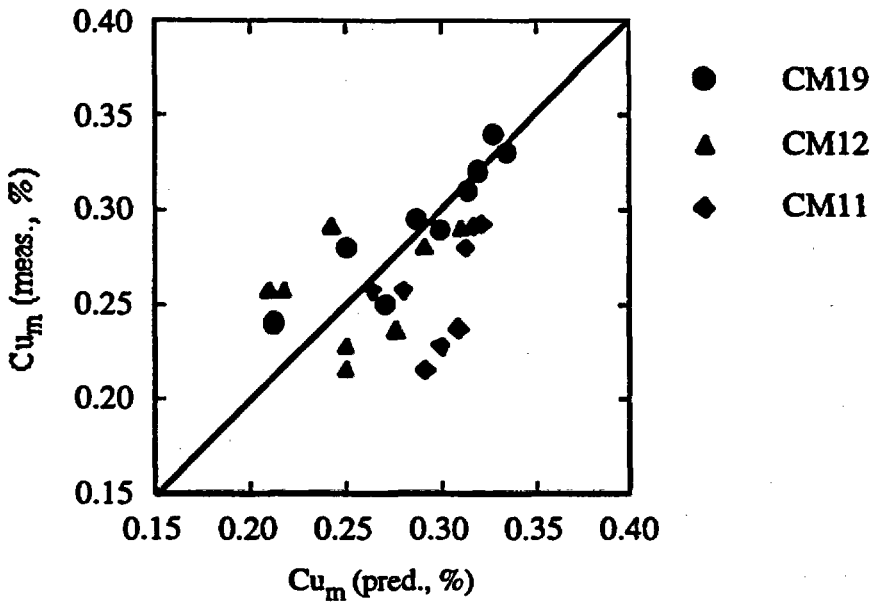

Figure 7-2 Comparison of Cu_m from VSR data to predictions of Equations 7-2 through 7-4.

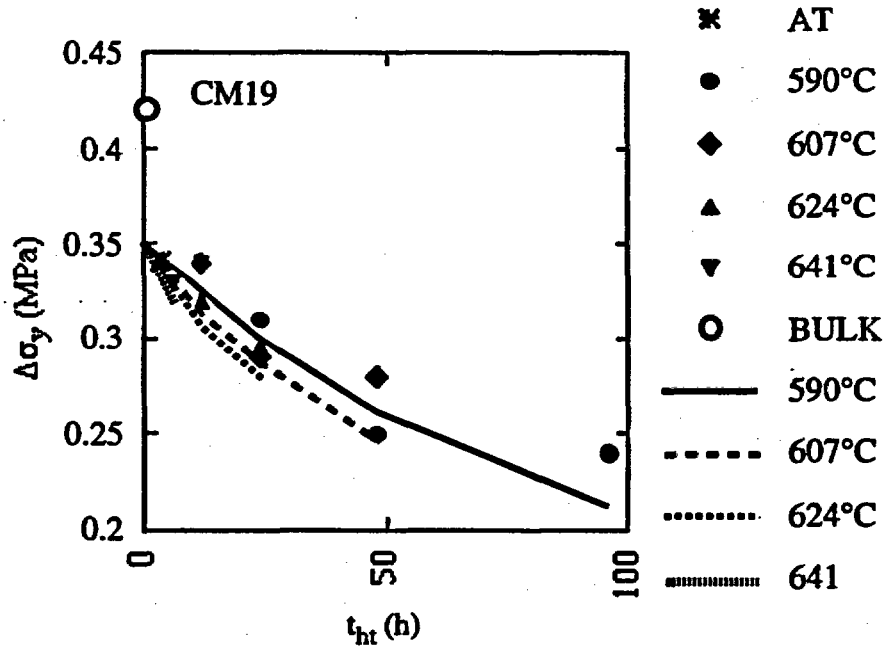

Figure 7-3 Comparison of Cu_m for CM19 as a function of t_{sr}.

8 SUMMARY AND CONCLUSIONS

This study is part of an overall effort to provide guidance and insight for supporting a technical basis for proposed changes to Reg Guide 1.99/Rev 2. The overall effort involves developing an independent embrittlement database from controlled, single-variable experiments. High-resolution experimental maps of the individual and interactive effects of metallurgical and environmental variables on embrittlement are derived from irradiation and post-irradiation testing of very large experimental matrices. These experiments take advantage of the relationship between ΔT and increases in yields stress ($\Delta\sigma_y$), which can be measured using small tensile specimens. These experiments achieve precise control and characterization of the embrittlement variables. Irradiations are carried out in the Irradiation Variable Facility (IVAR) at the University of Michigan Ford Research Reactor. The large experimental $\Delta\sigma_y$ database under development, will ultimately be complemented by an extensive effort to characterize the microstructural changes responsible for $\Delta\sigma_y$ and ΔT. The collective results will be analyzed and used to develop quantitative, mechanism-based embrittlement models. These in turn can be used to support the development and justification of statistical fits to the power reactor embrittlement database (PREDB), such as the Eason-Wright-Odette Model (NUREG/CR-6551) as a part of the technical basis for proposed changes to Reg Guide 1.99/2.

This report has focused on a subset of important questions that must be answered in establishing this technical basis. The effort involved analyzing irradiation hardening data from three irradiation experiments (T4, T14 and VSR) performed in the IVAR facility, and one irradiation experiment (PB) performed in a piggy back experiment.

Collectively, the T4, T14 and PB data permitted the systematic investigation of compositional effects. The sigmoidal dependence of hardening on copper was seen, as expected. The data also showed systematic increases of hardening with nickel, phosporous, and manganese. The sensitivity to copper was enhanced by nickel and the sensitivity to phosphorous was decreased by copper. The sensitivity to other chemical elements – boron, carbon, nitrogen, tramp elements – was small or negligible. The observed small sensitivity to molybdenum is consistent with a superposition of irradiation hardening to pre-existing hardening from strong obstacles like Mo_2C.

Data from these irradiations were compared to predictions of a $\Delta\sigma_y$ modification of a NUREG-ΔT correlation model. The overall agreement was quite remarkable. Thus the $\Delta\sigma_y$ database generated in this study provides a powerful and independent confirmation of the general form of the NUREG model treatment of copper, nickel and phosphorous and their interactions. All the major trends in both the NUREG model and in the IVAR database are consistent with current understanding of embrittlement mechanisms. Specifically, the data validate the general two-component form of the NUREG-ΔT model comprised of a copper-independent (matrix feature, matrix features) and copper-dependent (copper rich precipitate, CRP) terms, and corroborate the very strong interaction between copper and nickel in the NUREG model CRP contribution to ΔT. The data also validate the inclusion of phosphorous in the NUREG model, and support its approximate treatment in the matrix feature contribution to ΔT.

The VSR experiment permitted the investigation of the effect of systematic variations in stress relief time and temperature following the final tempering of several sets of A533B-type split melt alloys. These data demonstrated the systematic reduction of matrix copper, Cu_m, prior to irradiation by pre-precipitation. The pre-precipitation occurred to a greater extent with increasing stress relief time and with decreasing stress relief temperature. The irradiation hardening data

were complemented by FEGSTEM, resistivity and Seebeck coefficient measurements on unirradiated alloys subject to a range of stress relief anneals. In addition to verifying the effect of heat treatment on matrix copper, the emergence of resistivity and Seebeck coefficient measurements as useful nondestructive tools for assessing embrittlement potential were demonstrated. Together the data were used to develop a simple transformation model to estimate Cu_m as a function of stress relief time and temperature. In addition the data validate a maximum in Cu_m of around 0.3% following tempering and stress relief heat treatments found in the NUREG model. Strong support was also found for even lower Cu_m levels of about 0.25% in low-to-intermediate nickel steels, as well as evidence for corresponding levels in excess of 0.3% in high nickel steels.

The database and analysis provided in this report also provides additional insight into several other issues, which are further from closure. Resolution of these issues could lead to signif-icant improvements in embrittlement forecasting. They include:

1. Possible sources of product form variability and data scatter in the CRP term. These include embrittlement contribu-tions from elements not explicitly accounted for in the NUREG-DT model, like manganese (interacting with nickel and copper), and effects of microstructural variations on the fluence dependence of $\Delta\sigma_y$ and ΔT.

2. An unanticipated effect of flux and flux-composition interactions on the fluence dependence of the CRP contribution to $\Delta\sigma_y$ and ΔT.

3. Effects of the unirradiated constitutive and Charpy properties on: a) the $\Delta\sigma_y$ produced by a specified embrittlement microstructure; and b) the relationship between $\Delta\sigma_y$ and ΔT. This work has also identified new mechanisms that influence the effects the heat treatment on the unirradiated microstructure and properties, hence, also $\Delta\sigma_y$ and ΔT.

4. Possible sources of product form variability and data scatter in the matrix features term, including an increase in $\Delta\sigma_y$ with manganese and nickel.

5. A possible interaction reducing the effect of phosphorus at higher copper.

These will be addressed in ongoing research in the UCSB program.

9 REFERENCES

Arajs, S., F. C. Schwerer, R. M Fisher, "Residual Resistivities of Binary Iron Alloy," *Phys. Stat. Sol*, 33, 1969, pp.731-740.

Alexander, D. E., B. J. Kestel, P. R. Jemian, G. R. Odette, D. Klingensmith, D. Gragg, "Anomalous Small Angle X-ray Scattering Characterization of Model Pressure Vessel Alloy Microstructures," *MRS Soc. Symp. Proc.*, 540, 1999, p.415.

ASTM Standard Test Method for Resistivity of Electrical Conductor Materials, ASTM B193-87, *Annual Book of ASTM Standards*, American Society for Testing and Materials, Philadelphia, PA, 1987.

ASTM Standard Test Method for Determination of Reference Temperature T_o for Ferritic Steels in the Transition Range, ASTM 1921-97 *Annual Book of ASTM Standards 03.01*, American Society for Testing and Materials, West Conshohocken, PA, 1998, pp. 1068-1084.

Auger, P., P Parieje, M. Alcamatsu, J. C. Van Duysen, "Microstructural Characterization of Atom Clusters in Irradiated Pressure Vessel Steels and Model Alloys," *J. Nucl. Mater.*, 211, 1994, pp. 194-201.

Bolton, C., J. T. Buswell, R. B. Jones, R. Moskovic, R. H. Priest, "The Modeling of Irradiation Embrittlement in Submerged-Arc Welds," *ASTM STP 1270*, American Society for Testing and Materials, Philadelphia, PA, 1996, pp. 103-118.

Brillaud, C. and F. Hedin, "In Service Evaluation of French Pressurized Water Reactor Vessel Steel, ASTM-STP-1125, American Society for Testing and Materials, Philadelphia, PA, 1992.

Buswell, J. T. and R. B. Jones, "The Modeling of Radiation Hardening and Embrittlement in Magnox Mild Steel Submerged-Arc Welds, *ASTM STP 1175*, American Society for Testing and Materials, Philadelphia, PA, 1993, pp. 424-443.

Eason, E. D., J. E., Wright and G. R. Odette, "Improved Embrittlement Correlations for Reactor Pressure Vessel Steels," *NUREG/CR-6551*, U. S. Nuclear Regulatory Commission, Washington D.C., 1998.

English, C.A., W. J. Phythian and R. J. McElroy, "Microstructure and Modelling of RPV, Embrittlement," *Microstructure Evolution During Irradiation, MRS Symp.* 439, I. M. Robertson et al., eds., MRS, 1997, p. 471.

Fint, J., "A Study of the Evolution of Precipitates in Pressure Vessel Steels Using Small Angle Neutron Scattering," MS Thesis, UC Santa Barbara, 1990.

Fisher, S. B., J. E. Harbottle, N. Aldridge, *Phil. Trans. Roy. Soc. Lond*, A315, 1985, 301.

Fisher, S. B, and J. T. Buswell, "A Model for PWR Pressure Vessel Embrittlement," *Int. Journal of Pressure Vessels and Piping*, 27-2. 1987, pp. 91-135.

Foreman, A.J. E., and M. J. Makin, *Can. J. Phys.* 45, 1967, p. 511.

Guinier, A. and G. Fournet, *Small Angle Scattering of X-rays*, translated by C. B. Walker, John Wiley and Sons, New York, 1955.

Jenkins, M. L., "Characterization of Radiation Damage Microstructures by TEM," *J. Nuclear Materials*, 216, 1994, pp. 125-156.

Kenway-Jackson, A. J., J. Mace, R. N Thomas,. W. Phythian, *Technical Report AEA-RS 4411*, AEA Technology, Harwell, UK, 1993.

Kostorz, G., Small Angle Scattering and Its Applications to Materials Science," *Treatise on Materials Science and Technology*, 15.

Liu, C. L., G. R. Odette, B. D. Wirth, G. E. Lucas, "A Lattice Monte Carlo Simulation of Nanophase Compositions and Structures in Irradiated Pressure Vessel Fe-Cu-Ni-Mn-Si Steels," *Matls Sci and Eng.*, A238, 1997, pp. 202-209.

Lott, R. and P. D. Freyer, "Modeling of Irradiation Embrittlement and Annealing/Recovery in Pressure Vessel Steels," *ASTM STP 1270*, American Society for Testing and Materials, Philadelphia, PA, 1996, pp. 86-102.

Mader, E., "Kinetics of Irradiation Embrittlement and the Post-Irradiation Annealing of Nuclear Reactor Pressure Vessel Steels, Ph.D. Thesis, UC Santa Barbara, 1995.

Mathon, M-H., "Etude De La Precipitation Et Des Mechnismes Microscopiques De Durcissement Sous Irradiation Dans Des Alliages Ferritiques Dilues, *Report CEA-R-5701*, Commissariat A L'Engerie Atomique, Saclay, France, 1995

McElroy, R. J. and A. L. Lowe, "Irradiation Embrittlement Modeling of Linde 80 Welds, " *ASTM STP 1270*, American Society for Testing and Materials, Philadelphia, PA, 1996, pp. 68-85.

Miller, M. K., and M. G. Burke, "An APFIM Survey of Grain Boundary Segregation and Precipitation in Irradiated Pressure Vessel Steels," *ASTM STP 1175*, American Society for Testing and Materials, Philadelphia, PA, 1993, pp. 492-502.

Miller, M. K., P. Pareige, M. G. Burke, "Understanding Pressure Vessel Steels: An Atom Probe Perspective," *Materials Characterization*, 44, 2000, pp. 235-254.

Miloudi, S., S. Jumel, J.-F. Coste, J.-C. van Duysen, "Thermoelectric Power: Non-Destructive Method for Monitoring the Irradiation Effects in Ferritic Steels," in: *NDT Methods for Monitoring Degradation*, U. von Estorff, L. M. Davies, P. Trampus, eds, European Commission, Petten, The Netherlands, 1999, pp. 114-121.

Miloudi, S., S. Jumel, P. Pareige, J.-F. Coste, J.-C. Van Duysen, Thermoelectric Power: A Non-Destructive Method for Monitoring the Irradiation Effects in Ferritic Steels," *ASTM-STP-1366*, American Society for Testing and Materials, West Conshohocken, PA, 2000, pp.1029-1042.

Odette, G. R., "On the Dominant Mechanism of Irradiation Embrittlement in Pressure Vessel Steels," *Scripta Met.*, 11, 1983, p. 1183.

Odette, G. R., P. M. Lombrozo, R. A. Wullaert, "The relationship Between Irradiation Hardening and Embrittlement of Pressure Vessel Steels," *ASTM STP 870*, American Society for Testing and Materials, Philadelphia, PA, 1985, pp. 840-860.

Odette, G. R. and G. E. Lucas, "Recent Advances in Predicting Embrittlement of Reactor Pressure Vessel Steels," *Proceeding of the 2nd International Symposium on Environmental Degradation in Nuclear Reactors – Water Reactors*, J. T. A. Roberts, J. R. Weeks, G. J Theus, eds., American Nuclear Society, La Grange Park, IL, 1986, p. 345.

Odette, G. R. and G. E. Lucas "The Effect of Heat Treatment on Irradiation Harding of Pressure Vessel Steels," *Proceeding of the 3rd International Symposium on Environmental Degradation in Nuclear Reactors – Water Reactors*, J. R. Weeks, G. J Theus, eds, The Metallurgical Society, Warrendale, PA, 1988, p. 95.

Odette G. R and G. E. Lucas, "Irradiation Embrittlement of LWR Pressure Vessel Steels," *EPRI NP-6114* (1989).

Odette, G. R. and G. E. Lucas "The Effect of Nickel on Radiation Hardening of Pressure Vessel Steels," *ASTM-STP-1046*, Vol. II,

American Society for Testing and Materials, 1990, p.323.

Odette, G. R., Mader, E., Lucas, G. E., Phythian, W. J., English, C. A., "The Effect of Flux on Irradiation Hardening of Pressure Vessel Steels," Proceedings of the 16th Symposium on the Effects of Irradiation on Materials, *ASTM-STP-1175*, American Society for Testing and Mateials, Philadelphia, PA (1993) 373-393.

Odette, G. R., "Radiation Induced Microstructural Evolution in Reactor Pressure Vessel Steels," *MRS Soc. Symposium Proceedings*, 373, 1995, p.137.

Odette, G. R. and G. E. Lucas, "An Integrated Approach to Evaluating the Fracture Toughness of Irradiated Nuclear Reactor Pressure Vessels," *J. Non-Destrucive Eval.*, 14, 3/4 (1996) 137-150.

Odette, G. R. and G. E. Lucas, "Current Understanding of the Effects of Environmental and Irradiation Variables on RPV Embrittlement", *Proceedings of the 24th Water Reactor Safety Meeting*, 2, NUREG/CR-0157-2, 1997, p. 1.

Odette, G. R. and B. D. Wirth, "A Computational Microscopy Study of Nanostructural Evolution in Irradiated Pressure Vessel Steels, *J. Nucl. Mater.*, 251, 1997, pp. 157-171.

Odette, G. R. and G. E. Lucas, "Recent Progress in Understanding Reactor Pressure Vessel Steel Embrittlement," *Radiation Effects and Defects in Solids*, 144, 1998, pp. 189-231.

Odette, G. R., "Modeling Irradiation Embrittlement in Reactor Pressure Vessel Steels," *Neutron Irradiation Effects in Reactor Pressure Vessel Steels and Weldments*, IAEA-IWG-LMNPP-98/3, M. Davies, ed., IAEA, Vienna, 1998.

Odette, G. R. and G. E. Lucas, "Reactor Pressure Vessel Embrittlement: The Road Ahead," *Proc. Water Reactor Safety Meeting*, October, 1999, U.S. NRC.

Odette, G. R., G. E. Lucas, D. Klingensmith, "Anomalous Hardening in Model Alloys and Steels Thermally Aged at 290°C and 350°C: Implications to Low Flux Irradiation Embrittlement," Effects of Radiation on Materials: 18th International Symposium, *ASTM-STP-1325*, American Society for Testing and Materials, 1999, pp.88-101.

Odette, G. R. and M. He, "Physical Model for the Master Curve Shape," *Applications of Fracture Mechanics in Failure Assessment*, PVP-412, D. Lidbury et al., eds. PVP-ASME, 2000, p. 93.

Odette, G. R. and M. He, "A Cleavage Toughness Master Curve Model," *J. Mucl. Mater.*, 283-287, 2000, pp. 120-127.

Pareige, P., "Etude A La Sonde Atomique De L'Evolution Microstructurale Sous Irradiation D'Alliages Ferritiques FeCu Et D'Aciers De Cuve De Reacteurs Nuclearies," Ph.D. Thesis, LeUniversite de Rouen, 1994.

Phythian, W. and C. A. English, "Microstructural Evolution in Reactor Pressure Vessel Steels," *J. Nucl. Mater.*, 205, 1993, p.162.

Pollock, D. D., *Thermocouples, Theory and Properties*, CRC Press, Ann Arbor, 1991.

Porter, D. A., and K. E. Easterling, *Phase Transformations in Metals and Alloys*, Van Nostrand Reinhold, Berkshire, UK, 1987.

Remec, I, "Preliminary Fast Neutron Flux Results for the UCSB Irradiation Facility Characterization Experiment," ORNL Internal Report, July 24, 1997.

Remec, I., C. A. Baldwin, F.B.K. Kam, "Neutron Exposure Parameters fof Capsule 10.05 in the Heavy-Section Steel Irradiation Program Tenth Irradiation Series," NUREG/CR-6600, U. S. Nuclear Regulatory Commission, 1998.

Rossiter, P. L., *The Electrical Resistivity of Metals and Alloys*, Cambridge University Press, Cambridge, UK, 1991.

Sokolov, M. A, S. Spooner, G. R. Odette, B. D. Wirth, G. E. Lucas, "SANS Study of High Copper RPV Welds in Irradiated and Annealed Conditions," Effects of Radiation on Materials: 18th Int'l Symp., *ASTM STP 1325*, American Society for Testing and Materials, 1999, pp. 333-345.

Solt, G., F. Frisius, W. B. Waeber, P. Tipping, *Proceedings of the 5th Inteanational Symposium on Environmental Degradation of Materials in Nuclear Power Systems – Water Reactors*, D. Cubicciott, E. Simonen, R. Gold (eds), American Nuclear Society, La Grange Park, IL, 1990, p. 444.

Solt, G., F. Frisius, W.B. Waeber, P. Tipping, *ASTM STP 1175*, American Society for Testing and Materials, West Conshohocken, PA, 1993, pp. 444-462.

Stallmann, F. W., J. A. Wang, F. B. K. Kam, B. J Taylor, "PR-EDB: Power Reactor Embrittlement Data Base, Version 2," *NUREG/CR-4816*, U. S. Nuclear Regulatory Commission, 1994.

Stoller, R., "Pressure Vessel Embrittlement Predictions Based on a Composite Model of Copper Precipitation and Point Defect Clustering, *ASTM STP 1270*, American Society for Testing and Materials, West Conshohocken, PA, 1996, pp. 25-58.

Williams, T. J., P. R. Burch, C. A. English, and P. H. N de la Cour Ray, "The Effects of Dose Rate and Temperature and Copper and Nickel Content on the Irradiation Shift of Low Ally Submerged-Arc Welds," *Proceedings of the 3rd International Symposium on Environmental Degradation of Materials in Nuclear Power Systems – Water Reactors*, J. R. Weeks, G. J Theus, eds, The Metallurgical Society, Warrendale, PA, 1988, p. 121.

Williams, T. J., and W. J. Phythian, "Electron Microscopy and Small Angle Neutron Scattering Study of Precipitates in Low-Alloy Submerged Arc Welds," *ASTM STP 1270*, American Society for Testing and Materials, Philadelphia, PA, 1996, p. 191.

Wirth, B. D., "On the Character of Nano-Scale Features in Reactor Pressure Vessel Steels Under Neutron Irradiation," Ph.D. Thesis, University of California, Santa Barbara, 1998.

Wirth, B. D., G. R. Odette, W. Pavinich, G. E. Lucas, S. Spooner, "Small Angle Neutron Scattering Study of Linde 80 RPV Welds," *ASTM STP 1325*, American Society for Testing and Materials, 1999, pp.102-124.

Wirth, B. D., and G. R. Odette, "Kinetic Lattice Monte Carlo Simulations of Cascade Aging in Dilute Iron-Copper Alloys, *MRS Symp. Proc.*, 540, 1999, pp. 637-642.

USNRC, *Rules and Regulations Title 10 Code of Federal Regulations Part 50 Fracture Toughness Requirement*, United States Nuclear Regulatory Commission, U. S. Government Printing Office, Washington, 1986.

USNRC, *Regulatory Guide 1.99: Radiation Embrittlement to Reactor Vessel Materials*, United States Nuclear Regulatory Commission, U. S. Government Printing Office, Washington, D.C., 1988.

Appendix A The NUREG $\Delta\sigma_y$ Model

A comprehensive effort to develop improved embrittlement prediction models was reported in NUREG/CR-6551 published in 1998 [Eason et al, 1998]. Statistical equations were least squares fit to the scrubbed Charpy V-notch test energy-temperature data extracted from power reactor embrittlement (surveillance) data base (PREDB). Embrittlement equations were developed for both reductions in upper shelf energy and increases in the 41J transition temperature (ΔT). The latter were based on 609 ΔT points in the PREDB. The NUREG-ΔT models contain two terms. The first is attributed to what is called in this report the matrix feature contribution, which occurs in steels independent of their copper (and nickel) content. The matrix features term depends on phosphorous, irradiation temperature (T_i) and fluence (ϕt). The second term derives from what is called the CRP contribution in this report. The NUREG CRP term depends on copper, nickel, ϕt and flux (ϕ) or irradiation time ($\phi t/\phi$).

The most salient features of the NUREG ΔT models were that: a) the correlation equations were based on an understanding of key embrittlement mechanisms; b) selection from among a large number of statistically similar calibrated correlation equations was based on both mechanistic considerations and consistency with independent sources of data, largely derived from UCSB test reactor studies preceding the IVAR program, including data from the PB capsule; c) unless there was a combination of mechanistic and statistical significance dictating otherwise, the correlation equations were kept as simple and with as few degrees of freedom as possible.

Improvements in the NUREG model have continued and currently focus on the following questions and issues:

a. The treatment of phosphorous in the matrix feature term.

b. The effective maximum copper content as influenced by variables such as product form and nickel.

c. Variability in the embrittlement model coefficients associated with product form, including subclasses representing a vendor effect.

d. The effects of flux-time in the CRP term associated with possible thermal diffusion contributions to precipitation kinetics, primarily impacting very low flux service conditions characteristic of BWRs.

e. An additional possible non-conservative bias in ΔT at times in excess of about 10^5h that cannot be attributed to a particular mechanism or combination of other variables (although this effect increases slightly with increasing T_i.)

While not a major issue of contention, it remains important to evaluate the general forms and variable dependence of both the matrix features and CRP, since some details of the correlation depend on all others. Thus a major objective of this study has been to compare the IVAR data trends with predictions of the NUREG model.

Such comparisons require conversion of the ΔT predictions to corresponding values of $\Delta\sigma_y$. A strong empirical relation between ΔT and $\Delta\sigma_y$ has been observed in almost all cases where both types of data are available in cases where non-hardening temper embrittlement, associated with intergranular fracture does not play a role [Odette et al, 1985]. However, the empirical hardening Charpy shift factor, $C_c = \Delta T/\Delta\sigma_y$, varies in a typical range of about 0.65 ± 0.15 °C/MPa. The ΔT-$\Delta\sigma_y$ relation should also be consistent with the micromechanics of cleavage fracture.

A quantitative micromechanics model of C_c has been developed [Odette et al, 1985]. The model includes treatment of both: a) $\Delta\sigma_y$ induced shifts in the maximum temperature (T_c) for cleavage preceding general yield (which occurs at a Charpy energy of about 10J); and b) the layover in the Charpy energy-temperature curve in the transition that is be related to the decrease in the upper shelf energy (ΔUSE) that can also be related empirically to $\Delta\sigma_y$. As a consequence of the temperature-dependence of σ_y and the contribution of the USE drop to the 41 J ΔT, C_c depends on the unirradiated Charpy properties (T_{cu} and USE_u) and $\Delta\sigma_y$. Thus this model explains part of the observed variability of C_c.

The NUREG-ΔT model does not explicitly account for the variations in C_c due to differences in unirradiated T_{cu} and USE_u. However, it does implicitly account for $\Delta\sigma_y$. Thus the average of values in the T_{cu} and USE_u in the NUREG PREDB were used in the model to determine an average relation between ΔT(°C) and $\Delta\sigma_y$(MPa). The results can be fit to a convenient analytical form

$$C_c(\Delta T) = \Delta T/\Delta\sigma_y \qquad \text{(A-1)}$$

Where $\Delta\sigma_y \sim 6.59\times10^{-6}\Delta T^3 - 4.67\times10^{-3}*\Delta T^2+1.78*\Delta T+3.432$

Figure A-1 shows that C_c increases significantly with increasing ΔT (and $\Delta\sigma_y$). However, while such tends have been observed, the quantitative relationship has not been fully verified by experiment, particularly at high $\Delta\sigma_y$ and $C_c > 0.8$. Further, within data scatter an average value of $C_c = 0.7$ is a reasonable approximation to relate to $\Delta\sigma_y \sim \Delta T/C_c$: Thus three options were used to convert the NUREG-ΔT to $\Delta\sigma_y$, including: a) Equation A-1; b) Equation A-1 up to a maximum $C_{cmax} = 0.8$; c) an average constant $C_{cav} = 0.7$.

The NUREG-ΔT model is given by

$$\Delta T = \Delta T_{mf} + \Delta T_{crp} \qquad \text{(A-2a)}$$

where

$$\Delta T_{mf} = A\exp\{1.91\times10^4/(T_{i'}+460)\}(1+57.7P)\phi t^{[0.445-\log(\phi t)]}$$

$$\Delta T_{crp} = B(1+2.56Ni^{1.358})h(Cu)g(t) \qquad \text{(A-2b)}$$

and

$$h = 0, \text{ for } Cu \le 0.072\%, \qquad \text{(A-2c)}$$

$$h = (Cu - 0.072)^{0.678} \text{ for } 0.072 < Cu < 0.3\%$$

$$h = 0.367 \text{ for } Cu \ge 0.3\%$$

$$g(\phi t) = 0.5 + 0.5\tanh[(\log\phi t - 18.29)/0.6] \qquad \text{(A-2d)}$$

The $T_{i'}$ is in °F and the $g(\phi t)$ ignores a small contribution from irradiation time that is not pertinent to assessing the test reactor data in this report. The corresponding $\Delta\sigma_y$ were determined as $\Delta\sigma_y = \Delta T/C_c$, based on one of the three options listed above.

The NUREG-$\Delta\sigma_y$ model was used in analyzing the IVAR data. In all cases the A and B parameters for welds from the NUREG model were used since this choice provided the best results and welds cover the widest range of copper and nickel in the PREDB. The analysis involved:

1. Adjusting $\Delta\sigma_y$ for the LH and LI (~ 0.74%) alloys to account for small differences in nickel compared to the high copper LV and CM alloys (~ 0.83±0.03%). This was done by adding the NUREG predictions of $\Delta\sigma_y$(Ni for LV or CM) - $\Delta\sigma_y$(Ni = 0.74%) to the experimental $\Delta\sigma_y$ using the set of other pertinent variables. This small adjustment, of order 10-15 MPa, was based on the basic NUREG model and use of option b above for C_c.

2. Comparison of the $\Delta\sigma_y$ predicted by the NUREG model for the specified alloy

chemistry, irradiation temperature and fluence to the corresponding experimental data from the T14 capsule. Flux was not explicitly considered in this comparison, and option b above for C_c provided the best results.

3. Comparing the $\Delta\sigma_y$ predictions of the NUREG model (the matrix feature term) to the corresponding data for low copper CM steels from a number of IVAR capsules for low (0.005%) and high (0.040%) nominal phosphorous contents. This used the base model and option b for C_c.

4. Evaluating Cu_m from the $\Delta\sigma_y$ data from the VSR study. The VSR data are from a high flux capsule. Although not the focus of this report, other IVAR data show that higher flux shifts the $\Delta\sigma_y(\phi t)$ CRP contribution for a particular alloy to higher fluence. Thus the NUREG model was modified to account for the effect of flux. The approach was based on analysis of the data from the high flux T4 capsule. A number of modified NUREG models were tried to find a plausible treatment of flux that provided a good fit to these data. It was found that a very good fit could be achieved by using option c for C_c above, and a flux factor ($f_\phi \leq 1$) to reduce the actual fluence to an effective fluence at high flux. Further, it was found that fitting required a f_ϕ that decreased with increasing alloy nickel content. This behavior is consistent with higher rates of interstitial recombination with vacancies trapped on nickel solutes. The fit provided by $f_\phi = 1/(1+1.3Ni)$ is shown as the filled circles in Figure A-2 comparing the $\Delta\sigma_y$ predicted by the modified NUREG model with the data from the T4 capsule. The unfilled circles are the corresponding results for $f_\phi = 1$. The need to account for nickel is illustrated in Figure A-3. Here the differences between the predicted and measured $\Delta\sigma_y$ are plotted against nickel for the T4 capsule steels with more than 0.072% copper. Data for the low manganese and highest copper alloys and one weld (67W) with a large inexplicable discrepancy are not included in this plot, since they are not representative of the other IVAR or the PREDB data trends (note the low manganese result is consistent with the lower sensitivity of forgings in the PREDB). The discrepancy between the $\Delta\sigma_y$ predictions of a flux independent NUREG model and experiment increases with increasing nickel. This trend demonstrates the need for a nickel-dependent f_ϕ in the modified NUREG model. However, it should be emphasized that the $f_\phi(Ni)$ modification does not represent a quantitative flux model. Rather, it represents an attempt to calibrate the modified NUREG model to estimate relative values of Cu_m using data from the VSR study.

Application of the modified NUREG-model is straightforward. The specific nickel and phosphorous contents along with the VSR irradiation temperature and fluence are used to compute $\Delta\sigma_y$ using the modified NUREG model as a function of copper. The copper that gives the predicted $\Delta\sigma_y$ equal to the measured value is taken as Cu_m.

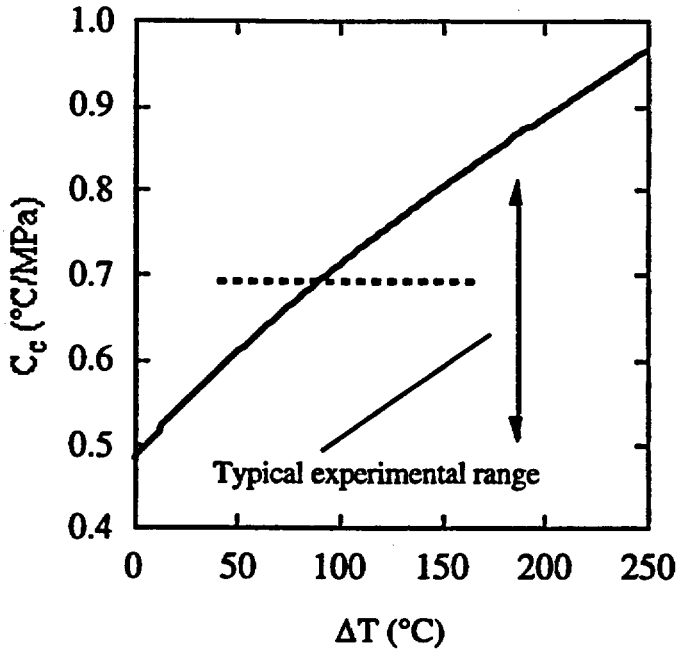

Figure A-1 Variation of C_c with ΔT. The dashed line shows the average.

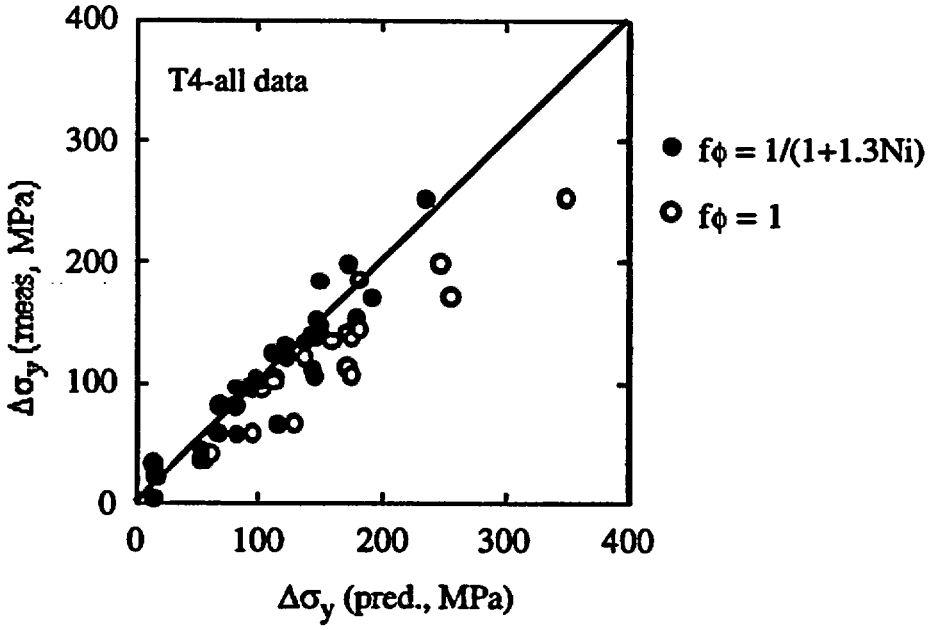

Figure A-2 Comparison measured $\Delta\sigma_y$ with values predicted from NUREG model for T4.

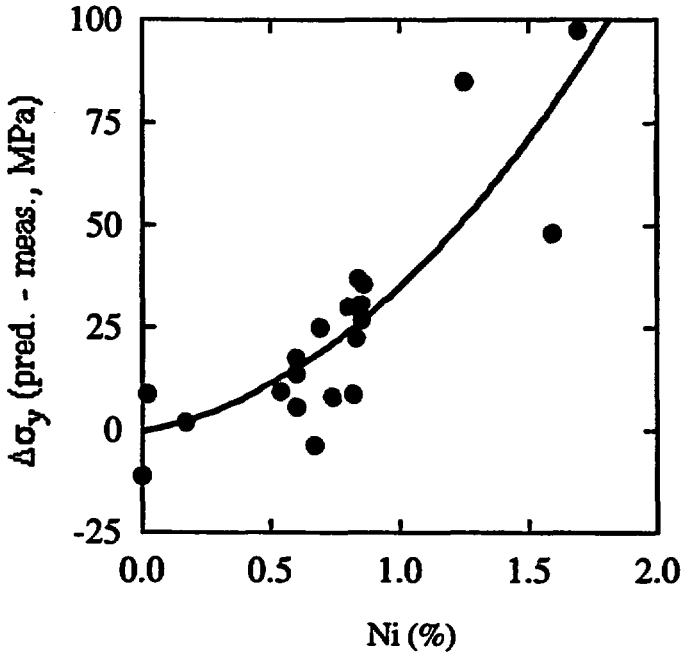

Figure A-3 Variation of the difference between predicted and measured $\Delta\sigma_y$ with Ni.

APPENDIX B TENSILE DATA FOR T4, T14, VSR AND PB

Table T4. Data for Capsule T4

Alloy	Baseline σ_y MPa	$\pm\sigma_y$ MPa	Irradiated σ_y MPa	$\pm\sigma_y$ MPa	$\Delta\sigma_y$ MPa	$\pm\Delta\sigma_y$ MPa	Baseline uts MPa	±uts MPa	Irradiated uts MPa	±uts MPa	Δuts MPa	±Δuts MPa
CM3	428	12	433	14	5	18	531	16	523	12	-8	20
CM10	429	11	452	10	23	15	520	15	537	13	17	20
CM11	438	6	587	12	149	13	527	11	658	10	131	15
CM13	424	11	464	4	40	12	512	17	540	8	28	19
CM15	433	5	478	7	45	9	516	8	549	13	33	16
CM16	434	14	558	9	124	17	523	16	635	8	112	18
CM17	451	9	650	3	199	10	548	14	718	8	170	16
CM18	433	8	492	7	59	11	521	15	564	5	43	16
CM19	450	4	602	7	152	8	545	11	666	10	121	15
CM20	464	11	716	7	252	13	561	19	784	11	223	22
CM21	398	8	505	9	107	12	464	11	550	7	86	13
CM22 (series a)	406	7	545	6	139	9	482	6	598	3	116	7
CM22 (series b)	446	6	575		129	6	515	7	622		107	7
LA	469	6	549	13	80	15	583	6	656	10	73	12
LB	483	9	563	11	80	14	590	7	667	4	77	8
LC	491	4	636	3	145	5	609	4	745	6	136	7
LD	501	3	671	5	170	6	633	3	791	1	0	3
LG	493	7	526	6	33	9	609	6	637	6	28	9
LH	507	4	544	1	37	4	616	2	650	1	34	2
LI	512	6	617	11	105	12	628	7	719	11	91	13
LJ	530	12	671	1	141	12	641	4	758	1	117	4
LK	551	8	663	3	112	8	644	6	746	5	102	8
LO	527	9	712	2	185	9	638	8	808	1	170	8
ORNL 73 weld	507	13	639	6	132	14	610	12	726	6	116	13
EPRI C weld	536	5	656	3	120	6	626	8	731	5	105	9
B.W. weld 62	526	8	620	4	94	9	627	8	700	1	73	8
B.W. weld 63	497	7	632	0	135	7	598	5	716	3	118	6
B.W. weld 65	473	7	573	8	100	11	575	6	661	6	86	8
B.W. weld 67	514	16	581	6	67	17	606	15	663	4	57	15
ORNL A302b	557	18	580	4	23	18	690	19	714	0	24	19
ORNL HSST02 plate	473	4	570	10	97	11	619	4	700	4	81	6
JRQ plate	484	8	543	1	59	8	601	10	657	1	55	10

u = undertermined

Data for Capsule T14

Alloy	Baseline		Irradiated				Baseline		Irradiated			
	σ_y MPa	$\pm\sigma_y$ MPa	σ_y MPa	$\pm\sigma_y$ MPa	$\Delta\sigma_y$ MPa	$\pm\Delta\sigma_y$ MPa	uts MPa	±uts MPa	uts MPa	±uts MPa	Δuts MPa	±Δuts MPa
CM1	419	8	416	8	-3	12	497	9	480	17	-17	19
CM2	436	9	472	4	36	10	527	15	552	1	25	15
CM3	428	12	434	10	6	16	531	16	575	13	-10	21
CM4	458	13	490	5	32	14	559	13	575	3	16	13
CM5	394	21	453	9	62	24	488	18	566	8	0	20
CM6	453	9	476	21	23	22	552	8	559	27	7	28
CM7	457	17	502	16	45	24	566	20	606	12	40	12
CM8	400	6	393	11	-8	12	478	9	472	11	-7	14
CM9	416	5	427	0	11	5	499	15	505	10	6	18
CM10	429	11	455	1	26	11	520	15	538	4	18	15
CM11	438	6	610	4	172	7	527	11	718	5	152	12
CM12	496	9	634	6	138	11	590	12	711	8	121	15
CM13	421	2	483	10	62	10	507	17	534	27	27	17
CM14	429	14	492	11	63	18	526	15	585	13	59	20
CM15	434	13	476	6	42	14	523	16	549	9	26	18
CM16	434	13	582	4	148	14	523	16	651	6	128	17
CM17	451	9	676	5	225	10	548	14	739	4	191	15
CM18	433	8	496	3	63	9	521	15	568	7	47	16
CM19	450	4	621	1	171	4	545	11	690	5	145	12
CM20	464	11	736	6	272	12	561	19	799	8	238	21
CM21	398	8	513	6	113	10	464	11	564	7	97	13
CM22(set1)	406	7	562	5	156	9	482	6	617	5	135	8
CM22(set2)	446	6	591	u	145	6	515	7	649	u	134	7
CM 23	404	3	416	6	12	7	479	4	486	5	7	6
CM24	463	13	481	1	18	13	599	23	611	8	12	25
CM25	443	6	462	2	19	6	532	13	545	25	13	28
CM26	444	6	456	19	12	20	529	9	537	18	8	20
CM27(set1)	445	5	447	u	2	5	537	8	529	u	-8	8
CM27(set2)	438	14	435	u	-3	14	529	18	523	u	-12	18
CM28	448	10	634	1	186	10	538	8	696	0	158	8
CM29	265	7	343	2	78	7	379	12	434	4	55	13
CM30	481	9	619	5	138	10	579	11	698	6	119	13
CM31	444	6	442	1	-3	6	514	8	512	8	1	8
LA	469	6	549	8	80	10	583	6	657	6	74	9
LB	483	9	577	8	94	12	590	7	677	7	87	10
LC	491	4	660	4	169	6	609	4	764	2	155	5
LD	501	3	701	1	200	3	633	3	810	2	177	3
LG	493	7	528	3	35	7	609	6	636	2	27	6
LH	507	4	553	1	46	4	616	2	658	1	42	2
LI	512	10	619	8	107	13	628	6	721	5	93	8
LJ	530	12	684	4	154	13	641	4	773	4	132	6
LK	551	8	680	8	129	11	644	6	763	12	119	13
LO	527	9	709	1	182	9	638	8	811	1	173	8

T14 – cont'd

	Baseline		Irradiated				Baseline		Irradiated			
	σ_y MPa	$\pm\sigma_y$ MPa	σ_y MPa	$\pm\sigma_y$ MPa	$\Delta\sigma_y$ MPa	$\pm\Delta\sigma_y$ MPa	uts MPa	±uts MPa	uts MPa	±uts MPa	Δuts MPa	±Δuts MPa
ORNL 73 Weld	507	13	654	7	147	15	610	12	737	5	127	13
EPRI C weld	537	6	674	2	137	6	631	6	749	2	118	6
B.W. A weld	514	15	620	1	106	15	610	10	702	1	92	10
B.W. B weld	510	11	625	6	115	12	611	6	711	5	100	8
B.W. C weld	470	6	509	7	39	9	572	6	603	1	31	6
B.W. weld 62	526	8	624	2	98	8	627	8	705	4	78	9
B.W. weld 63	497	7	642	4	145	8	598	5	722	1	124	5
B.W. weld 65	473	7	568	7	95	10	575	6	631	4	56	7
B.W. weld 67	514	16	593	21	79	26	606	15	675	15	69	21
Rolls Royce Weld WV	462	8	761	2	299	8	559	8	829	6	270	10
Rolls Royce Weld WG	422	6	583	12	161	14	533	8	675	13	142	15
Rolls Royce Weld WP	472	3	514	3	42	4	571	3	608	2	37	3
ORNL Midland Weld	522	8	641	4	119	9	623	9	723	5	99	10
ORNL A302b	557	18	599	6	42	19	690	19	723	8	33	21
ORNL HSST02 plate	473	4	586	10	113	11	619	4	714	8	95	9
B.W. A508 plate	418	8	447	5	29	9	573	9	591	3	18	9

u = undertermined

Data for Capsule PB

Alloy	Baseline σ_y MPa	$\pm\sigma_y$ MPa	Irradiated σ_y MPa	$\pm\sigma_y$ MPa	$\Delta\sigma_y$ MPa	$\pm\Delta\sigma_y$ MPa	Baseline uts MPa	$\pm$uts MPa	Irradiated uts MPa	$\pm$uts MPa	Δuts MPa	$\pm\Delta$uts MPa
CM1-as tempered	451	8	464	2	13	8	521	4	538	1	17	4
CM2-as tempered	477	8	540	6	63	10	558	11	632	0	75	11
CM3-as tempered	447	7	481	20	34	21	535	8	569	26	35	27
CM4-as tempered	533	8	600	4	67	9	635	15	686	4	51	15.5
CM5-as tempered	493	27	573	8	80	28	585	32	671	10	86	33.5
CM6-as tempered	541	14	590	4	49	15	632	19	681	2	49	19.1
CM7-as tempered	486	16	587	9	101	18	589	9	693	6	103	10.8
CM8-as tempered	434	14	450	21	16	25	521	15	532	18	12	24
CM9-as tempered	450	1	462	9	12	9	530	6	536	7	6	9
CM10-as tempered	460	6	499	8	40	10	545	6	582	4	37	7
CM11-as tempered	480	4	667	2	187	5	580	4	749	6	169	7
CM12-as tempered	505	5	714	32	208	14	589	4	802	10	213	11
CM13-as tempered	474	3	515	5	41	6	560	5	591	5	31	7
CM14-as tempered	476	18	561	8	86	20	566	28	653	8	87	29
CM15-as tempered	477	8	530	4	52	9	546	10	601	2	54	10
CM16-as tempered	477	4	613	1	136	4	561	5	685	1	125	5
CM17-as tempered	497	8	726	5	228	10	591	7	808	1	217	7
CM18-as tempered	464	4	566	5	102	6	542	4	638	11	96	11
CM19-as tempered	490	16	698	10	205	19	590	24	787	15	197	29
CM20-as tempered	478	11	769	6	291	12	588	10	866	1	277	10
CM21-as tempered	454	6	563	3	109	7	516	6	620	1	104	6
CM22-as tempered	480	4	651	1	171	4	543	7	704	1	161	7
CM23-as tempered	412	13	410	3	-2	13	492	12	490	6	-2	14
CM24-as tempered	496	12	525	u	29	u	619	23	664	u	45	u
CM25-as tempered	475	5	513	5	38	7	563	19	594	8	32	21
CM26-as tempered	471	16	498	4	27	17	572	21	585	5	12	22
CM27-as tempered	488	17	499	34	11	38	571	19	581	28	10	34
CM28-as tempered	498	12	701	16	203	20	587	18	776	19	189	26
CM29-as tempered	315	7	394	25	79	26	430	5	486	26	56	27
CM30-as tempered	498	18	636	20	138	27	591	28	696	10	105	30
CM31-as tempered	472	11	505	10	33	15	556	15	586	15	30	21
alternate heat treatments												
CM5* aged 480°100hr/a.c	519	17	539	35	20	39	639	20	640	46	1	50
CM8* 400°C s.q.(not 450°)	422	33	439	15	18	36	504	18	510	15	6	23
CM12* s.r. 600° 8hr/ a.c.	499	8	682	5	183	9	591	17	749	10	158	20
CM18* s.r 600° 40hr/ a.c.	437	20	522	3	85	20	518	6	583	1	65	6
CM19* s.r. 600° 8hr/ a.c.	476	6	667	15	191	16	572	10	741	6	169	12
CM19* s.r. 600° 40hr/ a.c.	463	12	653	4	190	13	554	25	727	0	173	25
CM19* s.r. 600° 80hr/ a.c.	464	21	637	5	173	22	566	25	713	10	147	27
CM19* 500°C s.q.(not 450°)	495	12	694	6	200	14	601	11	775	11	174	16
CM20* s.r. 600° 40hr/ a.c.	467	5	773	9	306	11	550	4	842	16	292	17
CM20*500°C s.q.(not 450°)	507	25	823	3	316	25	609	33	908	11	299	35
CM23* 400°C s.q.(not 450°)	425	12	448	37	23	39	503	14	522	35	19	38
CM26* aged 480°100hr/a.c.	490	3	487	26	-3	26	592	9	581	42	-12	43

PB cont'd

Alloy	Baseline σ_y MPa	$\pm\sigma_y$ MPa	Irradiated σ_y MPa	$\pm\sigma_y$ MPa	$\Delta\sigma_y$ MPa	$\pm\Delta\sigma_y$ MPa	Baseline uts MPa	±uts MPa	Irradiated uts MPa	±uts MPa	Δuts MPa	±Δuts MPa
LA	462	10	534	0	71	10	579	8	643	1	64	8
LB	484	6	569	5	86	7	600	4	689	4	90	6
LD	513	2	729	0	216	2	649	7	840	0	191	7
LG	493	10	529	29	36	31	613	16	654	19	41	25
LH	498	8	558	2	59	9	620	13	665	0	45	13
LI	497	8	623	4	125	9	615	5	723	4	108	6
LJ	527	12	683	3	156	12	641	14	775	2	134	14
LK	537	13	667	u	130	u	644	8	762	u	118	8
LO	497	10	719	3	223	11	613	10	827	3	214	11
VA	154	15	196	20	42	25	217	13	230	26	14	29
VB	158	17	260	17	102	24	215	12	325	16	110	20
VC	152	2	222	43	70	43	204	16	257	38	54	41
VD	216	6	522	3	306	7	310	7	579	2	268	7
VE	220	3	428	3	208	4	322	5	489	1	167	5
VG	174	7	348	6	175	9	257	10	390	1	134	10
VH	175	12	393	4	218	13	252	14	444	4	192	15
VI	176	15	351	2	175	15	261	22	412	1	151	22
VJ	179	8	397	17	218	18	257	10	447	10	190	14
VK	226	5	259	4	33	6	289	8	299	4	10	9
VL	154	11	178	19	24	22	269	2	283	9	14	9
VM	207	7	356	5	149	9	277	19	400	1	123	19
VN	214	17	430	4	217	18	312	9	493	1	181	9
VO	240	10	464	11	225	15	332	11	523	3	192	12
VP	196	14	443	14	247	20	327	21	515	7	187	22
VR	169	3	321	1	152	3	272	5	376	7	104	9
VS	218	6	536	8	318	10	304	5	582	14	278	15
VT	223	7	443	3	219	8	343	14	520	2	176	14
VV	181	13	220	1	39	13	240	7	258	3	18	8
VW	209	7	245	1	36	7	271	9	287	9	16	13

U = undetermined

Data for VSR Capsule

		Baseline		Irradiated				Baseline		Irradiated			
Alloy	SR	σ_y MPa	$\pm\sigma_y$ MPa	σ_y MPa	$\pm\sigma_y$ MPa	$\Delta\sigma_y$ MPa	$\pm\Delta\sigma_y$ MPa	uts MPa	±uts MPa	uts MPa	±uts MPa	Δuts MPa	±Δuts MPa
CM3	590°C/24h	447	4	457	1	10	4	537	8	540	6	3	10
CM3	590°C/48h	414	23	445	21	31	31	495	24	517	29	22	38
CM3	590°C/96h	369	7	394	8	25	11	450	4	467	9	16	10
CM3	607°C/12h	431	21	456	15	25	25	523	21	539	21	16	29
CM3	607°C/24h	428	12	459	0	31	12	531	16	548	0	17	16
CM3	607°C/48h	410	13	438	5	27	14	497	22	524	6	27	23
CM3	607°C/96h	302	16	285	u	-17	16	422	6	411	u	-11	6
CM3	607°C/24h-air cool	448	1	455	3	18	3	520	6	527	9	19	11
CM3	624°C/12h	421	26	449	6	28	27	513	25	538	10	25	27
CM3	624°C/24h	417	4	440	4	23	6	508	7	529	6	21	9
CM3	624°C/48h	397	1	413	8	16	9	491	0	501	6	10	6
CM3	641°C/6h	409	3	432	4	23	5	506	4	523	8	18	9
CM3	641°C/12h	392	1	410	4	18	4	488	1	500	4	12	4
CM3	641°C/24h	306	u	334	30	28	30	434	u	443	17	9	17
CM3	AT	479	7	507	1	28	7	566	4	596	2		
CM5	590°C/24h	359	47	426	33	67	57	468	44	522	33	54	55
CM5	590°C/48h	337	35	410	29	73	46	448	24	505	24	57	34
CM5	590°C/96h	267	5	358	54	92	54	410	4	468	32	58	32
CM5	607°C/12h	388	u	440	22	52	22	494	u	541	25	47	25
CM5	607°C/24h	No	data										
CM5	607°C/48h	371	5	419	1	49	5	473	8	507	7	34	11
CM5	607°C/96h	257	8	320	11	63	14	399	13	444	4	45	13
CM5	607°C/24h-air cool	411	u	447	8	36	8	494	u	541	6	47	6
CM5	624°C/12h	375	u	430	23	55	23	482	u	526	12	44	12
CM5	624°C/24h	365	8	426	17	61	19	471	9	529	12	58	15
CM5	624°C/48h	364	31	412	12	48	33	457	u	507	5	50	5
CM5	641°C/6h	363	6	407	2	44	6	480	11	512	1	32	11
CM5	641°C/12h	355	u	412	10	57	10	465	u	520	11	55	11
CM5	641°C/24h	293	21	360	41	68	46	428	14	478	33	50	35
CM11	590°C/24h	471	14	612	6	141	15	566	23	689	8	123	24
CM11	590°C/48h	450	6	600	7	151	10	538	9	677	4	139	10
CM11	590°C/96h	421	23	591	5	170	24	499	27	656	4	157	27
CM11	607°C/12h	466	21	633	4	167	21	570	20	714	3	144	20
CM11	607°C/24h	446	15	582	8	136	17	539	22	650	6	111	23
CM11	607°C/48h	445	18	596	13	151	22	545	23	673	16	128	28
CM11	607°C/96h	365	34	573	6	208	34	463	19	635	4	173	20
CM11	607°C/24h-air cool	486	1	588	16	102	16	574	1	654	16	80	16
CM11	624°C/12h	452	12	612	17	161	21	557	15	693	18	136	23
CM11	624°C/24h	453	2	582	11	130	12	557	1	659	11	103	11
CM11	624°C/48h	425	0	571	8	146	8	523	0	652	11	129	11
CM11	641°C/6h	432	2	600	24	169	24	534	3	686	28	152	28
CM11	641°C/12h	432	9	590	25	158	26	536	10	674	24	138	26
CM11	641°C/24h	393	0	585	2	192	2	500	0	670	0	170	0
CM11	AT	490	5	636	8	146	9	577	19	722	13	145	23

VSR – cont'd

		Baseline		Irradiated				Baseline		Irradiated			
		σ_y	$\pm\sigma_y$	σ_y	$\pm\sigma_y$	$\Delta\sigma_y$	$\pm\Delta\sigma_y$	uts	±uts	uts	±uts	Δuts	±Δuts
Alloy	SR	MPa	MPa	MPa	MPa	MPa	MPa	MPa	MPa	MPa	MPa	MPa	MPa
CM12	590°C/24h	494	u	621	4	127	4	580	u	688	7	108	7
CM12	590°C/48h	486	u	617	5	131	5	577	u	680	0	103	0
CM12	590°C/96h	482	u	600	3	118	3	563	u	660	10	97	10
CM12	607°C/12h	488	u	633	8	145	8	571	u	707	3	136	3
CM12	607°C/24h	499	u	619	1	120	1	589	u	695	2	106	2
CM12	607°C/48h	475	1	607	14	133	14	562	8	679	13	117	16
CM12	607°C/96h	461	u	594	8	133	8	533	u	644	6	111	6
CM12	607°C/24h-air cool	495	27	650	u	155	27	572	33	719	u	147	33
CM12	624°C/12h	487	u	624	9	137	9	583	u	685	8	102	8
CM12	624°C/24h	479	u	613	1	134	1	557	u	675	1	118	1
CM12	624°C/48h	464	u	610	2	146	2	546	u	674	11	128	11
CM12	641°C/6h	478	1	627	1	149	1	566	6	705	1	139	6
CM12	641°C/12h	466	4	612	13	146	13	554	2	683	9	129	9
CM12	641°C/24h	452	2	610	6	159	6	531	1	672	1	142	2
CM12	AT	515	4	708	u	193	4	601	10	795	u	194	10
CM13	590°C/24h	438	23	482	23	45	32	522	30	559	30	37	43
CM13	590°C/48h	416	24	464	16	48	29	493	30	530	16	37	34
CM13	590°C/96h	407	8	449	4	42	9	486	11	513	7	28	13
CM13	607°C/12h	439	21	473	1	34	21	530	31	548	6	18	32
CM13	607°C/24h	419	5	475	6	56	8	504	4	561	8	57	9
CM13	607°C/48h	368	17	424	18	56	25	452	11	493	15	41	19
CM13	607°C/96h	327	0	423	13	96	13	430	0	495	11	65	11
CM13	624°C/12h	408	u	456	11	48	11	496	u	530	20	34	20
CM13	624°C/24h	294	u	380	u	86	u	412	u	467	u	55	u
CM13	624°C/48h	192	1	293	4	101	4	348	0	397	5	49	5
CM13	641°C/6h	304	62	410	31	106	70	417	29	495	33	78	44
CM13	641°C/12h	197	1	293	4	96	4	355	2	400	2	45	3
CM13	641°C/24h	190	2	286	5	96	5	353	3	405	6	52	6
CM13	AT	479	13	537	8	52	15	566	25	631	4	62	25
CM16	590°C/24hrs	469	15	600	1	131	15	569	9	679	1	110	9
CM16	590°C/48hrs	438	6	574	5	136	8	525	9	651	13	126	15
CM16	590°C/96hrs	450	1	554	6	104	7	534	4	620	6	86	7
CM16	607°C/12hrs	452	21	578	1	126	21	544	21	658	11	114	24
CM16	607°C/24hrs	450	14	584	17	134	22	546	23	666	13	120	26
CM16	607°C/48hrs	448	11	557	4	109	12	542	12	633	6	91	13
CM16	607°C/96hrs	374	20	533	8	159	22	465	11	599	6	134	12
CM16	607°C/24hrs-air cool	459	16	581	11	122	19	540	3	653	19	113	19
CM16	624°C/12hrs	427	12	566	2	139	12	521	15	644	12	123	19
CM16	624°C/24hrs	418	4	562	3	144	5	510	8	641	11	131	14
CM16	624°C/48hrs	410	17	554	1	143	17	507	16	636	4	128	17
CM16	641°C/6hrs	451	4	561	6	110	8	550	0	640	6	90	6
CM16	641°C/12hrs	395	24	564	1	168	24	497	17	646	6	149	18
CM16	641°C/24hrs	354	1	515	4	162	4	466	3	597	7	131	8
CM16	AT	503	6	602	3	99	7	588	3	691	13	103	13

VSR – cont'd

		Baseline		Irradiated				Baseline		Irradiated			
Alloy	SR	σ_y MPa	$\pm\sigma_y$ MPa	σ_y MPa	$\pm\sigma_y$ MPa	$\Delta\sigma_y$ MPa	$\pm\Delta\sigma_y$ MPa	uts MPa	±uts MPa	uts MPa	±uts MPa	Δuts MPa	±Δuts MPa
CM18	590°C/24hrs	451	16	523	2	72	16	539	12	601	4	62	12
CM18	590°C/48hrs	446	10	505	6	58	12	537	4	574	6	37	7
CM18	590°C/96hrs	418	13	480	8	62	16	497	19	545	20	48	27
CM18	607°C/12hrs	451	9	522	9	71	13	541	10	593	8	52	13
CM18	607°C/24hrs	433	8	510	9	77	12	521	15	587	4	66	15
CM18	607°C/48hrs	435	6	499	3	64	7	521	3	572	1	51	3
CM18	607°C/96hrs	394	7	460	2	66	7	471	4	522	1	51	4
CM18	607°C/24hrs-air cool	452	4	532	6	81	7	529	1	598	7	69	7
CM18	624°C/12hrs	439	3	506	13	67	13	528	4	579	11	51	12
CM18	624°C/24hrs	431	15	498	0	67	15	517	6	576	3	59	6
CM18	624°C/48hrs	413	6	486	6	73	8	502	7	564	9	62	12
CM18	641°C/6hrs	421	2	498	4	77	4	519	6	581	3	62	7
CM18	641°C/12hrs	420	5	490	8	70	9	505	9	564	8	59	12
CM18	641°C/24hrs	402	5	481	1	79	5	491	2	554	3	63	4
CM18	AT	478	5	579	5	101	7	569	10	659	6	90	12
CM19	590°C/24h	449	12	626	4	177	13	543	19	705	2	162	19
CM19	590°C/48h	448	6	595	1	147	6	545	10	663	10	118	14
CM19	590°C/96h	440	12	582	2	142	12	528	25	637	1	109	25
CM19	607°C/12h	446	8	636	8	190	11	541	17	718	11	176	20
CM19	607°C/24h	447	5	615	11	168	12	538	11	690	12	152	16
CM19	607°C/48h	435	12	597	3	162	12	528	21	679	2	150	21
CM19	607°C/96h	404	17	582	9	178	20	483	17	644	8	161	19
CM19	607°C/24h-air cool	459	16	612	4	153	17	533	21	681	14	148	25
CM19	624°C/12h	437	14	618	11	181	18	536	22	697	18	161	28
CM19	624°C/24h	430	5	601	5	170	7	531	9	681	6	149	11
CM19	624°C/48h	419	23	588	14	169	27	516	28	669	16	152	32
CM19	641°C/6h	432	1	609	1	177	1	542	11	692	2	150	11
CM19	641°C/12h	420	16	595	6	190	17	528	16	671	8	160	18
CM19	641°C/24h	369	3	575	4	206	5	482	3	656	4	174	5
CM19	AT	495	4	671	3	176	5	568	19	756	3	188	19

VSR – cont'd

Alloy	SR	Baseline σ_y MPa	Baseline $\pm\sigma_y$ MPa	Irradiated σ_y MPa	Irradiated $\pm\sigma_y$ MPa	$\Delta\sigma_y$ MPa	$\pm\Delta\sigma_y$ MPa	Baseline uts MPa	Baseline ±uts MPa	Irradiated uts MPa	Irradiated ±uts MPa	Δuts MPa	±Δuts MPa
CM20	590°C/24h	473	15	722	10	249	18	566	24	789	9	223	26
CM20	590°C/48h	461	8	722	8	261	12	556	9	792	11	236	14
CM20	590°C/96h	459	15	704	1	245	15	547	22	757	1	210	22
CM20	607°C/12h	453	3	722	4	269	5	530	1	780	1	250	2
CM20	607°C/24h	468	14	722	4	254	14	561	19	794	8	233	20
CM20	607°C/48h	466	11	719	2	253	11	563	13	787	4	224	13
CM20	607°C/96h	449	11	712	12	263	17	543	10	779	23	236	25
CM20	607°C/24h-air cool	409	15	696	6	287	16	496	12	754	4	258	12
CM20	624°C/12h	450	7	726	6	276	10	553	23	799	8	246	24
CM20	624°C/24h	449	11	721	0	272	11	552	18	790	0	238	18
CM20	624°C/48h	406	20	711	9	305	22	513	18	774	5	261	19
CM20	641°C/6h	439	11	726	1	287	11	546	19	804	13	258	23
CM20	641°C/12h	417	24	710	1	293	24	528	21	780	12	252	24
CM20	641°C/24h	384	10	707	4	323	11	510	12	776	3	266	12
CM20	AT	490	2	759	1	269	2	574	1	837	2	263	2

NRC FORM 335 (2-89) NRCM 1102, 3201, 3202

U.S. NUCLEAR REGULATORY COMMISSION

BIBLIOGRAPHIC DATA SHEET

(See instructions on the reverse)

1. REPORT NUMBER (Assigned by NRC, Add Vol., Supp., Rev., and Addendum Numbers, if any.)

NUREG/CR-6778

2. TITLE AND SUBTITLE

The Effects of Composition and Heat Treatment on Hardening and Embrittlement of Reactor Pressure Vessel Steels

3. DATE REPORT PUBLISHED

MONTH: May | YEAR: 2003

4. FIN OR GRANT NUMBER

Y6396

5. AUTHOR(S)

G. R. Odette, G. E. Lucas, D. Klingensmith, B. D. Wirth and D. Gragg

6. TYPE OF REPORT

7. PERIOD COVERED *(Inclusive Dates)*

8. PERFORMING ORGANIZATION - NAME AND ADDRESS *(If NRC, provide Division, Office or Region, U.S. Nuclear Regulatory Commission, and mailing address; if contractor, provide name and mailing address.)*

Department of Mechanical and Environmental Engineering
University of California Santa Barbara
Santa Barbara, CA 93106

9. SPONSORING ORGANIZATION - NAME AND ADDRESS *(If NRC, type "Same as above"; if contractor, provide NRC Division, Office or Region, U.S. Nuclear Regulatory Commission, and mailing address.)*

Division of Engineering Technology
Office of Nuclear Regulatory Research
U.S. Nuclear Regulatory Commission
Washington, DC 20555-0001

10. SUPPLEMENTARY NOTES

C. Santos, NRC Project Manager

11. ABSTRACT *(200 words or less)*

This report addresses several important issues regarding possible revisions of RG 1.99 Rev. 2 to predict irradiation induced hardening ($\Delta\sigma_y$) and hence embrittlement manifested as shifts (ΔT) in the 41 J Charpy test transition temperature. We are developing a $\Delta\sigma_y$ database from controlled, single-variable experiments to map the individual and interactive effects of metallurgical and environmental variables. The data are generated from a large matrix of composition-controlled alloys irradiated in the Irradiation Variables Facility (IVAR) at the University of Michigan Ford Research Reactor. The results provide quantitative and independent validation of the two component form of the NUREG/CR-6551 model, comprised of matrix feature (MF) and copper rich precipitate (CRP) terms. The IVAR database also quantitatively supports: 1) the model treatments of a strong copper-nickel interaction in the CRP term; 2) the treatment of phosphorous in the MF term; 3) an independent validation of a maximum effective matrix copper level (Cu_{max}) of around 0.3% following heat treatment; and 4) a sensitivity of Cu_{max} to nickel content. The IVAR database also shows: 1) manganese interaction with copper and nickel in the CRP contribution; 2) manganese and nickel increase the MF term; 3) a somewhat unanticipated effect of flux and flux-composition interactions on the fluence dependence of $\Delta\sigma_y$ and ΔT; and 4) a possible reduction in the effect of phosphorus at higher copper.

12. KEY WORDS/DESCRIPTORS *(List words or phrases that will assist researchers in locating the report.)*

Reactor Pressure Vessel, Embrittlement, Embrittlement Mechanisms

13. AVAILABILITY STATEMENT

unlimited

14. SECURITY CLASSIFICATION

(This Page) unclassified

(This Report) unclassified

15. NUMBER OF PAGES

16. PRICE

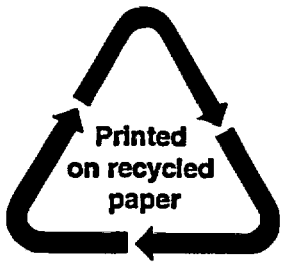

Federal Recycling Program

UNITED STATES
NUCLEAR REGULATORY COMMISSION
WASHINGTON, DC 20555-0001

OFFICIAL BUSINESS